Growth and Characterization of III-V Nanowires and Nanoneedles

Michael James Moewe

Electrical Engineering and Computer Sciences
University of California at Berkeley

Technical Report No. UCB/EECS-2009-100
http://www.eecs.berkeley.edu/Pubs/TechRpts/2009/EECS-2009-100.html

July 16, 2009

Growth and Characterization of III-V Nanowires and Nanoneedles

by

Michael Moewe

B.S. (University of California, San Diego) 2003

A dissertation submitted in partial satisfaction of the

requirements for the degree of

Doctor of Philosophy

in

Engineering – Electrical Engineering and Computer Sciences

And the Designated Emphasis

in

Nanoscale Science and Engineering

in the

Graduate Division

of the

University of California, Berkeley

Committee in Charge:

Professor Constance J. Chang-Hasnain, Chair
Professor Ming C. Wu
Professor Peidong Yang

Fall 2009

The dissertation of Michael Moewe is approved:

Professor Constance J. Chang-Hasnain | Date

Professor Ming C. Wu | Date

Professor Peidong Yang | Date

University of California, Berkeley

Fall 2009

ABSTRACT

Growth and Characterization of III-V Nanowires and Nanoneedles

by

Michael Moewe

Doctor of Philosophy in Engineering – Electrical Engineering and Computer Sciences

And the Designated Emphasis in Nanoscale Science and Engineering

University of California, Berkeley

Professor Connie J. Chang-Hasnain, Chair

Integration of optoelectronic materials with silicon is an important area of study, which could enable silicon CMOS-integrated optical devices for chip-scale optical communication, with the potential for higher bandwidth and lower costs. However, optical-quality III-V thin-film growth on silicon is difficult due to the crystal lattice-mismatch between the materials, and III-V growth typically requires growth temperatures of 600 °C, whereas silicon CMOS processes are limited to < 450 °C.

In this work we present methods for overcoming these lattice-mismatched epitaxial limitations. Au-catalyzed vapor-liquid-solid nanowire growth is conducted via metal-organic chemical vapor deposition, and material-dependent critical diameters are discussed. Experimental results are presented which support theoretical predictions of a critical nanowire maximum diameter for epitaxial growth. A model is developed which predicts the nanowire growth rate, and dependence of the crystal phase on the nanowire diameter observed in experiments.

We also present a new growth mode which produces III-V nanoneedles via metal-organic chemical vapor deposition. The nanoneedles are catalyst-free, ultra-sharp GaAs-based structures, with record narrow tip diameters of less than 1 nm, sharp 6-9° taper angles, and lengths up to 10 µm. The crystals are pure wurtzite phase crystal, free of zincblende phases, which is uncommon for GaAs. The nanoneedles grow on GaAs, silicon and sapphire substrates and exhibit bright room-temperature photoluminescence. The growths are conducted at 380 to 420 °C, making the process ideal for silicon-CMOS integration. The nanoneedles can also be large enough for device fabrication using top-down, standard processing techniques.

Growth of ternary nanoneedles is also demonstrated, specifically, pure InGaAs nanoneedles. The InGaAs nanoneedles exhibit similar structural properties as the GaAs nanoneedles, being single-crystal, with bright photoluminescence and ultra-sharp tips. Core-shell heterostructure nanoneedles of InGaAs and AlGaAs are also demonstrated. InGaAs quantum well nanoneedles having near-band-edge emission tunable by 380 meV are also shown, with photoluminescence emission below the silicon absorption edge, facilitating use of integrated passive silicon devices.

Transmission electron microscopy analysis of the nanoneedles is also presented. The results elucidate the uniform crystal phase and lattice constants, and show the ultra-sharp tips of the nanoneedles of the different III-V nanoneedle compositions grown on the various substrates.

Professor Constance J. Chang-Hasnain	Date
Dissertation Committee Chair

To my parents

Contents

Acknowledgement

I would like to thank my advisor, Professor Connie Chang-Hasnain, for her tireless dedication, insight and eternal optimism. She has made this research group both an exciting environment to conduct research, as well as helped to create the uniquely collegial and supportive atmosphere among the students and various collaborators.

I would also like to thank the other members of my dissertation committee, Professor Ming C. Wu and Professor Peidong Yang, for their input and discussions.

The body of work in this dissertation would not have been possible without the collaboration and hard work of many of my colleagues. In particular I would like to thank Chih-Wei “Linus” Chuang, who has been a pleasure to work with over the years and one of the kindest and most considerate people I’ve had the pleasure to know. His expertise in material growth in MOCVD and characterization has made possible many of the results presented in this dissertation, and his insight and enthusiasm has made working on this research all the more enjoyable. I would also like to thank Shanna Crankshaw, who has helped to make possible our various spectroscopy capabilities, and whose persistence and dedication to science have been integral to this work. I would like to thank all the other people in our group whom I have worked with on various projects, such as Eui-Tae Kim, Pei-Cheng Ku, Nobby Kobayashi, Forrest Sedgwick, Ye “Mervin” Zhou, Matthias Kuntz, Roger Chen, Thai Tran, Kar-Wei “Billy” Ng, Phedon Palinginis,

Lukas Chrostowski, Chih-Hao Chang, Wendy Zhou, and also Hao-Lin Chen for the helpful discussions about our research projects.

I would also like to thank our various outside collaborators, particularly Vladimir Dubrovskii, who has provided exciting collaboration and insight on the nanowire growth modeling. I would also like to thank Christian Kisielowski, whose training, support and discussions have helped make possible the transmission electron microscopy study of our nanoneedles presented in this dissertation.

I would also like to thank my friends, who have been like a second family to me throughout many years, and made my life truly rich in immeasurable ways. They have given me a balance and foundation in my life, without which I could not have accomplished my goals or enjoyed my life to the degree that I have thus far. Most importantly I would like to thank my parents, who helped cultivate within me a sense of intellectual curiosity and independence, and whose love and selfless support have helped me to pursue my goals.

1 Introduction

Integration of optoelectronic materials with silicon is an important area of research, which could enable CMOS-integrated optoelectronic devices for chip-scale optical communication, with potential for higher bandwidth and lower power devices. However, achieving optical quality III-V thin-film growth on silicon is difficult due to the crystal lattice-mismatch between the materials which causes defects. III-V growth also typically requires high growth temperatures of ~600 °C, whereas silicon-CMOS processes are limited to temperatures < 450 °C [1]. In this work, we present new growth techniques and nanostructures which have advantages over typical epitaxial growth, particularly those with the ability for integration with silicon-CMOS.

We first present the growth of GaAs on the atypical (110)GaAs substrate orientation, which has longer carrier spin coherence lifetimes than (001) growth, which is advantageous for slow light devices. This work shows the interesting physical properties resulting from quantum confinement in atypical crystal orientations or structures.

Next, III-V materials growth on lattice-mismatched substrates is presented. First, low-temperature vapor-liquid-solid (VLS) nanowire growth is discussed. Experimental results of MOCVD-grown nanowires confirm predictions of a maximum epitaxial critical diameter which is inversely related to nanowire/substrate lattice mismatch. A growth model is developed which predicts the length-diameter dependence of the nanowires based on the Gibbs-Thomson effect, and also predicts the dependence of the crystal phase on the nanowire diameter observed in experiments.

We also present the growth of III-V nanoneedles via metal-organic chemical vapor deposition. The nanoneedles are catalyst-free, ultra-sharp GaAs-based structures, with record narrow tip diameters of less than 1 nm, sharp 6-9° taper angles, lengths up to 4 µm. The nanoneedles grow on GaAs, silicon and sapphire substrates under the same growth conditions, are free of the typical twinning defects seen in nanowires, and exhibit bright room-temperature photoluminescence. The growths are conducted at 380 – 420 °C, temperatures even lower than that of typical nanowires, making the process ideal for silicon-CMOS integration. The nanoneedles can also be large enough to facilitate device fabrication using top-down, standard processing techniques.

Ternary nanoneedle compounds are demonstrated, such as pure InGaAs nanoneedles, as well as InGaAs and AlGaAs heterostructures. We show photoluminescence of quantum well nanoneedles with emission tunable by 380 meV, below the silicon absorption edge.

2 (110) GaAs Quantum Well Growth for Slow Light Devices

Most of the major work done in III-V epitaxy for optoelectronic devices has been on the (001) crystal orientation in zincblende semiconductor substrates, due to the favorable growth conditions for this orientation. However, quantum wells grown on (110)GaAs have been shown to have much longer spin relaxation lifetimes, compared with (001)GaAs, due to the suppression of the Dyakonov Perel (DP) effect which dominates at higher temperatures [2]. The DP effect treats the spin splitting of the conduction band in zincblende semiconductors at finite wave vectors as equivalent to an effective magnetic field that causes electron spin precession [3]. For (110)GaAs, the effective magnetic field $B_{eff}(k)$ is always normal to the plane of the quantum well. Therefore if the initial electron spin is oriented along the growth direction, the scattering processes will not change the spin orientation. Ohno et al. [2] have shown that (110) quantum wells at room temperature can have spin relaxation times of as much as 2 ns, much longer than the 70 ps lifetimes exhibited for (001) substrates. The (110) substrates also show an increasing dependence of spin relaxation lifetime vs. temperature, persisting up to room temperature [4], which makes this substrate orientation very suitable for practical devices which rely on spin coherence, such as quantum logic gates.

2.1 Challenges for Growth on (110) Substrates

Molecular beam epitaxy (MBE) is a common technique used for growth of high-quality quantum wells. MBE uses extremely high purity source materials for deposition in an ultra-high vacuum chamber, typically heated pure metals in effusion cells blocked by shutters. The heated materials evaporate from the effusion cells and react upon reaching the wafer surface, growing smooth, high purity epitaxial layers. The ultra-high vacuum conditions limit undesirable background doping in the quantum wells, making MBE an ideal method for any semiconductor device dependent on optical transitions in III-V quantum wells.

Typically MBE growth is conducted on the (001) plane of GaAs wafers, because the chemistry of the surface on this crystal face is ideal for MBE growth. The (110) surface of GaAs is much more difficult for growth than the (001) surface. This is because arsenic has a lower sticking coefficient and lower desorption energy on the (110) surface, due to the arrangement of the group III and V atoms on the respective planes. Figure 2.1 shows the difference between the two growth planes. The (001) surface is completely homogeneous, consisting of a plane of either group V or group III atoms. This results in many free bonds which will adsorb the next layer of atoms. The (110) surface has fewer dangling bonds, and contains an equal amount of group III and V atoms, making surface reconstruction more difficult.

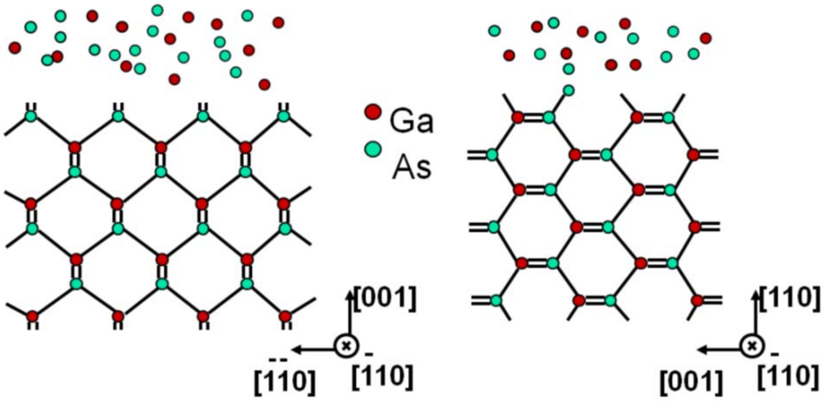

Figure 2.1 Comparison of growth on (001) and (110) substrates. The (001) substrate has a higher arsenic sticking coefficient due to the difference in the bonds at the surface, and the complete surface reconstruction of the group III or V elements. The (110) orientation has both group III and V atoms on each monolayer, resulting in a lower sticking coefficient.

There are several ways to overcome these limitations for (110) MBE growth. The first is to use a low growth temperature. This increases the sticking coefficient of the adatoms, but has the drawback of increasing the incorporation of background impurities, such as carbon. Arsenic in solid form typically exists as As_4, and must dissociate on the surface of the substrate. To facilitate this process, the solid arsenic source can be installed with a heated filament at the exit of the source which can crack the As_4 into two As_2 molecules, increasing the adsorption rate of arsenic to the substrate surface. High arsenic beam pressures can also be used, which further increase the rate of arsenic adsorption on the (110) surface. This can reduce the gallium mobility on the surface though, which increases surface roughness. To counteract this, low growth rates must be used as well. This, in addition to lower growth temperatures, can also increase background impurity incorporation, so chamber cleanliness is of utmost importance. Annealing can also be used to reduce surface roughness, which is more of a problem for the (110) growths [5].

2.2 (110) GaAs Quantum Wells Grown by Molecular Beam Epitaxy

The (110) GaAs/AlGaAs quantum wells discussed in this section were grown at low temperatures of 485 °C in a Varian Modular Gen II MBE system. The temperature was measured with a pyrometer calibrated by measuring the oxide evaporation temperature, as indicated from the transition of the reflection high-energy electron diffraction (RHEED) electron beam from a diffuse to spotty condition. An arsenic cracker was used as well with the cracker section heated to 900 °C to crack As_4 molecules into As_2. The arsenic beam equivalent pressure was held at 2.0×10^{-5} torr, twice that of the typical (001) GaAs growths for this machine. The growth rate was 0.25 μm/hr, 25% of the rate typically used for the (001) growths. The growth chamber was also scrubbed and etched clean and baked beforehand and loaded with new material to prevent background impurity incorporation. The resulting chamber pressure at standby mode was less than 5×10^{-11} torr.

Calibrating growth rates is also important for growing quantum well samples with consistent well thicknesses. Typically RHEED is used. In this method a 10 keV electron beam is directed across the wafer surface at a glancing angle, resulting in diffraction from only the surface layers of atoms. For (001) growth, these diffraction peaks oscillate in intensity in accordance with the complete assembly of each monolayer of alternating arsenic or gallium atoms. When the monolayer is incomplete, the monolayer-high steps cause reflections of the electron beam to be out of phase relative to each other, resulting in a decrease in intensity. However, since the (110) surface has a mixture of group III and V atoms as shown in Figure 2.1, the surface does not tend to reconstruct in smooth atomically flat layers, so RHEED oscillations cannot be measured. To overcome this limitation, the (110) growth rates were first calibrated on a (001) wafer, which was then replaced by the (110) substrate for growth. The oscillation period was recorded and plotted using a camera and computer interface.

Two quantum well samples were grown for comparison with the same structure, on (001) and (110) substrates. The structure was a leaky waveguide sample to facilitate simultaneous experiments using electromagnetically induced transparency (EIT) and coherent population oscillation (CPO), and be able to select the optimal amount of signal optical depth. The well consisted of AlGaAs barrier layers to improve the surface quality, $Al_{0.3}Ga_{0.7}As$ barriers and a 130 Å quantum well region. The exact structure is shown in Figure 2.2.

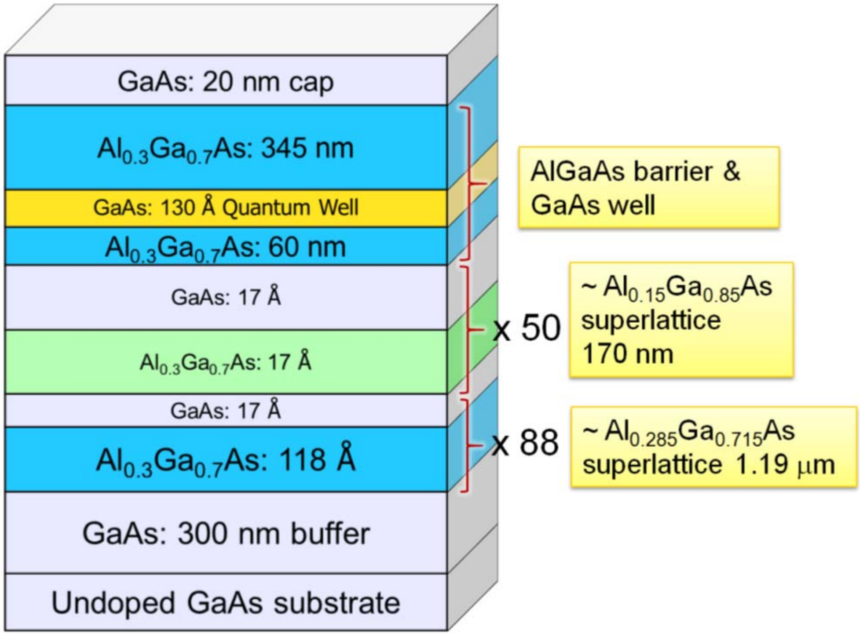

Figure 2.2 Quantum Well Leaky Waveguide structure

Figure 2.3 shows photoluminescence measurements for both samples, measured using a diode-pumped solid state laser at 532 nm. The (110) sample is redshifted from the (001) quantum well by 2.4 nm. This is typical for the (110) growths, and is possibly due to the increased heavy hole mass for this crystal orientation, as reported by Y. Kajikawa [6]. The photoluminescence linewidth is also larger, but is comparable to the narrowest linewidths reported in literature [5].

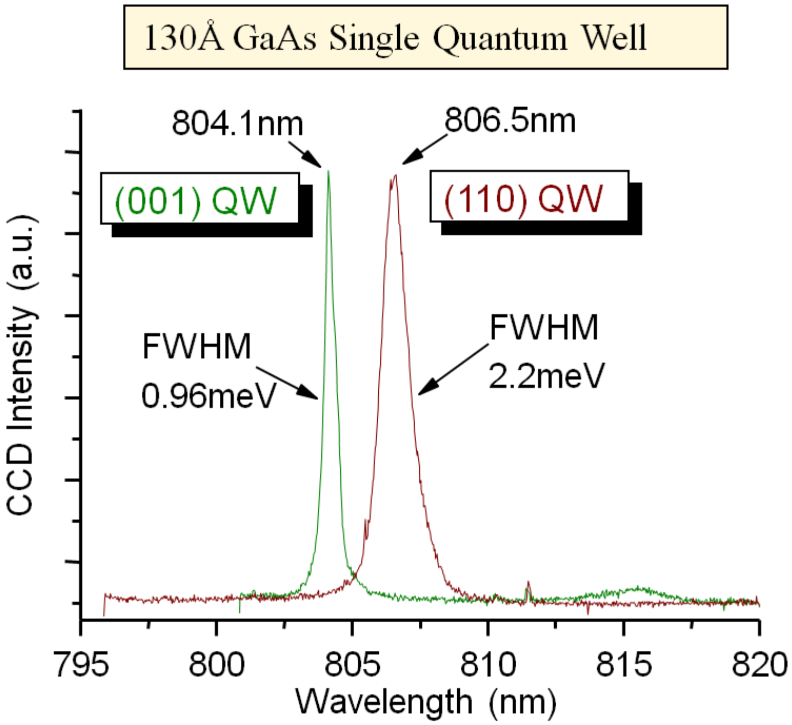

Figure 2.3 130 Å (001) and (110) quantum well photoluminescence at T = 4K, excited with a 532 nm diode-pumped solid state laser. The (110) is possibly a result of the increased heavy hole mass for the (110) orientation.

2.3 (110) Quantum Well Coherent Population Oscillation

Slow light devices have been demonstrated recently in semiconductors [7-9] using nonlinear effects such as EIT and CPO. The goal of these devices is for all-optical buffering of optical signals by modifying the material dispersion using a control beam, causing a reduction in the group velocity v_g and an effective slowdown factor $S = c/v_g$, where c is the speed of light in a vacuum. All-optical buffering could potentially improve network speed and decrease device cost by eliminating the need for converting optical signals to electrical signals for temporary storage in memory in electronic devices. Instead, optical waves would be compressed spatially as they travel through the slow light medium by the factor S.

The (110) quantum well structures from Figure 2.2 were used as slow-light devices at both low and room temperature using CPO [9,10]. The low-temperature work utilizing these (110) quantum wells demonstrated CPO effects, with measured time-domain slowdown factors of 10^6 using a surface-normal geometry along the growth direction [9]. The CPO nonlinear optical response results from wave-mixing between two optical fields via a resonant dipole optical transition [11]. Wave-mixing between pump and probe beams creates a temporal oscillation f of the excited state population, which results in coherent transfer of energy between the pump and probe beams. This results in an absorption dip around the control beam wavelength.

For practical all-optical-buffer devices, room temperature operation is required. For the room temperature measurements, a waveguide geometry using the structure in Figure 2.2 was used. This gives the ability to control the optical depth of the probe beam. The confinement factor Γ of the quantum well was ~1%.

To fabricate slab waveguides, the ~300 μm thick (110) quantum well substrates were scribed and cut into rectangular pieces with edges aligned to the $(1\bar{1}0)$ and (001) facets. GaAs typically cleaves along the $\{110\}$ family of planes. The waveguides require a smooth cleave along the $(1\bar{1}0)$ plane so that this plane can act as the input facet of the waveguide. If rectangular pieces are not used, thin (110)GaAs will tend to cleave into triangular pieces as shown in Figure 2.4, and achieving a short waveguide < 500 μm long with flat input and output facets is difficult. Having a rectangular edge perpendicular to the (110) cleaving plane (shown at the bottom of Figure 2.4) causes the wafer to cleave only along the plane shown in red, allowing the cleaving of thin waveguide strips, as shown by the two red lines.

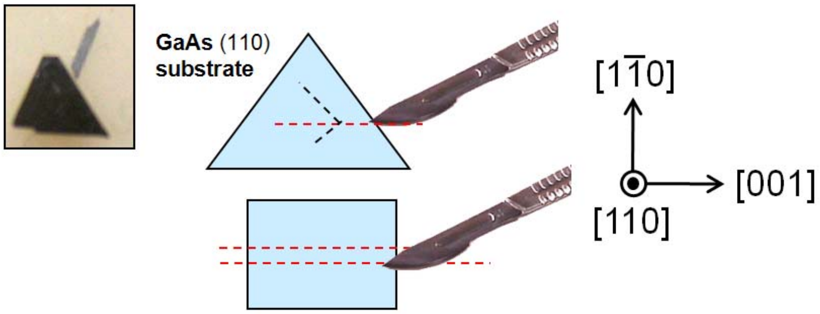

Figure 2.4 (110)GaAs tends cleave into triangular pieces, making cleaving along the (110) plane shown in red difficult. Contrarily, (100)GaAs cleaves in rectangular pieces easily along the perpendicular (011) and $(01\bar{1})$ planes.

To cleave the waveguides, the backside of the rectangular pieces were first mechanically thinned to ~90 µm thick to facilitate cleaving with a scalpel, and a 440 µm long strip was cleaved using a scalpel. The result is shown in Figure 2.5.

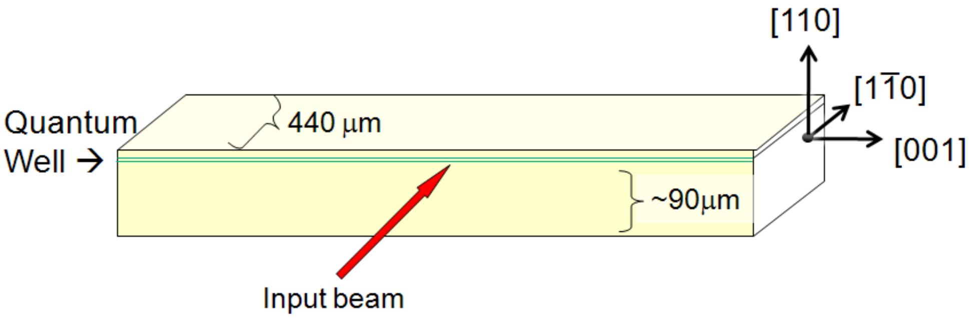

Figure 2.5 Diagram of the waveguides cleaved based on the method described in Figure 2.4. The waveguide used for the CPO experiment was 440 µm long, chosen to tune the proper amount of absorption based on the confinement factor for this leaky waveguide mode.

The slab waveguide strip was mounted on a thin copper edge to allow coupling of light into the slab waveguide and provide thermal contact.

For CPO, the pump and probe beams are typically detuned from each other by a small frequency offset δ. For this experiment, the pump and probe beams were generated by RF amplitude modulation of a continuous wave Ti:Sapphire laser at 500 MHz, resulting in modulation sidebands which serve as the probe beam, and the carrier wave which serves as the pump beam. The group delay variation was measured by comparing the time difference between the on-resonance (heavy hole-exciton transition) and off-resonance (below absorption edge) cases of the pump beam wavelength.

The measured delays for various input powers vs. modulation frequency are plotted in Figure 2.6. The highest delay measured is 830 ps, with a slowdown factor of 565.

The resonance FWHM is given by the expression $\Delta\nu = (1 + P/P_0)/(\pi T_1)$, where P is the pump power and P_0 is the saturation power, and T_1 is the upper state lifetime [12]. Linear fitting the FWHM of the three curves in Figure 2.6 results in T_1 = 5.9 ± 0.3 ns and P_0 = 123 ± 13 mW. These results are similar to those measured in (001) quantum wells [13] demonstrating that the observed time-domain delay is resulting from CPO.

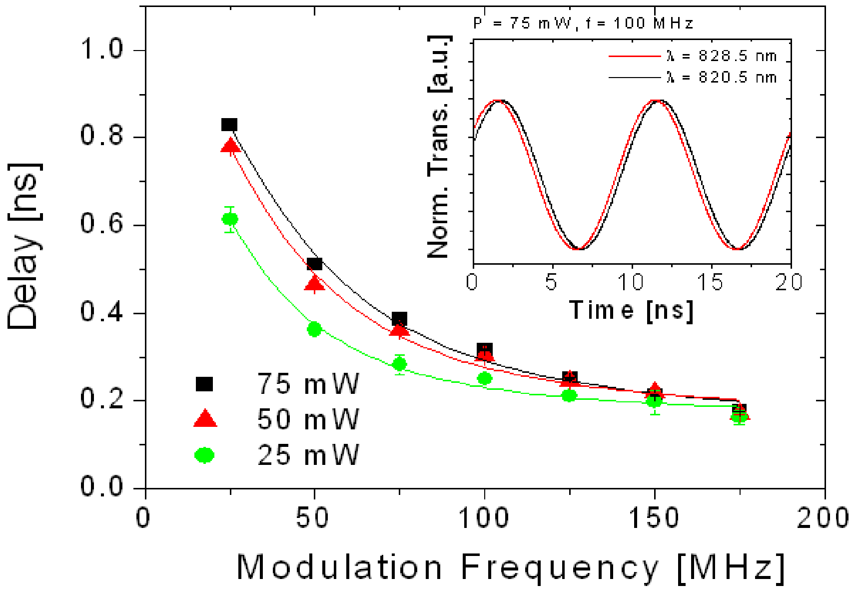

Figure 2.6 Time delay (comparing on- and off-resonance) vs. modulation frequency for various pump powers. The inset shows a typical trace of the on- and off-resonance conditions with a tunable delay between the two traces.

The results here show that the material in the (110)GaAs quantum wells is high quality, despite the unusual crystal orientation for MBE growth. This means the structures have the potential for even greater slow light tunability at room-temperature using EIT effects due to the enhanced spin lifetimes in (110)GaAs, and the waveguide technique allows for both CPO and EIT experiments on the same structure for comparison.

3 Critical Diameters of InP Nanowires Grown on Lattice-Mismatched Substrates

3.1 Lattice-Mismatch in Two-Dimensional Epitaxial Growth

The monolithic integration of different semiconductor materials, particularly in direct epitaxial heterostructure growth, has been a very important area of study, as it allows for the ability to select optimal material properties for various regions of a device over a wider range, and to effectively create new materials such as quantum confined wells, wires and dots. In particular, the ability to integrate optical-quality III-V materials with silicon would pave the way for semiconductor lasers integrated directly with silicon CMOS electronics. Silicon, having an indirect bandgap, currently cannot be used alone for efficient semiconductor laser devices. The issue of lattice mismatch and resulting strain between III-V materials and silicon makes normal two-dimensional thin film epitaxy difficult, due to the tendency of the epitaxial layers to relax by forming defects after a certain critical thickness is reached [14]. The lattice mismatches with silicon for typical materials used in semiconductor lasers, such as GaAs and InP, are 4.1% and 8.1% respectively. Removing this limitation could enable new applications, such as chip-scale optical communication.

Figure 3.1 shows the typical result of growing lattice-mismatched III-V material on silicon substrates. Due to the larger lattice constant of the epitaxial layer, the epitaxial material will be compressively strained at first when grown on a silicon substrate, with respect to its typical equilibrium lattice constant. If the layer thickness reaches a certain critical thickness, which is inversely proportional to the lattice mismatch, the strain between the two materials will end up relaxing via misfit dislocations [15], as highlighted in the red circles in Figure 3.1. The defects act as sites for non-radiative recombination, limiting the optical quality of the material. Threading dislocations propagating into the epitaxial layer can also prevent radiative recombination.

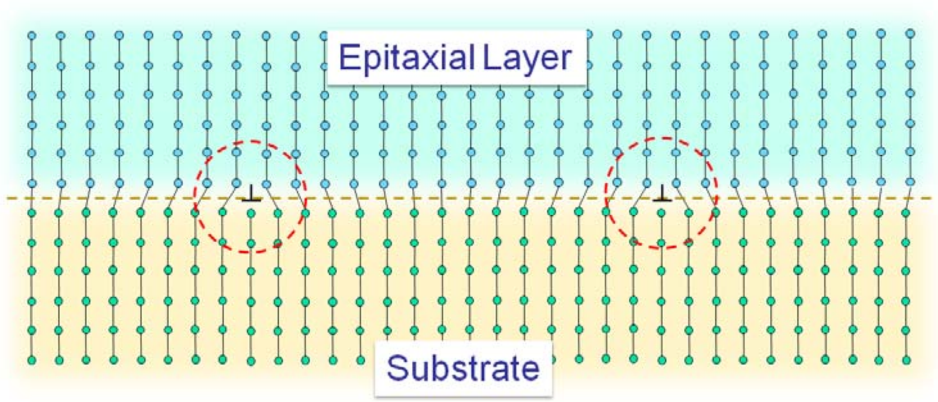

Figure 3.1 Diagram of misfit dislocations forming due to lattice-mismatch between the epitaxial layer and substrate.

3.2 Nanowire Vapor-Liquid-Solid Growth Mechanism

Nanowires grown by the vapor-liquid-solid (VLS) method, contrary to two-dimensional (2D) thin films, are promising for the monolithic integration of semiconductor materials with different lattice constants, due to their ability to accommodate strain in two dimensions [16-19]. Nanowires can be grown using the VLS mechanism [17] via both MBE and MOCVD. Figure 3.2 shows the growth process. The growth is catalyzed by the use of metal nanoparticles, primarily Au. The growth is conducted at much lower growth temperatures than typical 2D epitaxy, 430 – 470 °C in our experiments. The III-V reactants in vapor phase are adsorbed into the metal catalyst particle. The reactants can also adsorb to the surface or NW sidewall and migrate into the nanoparticle, although this mechanism is not dominant for MOCVD growth.

When the reactants reach a supersaturation point, they nucleate at the substrate/nanoparticle interface, resulting in layer-by-layer stacking of III-V material, resulting in the nanowire growth. The vapor, liquid and solid phase steps are labeled as

V, L and S, respectively, in Figure 3.2. The catalyst particle reduces the reaction energy of the growth, resulting in selective growth only at the positions of the Au nanoparticles. The diameters of the nanowires are determined by the diameter of the contact area between the Au nanoparticle and the substrate.

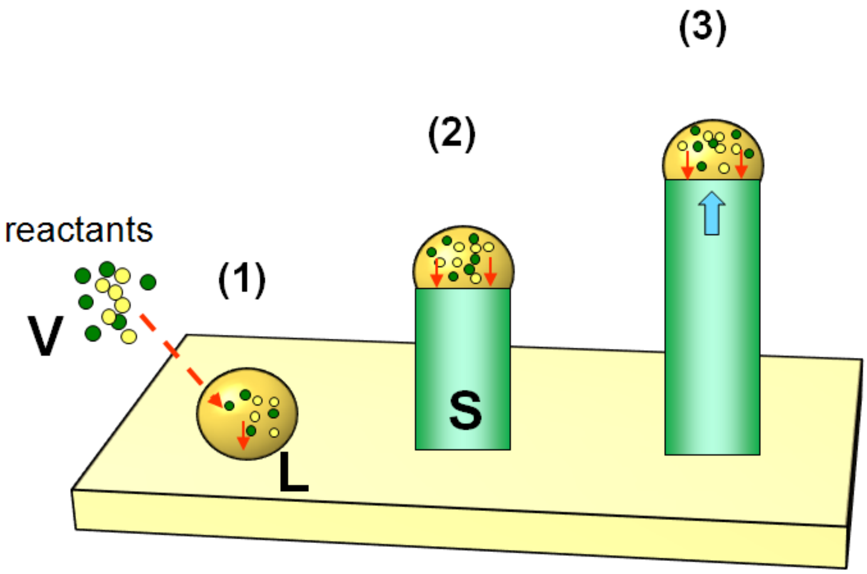

Figure 3.2 Nanowire growth process, from vapor phase, to liquid phase (1), to the solid nanowire phase (2), and continued growth in the vertical direction (3).

The nanowires also have the ability to relieve strain in the two dimensions perpendicular to their growth direction, as long as their diameter is below a critical diameter, which is dependent on the lattice-mismatch between the nanowire material and the substrate [16,18].

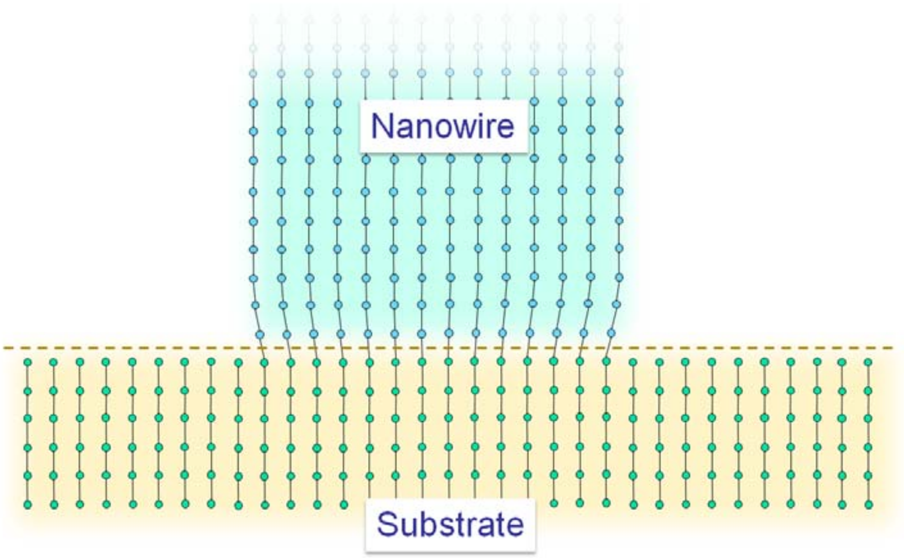

Figure 3.3 Lattice-mismatched material grown in the form of a nanowire can relieve strain by expanding/contracting in the two lateral dimensions, relieving strain without forming misfit dislocations.

3.3 Nanowire Lattice-mismatch Critical Diameter

The diameters of nanowires are limited by the lattice-mismatch between the nanowire and the substrate. Below a certain lattice-mismatch-dependent critical diameter, $D_e(\varepsilon_0)$, the nanowires will be free of defects. Above this diameter, one or more misfit dislocations will occur, which has the effect of reducing the overall formation energy of the nanowires [20]. The overall formation energy of the nanowire is given as

$$E_n = E_{el}^{*} + E_{disl}^{n} \, . \tag{3.1}$$

E_{el}^{*} is residual lattice strain energy and E_{disl}^{n} is the dislocation energy, which are both dependent on the lattice-mismatch [20].

We have demonstrated through experimental nanowire growths that the nanowire growths correspond to the theoretical predictions of Ertekin et al. [20]. Several different nanowire combinations were grown – InAs on silicon, InP on silicon and InP on GaAs with 11.6%, 8.1% and 4.1% lattice mismatches, respectively. The critical diameter $D_e(\varepsilon_0)$, is shown to be inversely proportional to lattice mismatch between the nanowire and substrate crystal lattice. This diameter equals 26 nm for InAs/silicon (lattice mismatch ε_0 = 11.6%), 36 nm for InP/silicon (ε_0 = 8.1%) and 96 nm for InP/GaAs (ε_0 = 4.1%) systems [16].

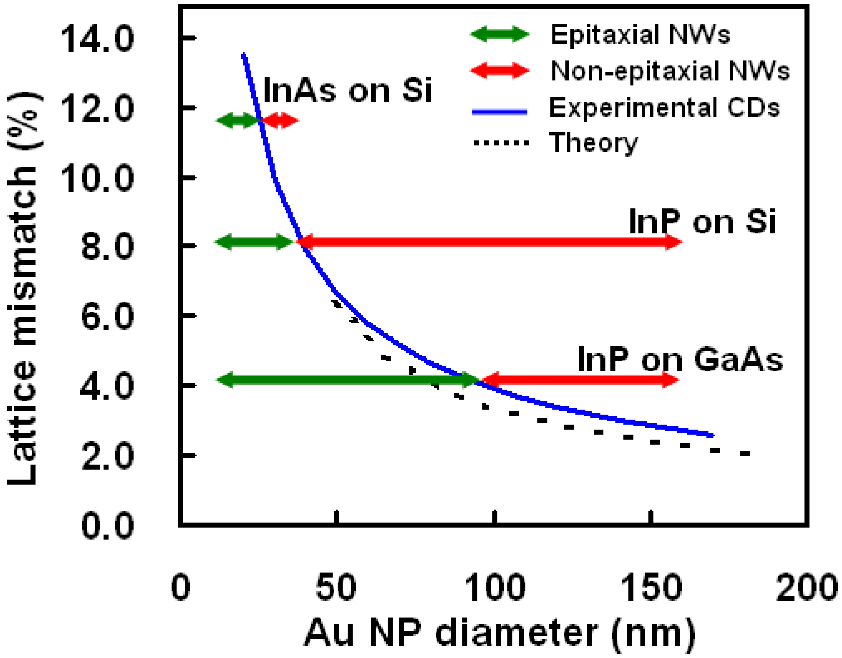

Figure 3.4 Nanowire epitaxial and non-epitaxial growth regimes for various combinations of nanowire material and substrate material. The theoretical curves from [20] are shown for comparison.

Figure 3.5(a) shows an example of InP nanowires grown on silicon using Au catalyst nanoparticles which are 20 nm in diameter on average. A histogram of the nanowire diameters for this growth is plotted in Figure 3.5(b), which corresponds to the distribution of the Au catalyst nanoparticle diameters. Figure 3.5(c)-(d) show the same growth conditions, except nanoparticles were used with average diameters 50 nm and

100 nm, respectively. The growth results in spiky, polycrystalline structures due to the inability of the larger diameter nanowires to accommodate the strain between the InP and silicon without forming misfit dislocations.

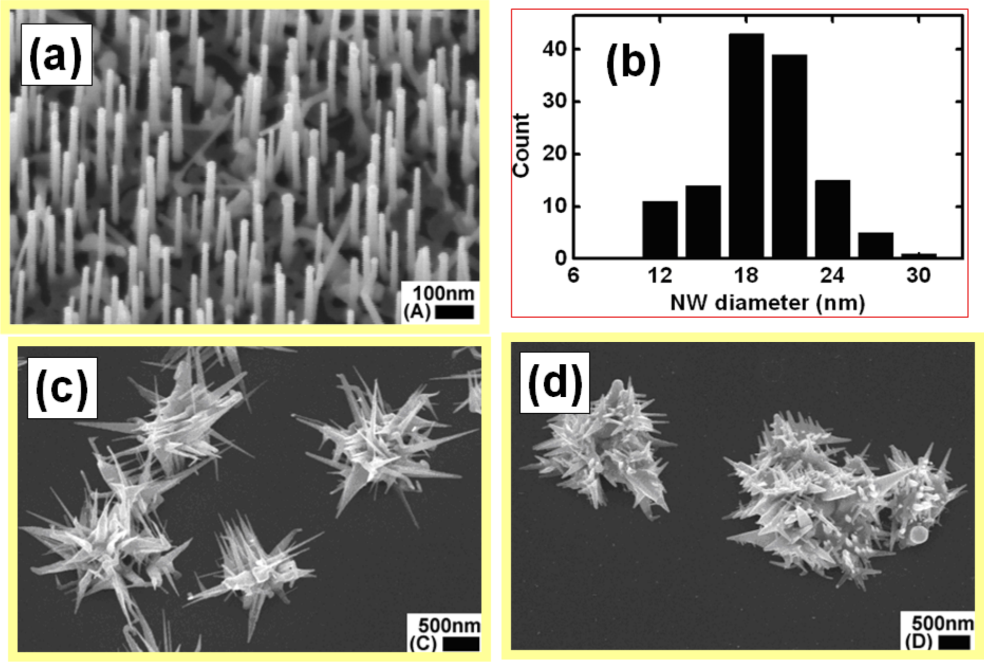

Figure 3.5 (a) InP nanowires grown on silicon using Au nanoparticles and VLS growth. (b) shows the nanowire diameters used in (a), corresponding to the distribution of Au nanoparticle diameters used as catalysts. (c) and (d) show growths using 50 nm and 100 nm, which result in defected polycrystalline structures due to the inability to accommodate strain between the InP and silicon at larger diameters.

3.4 Nanowire Growth Modeling

For the controlled growth of nanowires in device applications, it is important to understand their growth properties and also the factors influencing the crystallographic structure of nanowires to control factors such as length and crystal phase. Many recent studies [21-23] demonstrate that III-V nanowires often grow in the hexagonal wurtzite phase, in contrast to the typical III-V bulk form with cubic zincblende phase. This phenomenon has been observed for most zincblende compounds and epitaxial techniques, both for Au-assisted [21,22] and selective area [24] growth. Nanowires often contain sequences of different crystal phases, rotational twins, and stacking faults. This can potentially affect the material properties, so the control over the crystal phase is one of the main challenges of III-V nanowire fabrication.

This section address two issues of MOCVD growth of InP nanowires on (111)B GaAs substrates: 1) study of growth mechanisms and 2) investigation of crystallographic structure depending on the nanowire diameter. We show that VLS growth of InP nanowires is controlled by direct impingement of growth species onto the nanoparticle surface and is strongly influenced by the Gibbs-Thomson effect. The nanowire crystal phase is shown to be diameter dependent, so that 20 nm wide InP nanowires are predominantly wurtzite and 60 nm or larger nanowires exhibit twining between wurtzite and zincblende structure. We also present theoretical models qualitatively explaining the experimental observations.

The InP nanowires were grown using colloidal Au nanoparticles as catalysts in a MOCVD reactor in the VLS growth mode. The size of Au nanoparticles ranged from 10 to 160 nm, and the nanoparticles are chlorine-passivated to prevent aggregation of the nanoparticles. The mole fractions of the group V (tertiarybutylphosphine) and group III (trimethylindium) sources were 1.91×10^{-5} and 1.17×10^{-3}, respectively, in a 12 l/min hydrogen carrier gas flow, yielding a V/III ratio of 61. This ratio was found to be within a range that yields straight nanowires with uniform diameter from base to top [19]. The growth temperature was 470 °C and the growth time was 3 minutes.

In order to understand the growth mechanisms, we first study the length-diameter ($L(D)$) dependences of our nanowires. The nanowire growth can be controlled either by the direct impingement of material onto the nanoparticle [25], or by the adatom diffusion to the top of the nanowire [26,27]. The first case is characterized by an increasing dependence of the nanowire growth rate dL/dt on its diameter D, and the second case is characterized by a decreasing dL/dt on its diameter D. From the analysis of scanning electron microscopy (SEM) images of different samples, we constructed experimental $L(D)$ curves. The corresponding $L(D)$ dependence is shown in Figure 3.6, with a typical corresponding SEM image shown in the inset.

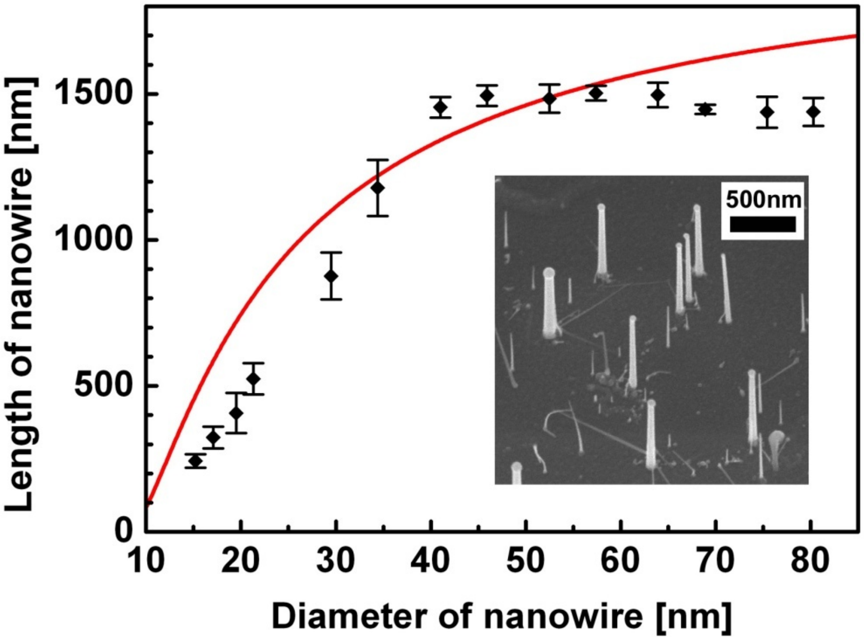

Figure 3.6 Experimental (points) and theoretical (line) length-diameter dependences of InP nanowires. Inset: SEM image of InP nanowires grown by MOCVD on a (111)B GaAs substrate.

We have found that the measured nanowire lengths $L(D)$ increase as D increases. Such behavior is usually explained by the Gibbs-Thomson effect of elevation of chemical potential in a nanowire with a curved lateral surface [25]. The adatom diffusion to the top is rather small, which is opposite to the case of MBE growth [27] and can be explained either by a slow rate of chemical reaction at the surface or by a low surface diffusivity by the growth species. According to the Givargizov-Chernov model [28], the added factor to the bulk chemical potential, $\Delta\mu_S$, in a nanowire of diameter D is equal to $4\Omega\gamma^l_{S-V}/D$. Ω is the volume per III-V pair in the crystal and γ^l_{S-V} is the surface energy of the lateral solid-vapor interface. The effective difference of chemical potentials in the vapor and the solid phase $\Delta\mu_{eff}$, driving the nanowire formation, is therefore lower than at the surface of a bulk crystal where ($D \rightarrow \infty$). $\Delta\mu = \Delta\mu_V - \Delta\mu_S$, and $\Delta\mu_{eff} = \Delta\mu - 4\Omega\gamma^l_{S\text{-}V}/D$. The second assumption of the model is that the growth rate is proportional to $\left(\Delta\mu_{eff}/k_BT\right)^2$, where T is the surface temperature and k_B is the Boltzmann constant. Writing the growth rate in the form $dL/dt = K\left(\Delta\mu/k_BT - 4\Omega\gamma^l_{S\text{-}V}/Dk_BT\right)^2$, with Kbeing the crystallization coefficient, and integrating, we arrive at

$$L = L_0\left(1 - \frac{D_{min}}{D}\right)^2 . \tag{3.2}$$

Here, $L_0 = Kt\left(\frac{\Delta\mu}{k_BT}\right)^2$, is the maximum length of infinitely thick wires. t is the growth time and $D_{min} = 4\Omega\gamma^l_{S-V}/\Delta\mu$ is the minimum diameter below which the nanowires cannot grow because $\Delta\mu_{eff} < 0$. In Eq. 3.2, we neglect the growth of a wetting layer, which is rather thin in all our samples.

Comparison of theoretical and experimental $L(D)$ dependences enables us to estimate several important characteristics of nanowire formation. From fitting the $L(D)$ curve in Figure 3.6 by Eq. 3.2 we obtain $L_0 = 708$ nm and $D_{min} = 8$ nm. For further estimates we use the parameters of InP from Refs. [29,30]. The elementary volume per III-V pair $\Omega = 0.0506$ nm^3 and the (110) surface energy of the zincblende phase $\gamma_{ZB}^{l} = 1.3$ J/m^2. According to this analysis, the formation of a wurtzite nanowire could lead to up to a 25% decrease of surface energy ($\gamma_{WZ}^{l} = 0.975$ J/m^2). Taking into account possible polytypism between zincblende and wurtzite structure, we obtain reasonable estimates of $\Delta\mu_{eff}/k_B T = 2.5 - 3.25$ and $K = 0.37 - 0.63$ nm/s. The values of $\Delta\mu = 150 - 210$ meV and the vapor supersaturation $\Phi = exp(\Delta\mu/k_B T) - 1 = 11 - 25$ are comparable to the case of MBE growth [27].

3.5 Sidewall Diffusion in Nanowire Growth Modeling

The predictions in the previous section ignore the contribution of sidewall diffusion of adatoms, because the $L(D)$ dependence is mainly increasing, which indicates a small diffusion effect. In this section we explicitly show the effect of the diffusion contribution and compare to diffusion-dominated processes such as MBE growth.

In order to compare the relative effects of direct adatom impingement on the catalyst nanoparticle and diffusion up the nanowire sidewall, we utilize the following equation which splits the growth rate dL/dt into these two separate processes. [26]

$$\frac{dL}{dt} \propto mR_{np} + nR_{dif} \tag{3.3}$$

The arrival rates of the growth species per unit area are R_{np} and R_{dif}, respectively. m and n are weighting factors for the relative contributions, given by the area receiving the reactants divided by the nanowire growth layer. They are given as:

$$m = \frac{\left(\frac{1}{2}\right)\pi D^2}{\left(\frac{1}{4}\right)\pi D^2} \quad ; \quad n = \frac{\pi D \lambda}{\left(\frac{1}{4}\right)\pi D^2}. \tag{3.4}$$

λ is the diffusion length of the adatoms up the sidewall of the nanowire. Assuming equal rates of precursor impingement, $R_{np} = R_{dif} = (1/2)R$, we arrive at Eq. 3.5.

$$\frac{dL}{dt} \propto R\left(1 + \frac{2\lambda}{D}\right) \tag{3.5}$$

The actual growth rate depends on the difference in chemical potentials between the vapor and solid phases, $\Delta\mu = \Delta\mu_V - \Delta\mu_S$. As before, due to the Gibbs-Thomson effect, the chemical potential in an Au nanoparticle increases for smaller nanoparticles. This gives us the added term to the bulk chemical potential, $4\Omega\gamma_{S-V}^{l}/D$, where Ω is the volume per III-V pair, and γ_{S-V}^{l} is the surface energy of the lateral solid-vapor interface of the Au nanoparticle. So we use the term $\Delta\mu_{eff} = \Delta\mu - 4\Omega\gamma_{S-V}^{l}/D$ as the effective difference in chemical potentials. We also assume still that the growth rate R is proportional to $\left(\Delta\mu_{eff}/k_B T\right)^2$.

Given these assumptions, if we replace R with a crystallization coefficient K and the $\left(\Delta\mu_{eff}/k_B T\right)^2$ term, we get

$$\frac{dL}{dt} = K\left(\frac{\Delta\mu}{k_B T} - \frac{4\Omega\gamma_{S-V}^{l}}{D k_B T}\right)^2 \times \left(1 + \frac{2\lambda}{D}\right). \tag{3.6}$$

For processes that are mainly dependent on direct impingement of precursors to the catalyst nanoparticle ($\lambda \ll D$), dL/dt has an increasing dependence on D due to the Gibbs-Thomson effect. For nanowires with long diffusion lengths ($\lambda \gg D$) and where the supersaturation is large, the Gibbs-Thomson effect can be ignored, and dL/dt has a decreasing dependence on D. If we integrate dL/dt, we get the expression

$$L = L_0\left(1 - \frac{D_{min}}{D}\right)\left(1 + \frac{2\lambda}{D}\right), \text{where } D_{min} = \frac{4\Omega\gamma_{S-V}^{l}}{\Delta\mu} \text{ and } L_0 = Kt\left(\frac{\Delta\mu}{\mathrm{k_B T}}\right)^2. \qquad 3.7$$

This L(D) dependence is similar to Eq. 3.2, except with the added $(1 + 2\lambda/D)$ term due to the sidewall diffusion of the growth species into the catalyst nanoparticle.

3.6 Sidewall Diffusion Fitting to Experimental Results

The experimental $L(D)$ nanowire dependence from Figure 3.6 was fitted using the expression in Eq. 3.7 to determine which effects dominated in the growth, be it the Gibbs-Thomson effect (exhibited by large D_{min}), or diffusion up the sidewalls (exhibited by large λ). The Gibbs-Thomson possibility would exhibit an increasing $L(D)$ dependence, the diffusion possibility would exhibit a decreasing $L(D)$ dependence, and if neither effect is critical in the range of diameters, one would observe nearly constant $L(D)$ dependence even for the smallest nanowires.

Figure 3.7 shows the standard deviations of the nanowire lengths vs. diameter and the fitted curve. The resulting fitted parameters were D_{min} = 13.5 nm, L_0 = 1230 nm and λ = 29 nm. The diffusion length λ is very small compared to MBE growth, which can be in the range of 1 – 10 µm [27]. Given the strong increasing $L(D)$ dependence, the Gibbs-Thomson effect seems to have the largest effect on the nanowire growth, particularly for the smallest diameters. If we constrain λ to larger values comparable to MBE growth and fit the other parameters, the curve results in artificially high D_{min} values and a strong decreasing $L(D)$ dependence which does not fit the experimental data.

In conclusion, we have shown that for our MOCVD-grown nanowires, growth is limited by the Gibbs-Thomson effect, and the diffusion length λ is very small, much smaller than in typical MBE growth which can reach 1 – 10 µm [27].

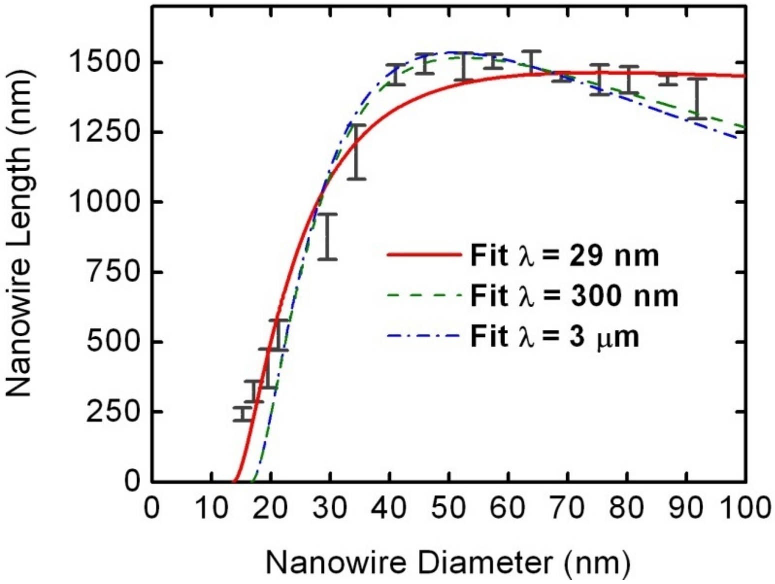

Figure 3.7 Standard deviations of nanowire length vs. diameter (gray). The solid line shows the fit to equation 3. The dotted lines show fits assuming longer diffusion lengths as in MBE growth.

3.7 Nanowire Crystal Phase Modeling

Experimental evidence [21,22,24] strongly suggests that the formation of wurtzite phase in zincblende III-V nanowires is related to their small radius, resulting in a larger relative contribution of the nanowire sidewall surfaces to the total free energy of fully formed wires [31-33], or monolayer islands mediating the growth of the wire top [34].

We now show results of transmission electron microscopy (TEM) study of crystallographic structure in InP nanowires of different diameters similar to those grown in Figure 3.6. Figure 3.8 shows a typical InP nanowire with a diameter of 8 nm imaged on the $[1\bar{2}10]$ zone axis. For the smaller nanowires, only the wurtzite phase is typically observed, without twinning defects. This is indicated in the Fast Fourier Transform in Figure 3.8, which shows a clear wurtzite pattern.

For nanowires larger than ~40 nm in diameter, the twinning between wurtzite and zincblende phases becomes quite frequent, which can clearly be seen by the banding in Figure 3.9. The diffraction pattern also shows a spread between diffraction peaks seen in both wurtzite and zincblende phases, as indicated by the circled section of the pattern.

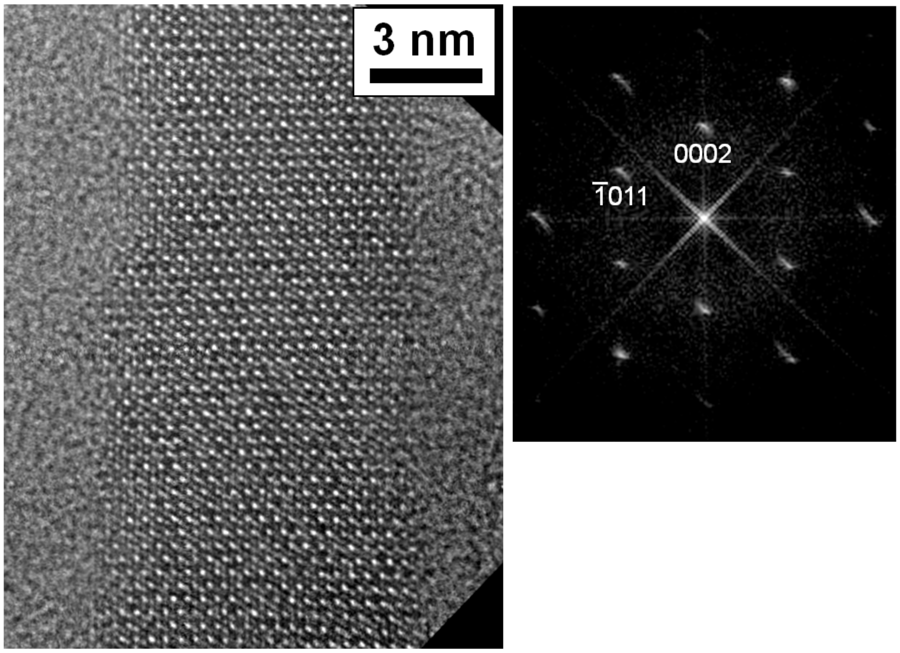

Figure 3.8 Transmission Electron Microscope images of InP nanowires. (a) shows a nanowire with 8 nm diameter and a pure wurtzite phase as indicated by the fast Fourier transform to the right.

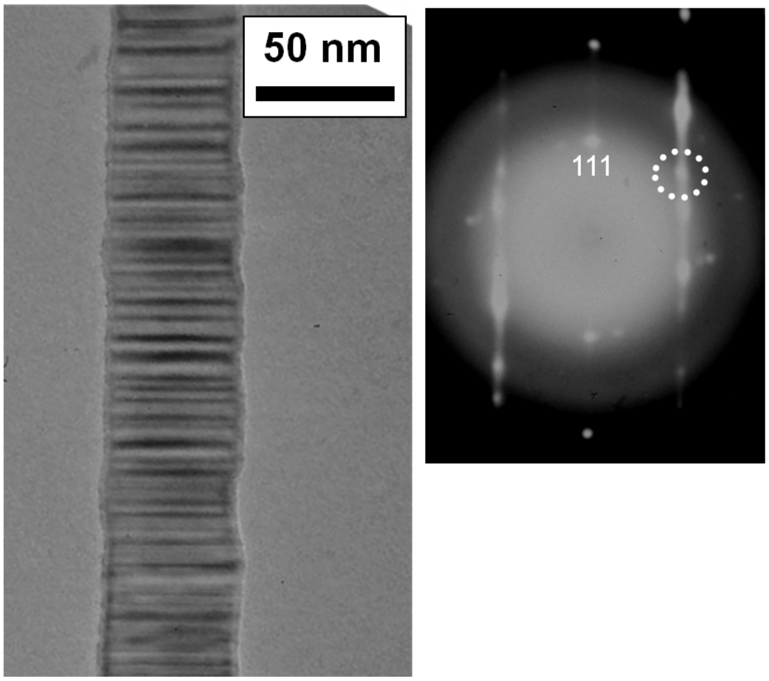

Figure 3.9 TEM image of a larger 45 nm diameter nanowire. Twinning defects are clearly seen in this image. The electron diffraction pattern also shows the hybrid of typical zincblende and wurtzite patterns.

Our model for predicting the nanowire crystal phase is as follows. Consider a single cylindrical nanowire, growing perpendicular to the (111) substrate. During growth, $N = \pi D^2 L / 4\Omega$ InP pairs are deposited onto the substrate to form a nanowire of diameter D and length L (Fig. 3). Assume that D is below the critical diameter limit $D_e(\varepsilon_0)$ for coherent nanowire growth. Neglecting a small variation in the nanoparticle size and shape which may occur during the growth, the difference of free energies in final (nanowire) and initial (the nanoparticle on a bare substrate) states of the system is given by

$$\Delta F = -\frac{\pi D^2 L}{4\Omega}\Delta\mu + \pi D L \gamma_{S-V}^{l} + \frac{E}{1-\nu}\frac{\pi D^2 L}{4}\frac{\varepsilon_o^2}{1 + A_\nu L/D}\,. \qquad 3.8$$

The first term on the right hand side represents the change of volume free energy due to the vapor-solid phase transition. The second term gives the energy required to form the sidewall surface. The last term describes the strain-induced elastic contribution to the free energy due to the lattice mismatch; E is the Young modulus and ν the Poisson ratio of nanowire material. The coefficient A_ν depends on ν. For further analysis it is convenient to re-write Eq. 3.8 in terms of the normalized formation energy per III-V pair $\Delta f \equiv \Delta F/N$. Comparison of the different terms in Eq. 3.8 shows that the strain-induced contribution to Δf scales as D/L and cancels at $L/D \to \infty$. While the elastic energy determines the value of $D_e(\varepsilon_0)$, the stress relaxation involves the layer of thickness of few D at most and has little effect on the formation of longer nanowires.

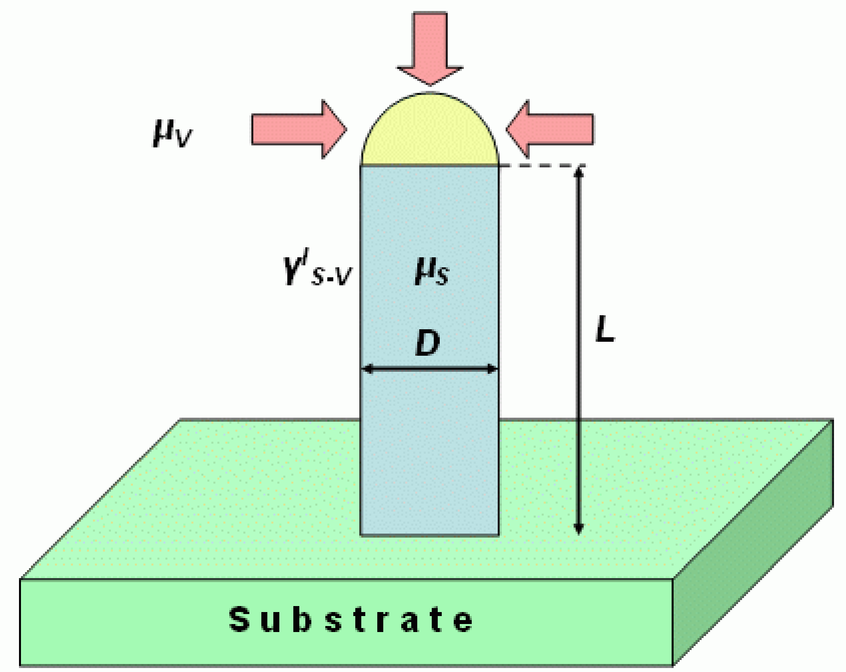

Figure 3.10 Schematics of nanowire growth: μ_V **is the vapor chemical potential,** μ_S **is the chemical potential in nanowire and** γ^l_{S-V} **is the lateral surface energy at the solid-vapor interface. The values of** μ_S **and** γ^l_{S-V} **depend on the crystallographic phase in the nanowire.**

Therefore, for the analysis of structural stability in the first approximation it is sufficient to ignore the strain-induced term from Eq. 3.8. This normalized expression $\Delta f \equiv \Delta F/N$ is then written as

$$\Delta f_k = -\Delta\mu_k + \frac{4\Omega\gamma_k^l}{D} \qquad 3.9$$

Eq. 3.9 should be treated for zincblende and wurtzite nanowires (*k* = zincblende or wurtzite), with $\Delta\mu_{ZB} = \mu_V - \mu_{ZB} \equiv \Delta\mu$ being the difference of chemical potentials in the vapor and in the zincblende phase, $\Delta\mu_{WZ} = \mu_V - \mu_{WZ}$ the corresponding value for the wurtzite phase, $\gamma_{ZB}^l = \gamma_{ZB}^{(110)}$ the lateral surface energy of zincblende and γ_{WZ}^l the lateral surface energy of wurtzite nanowires. The wurtzite phase should be predominant when $\Delta f_{WZ} < \Delta f_{ZB}$.

Nanowire formation is possible only at $\Delta f < 0$. At positive Δf, the vapor supersaturation is insufficient to overcome the Gibbs-Thomson effect. These two conditions give the range of diameters $D_{min} < D < D_c$, where the wurtzite phase should be prevalent. Characteristic diameters D_{min} and D_c are given by

$$D_{min} = \frac{4\tau}{(\Delta\mu/\psi - 1)} D_0 \quad ; \quad D_c = 4(1-\tau)D_0 \qquad 3.10$$

with $D_0 = \frac{\Omega\gamma_{ZB}^{(110)}}{\psi}$, $\psi = \mu_{WZ} - \mu_{ZB}$ and $\tau = \gamma_{WZ}^l/\gamma_{ZB}^l$. The value of D_{min} is equivalent to the Givargizov-Chernov expression in Eq. 3.2. At $D < D_{min}$ the formation of nanowires is thermodynamically forbidden. The parameter D_c therefore determines the critical diameter for the zincblende to wurtzite structural transition. The parameter ψ represents the difference of cohesive energies for the formation of bulk wurtzite and zincblende crystals. For all zincblende materials $\psi > 0$, since the zincblende phase is stable in the bulk form. The surface energy coefficient τ equals the ratio of wurtzite to zincblende lateral surface energy. According to Eq. 3.10, the structural transition may occur only when $\tau < 1$, when the surface energy of wurtzite structure is lower than that of zincblende. The characteristic diameter D_0 can be estimated from the available data on Ω, ψ and $\gamma_{ZB}^{(110)}$ [29-34].

Surface dangling bonds on the nanowire lateral facets have a significant effect on the nanowire structural stability at smaller diameters [31-33]. In order to estimate the coefficient τ, one can count the number of dangling bonds j on the lateral facets of zincblende and wurtzite nanowires, perpendicular to the (111) surface [33]. This procedure is illustrated in Fig. 4.

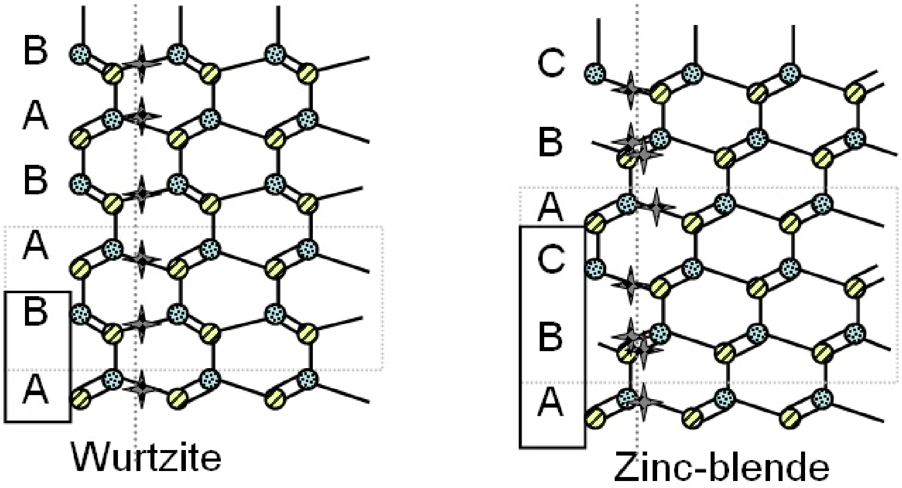

Figure 3.11 Side view of wurtzite and zincblende structures. Star symbols indicate the dangling bonds on the lateral facets. The number of dangling bonds j equals 1 per layer in the wurtzite and 4/3 per layer in the zincblende phase.

It is seen that j equals 1 bond per III-V layer in the wurtzite and 4/3 bonds per III-V layer in the zincblende phase. From these considerations we arrive at τ = 3/4, the formation of wurtzite phase thus leads to an approximate 25% reduction in the sidewall surface energy. From the second Eq. 3.10, the critical diameter for zincblende to wurtzite transition is determined to be $D_c = D_0$. Our analysis shows that the diameter D_{min} can be made arbitrary small by increasing the vapor supersaturation $\Delta\mu$. The critical diameter D_c does not depend on the lattice mismatch, whereas the critical diameter for the epitaxial growth of coherent nanowires D_e is determined mainly by ε_0.

Table 3.1 shows a summary of the estimates for D_c, obtained from Eq. 3.10 at τ = 3/4 for different material systems. We use the data of Ref. [29] for the (110) surface energies of zincblende crystals. The values of ψ are taken from Ref. [31]. We also present the experimental values of D for different material-substrate combinations [18]. Comparison of D_c and D_e shows that the InAs and InP nanowires on the silicon substrates can be grown epitaxially only in the wurtzite phase ($D_e < D_c$). The situation is different for the epitaxial InP nanowires on the GaAs substrate ($D_e > D_c$), which should form predominantly in the wurtzite phase below 60 nm and in the zincblende phase for larger diameters between 60 and 96 nm. Because the difference in the formation energies $\Delta f_{WZ} - \Delta f_{ZB}$ near D_c is much smaller than $k_B T$ = 64 meV, thermal fluctuations will create rotational twins between wurtzite and zincblende structure.

Material system	E_0 (%)	D_e (nm)	Ω (nm^3)	$\gamma_{ZB}^{(110)}$ (J/m^2)	ψ (meV/pair)	D_c (nm)
InAs/Si	**11.6**	**26**	**0.0567**	**1.0**	**10.6**	**34**
InP/Si	**8.1**	**36**	**0.0506**	**1.3**	**6.8**	**60**
InP/GaAs	**4.1**	**96**	**0.0506**	**1.3**	**6.8**	**60**

Table 3.1. Critical diameters and material parameters for different III-V materials on lattice-mismatched substrates.

The theoretical prediction is qualitatively in excellent agreement with the experimental data from the MOCVD-grown nanowires. The smaller diameter nanowires exhibit single crystalline wurtzite phase without twinning, whereas the larger nanowires have mixed wurtzite and zincblende portions alternating back and forth, at scales ranging from a few to 20 nm. The critical transition diameter experimentally observed was somewhat smaller than the theoretical value, possibly due to inaccuracies and some of the simplifications of the analysis.

To conclude, due to the interplay of strain-induced and surface energy effects on the growth performance, the technologically important fabrication of III-V nanowires enables one to combine two major advantages: 1) coherent growth and 2) formation of pure wurtzite phase nanowires without stacking faults. This requires two conditions: 1) high enough supersaturation of the vapor phase and 2) small enough diameter of nanowire.

This explanation of wurtzite structure in small nanowires is not specific for III-V materials and would apply for other cubic materials, in particular, for silicon. This is important because wurtzite silicon is a semiconductor with the direct band gap transition at the Γ point [35]. Recently, wurtzite silicon was observed experimentally in CVD grown nanowires with the diameters as large as 100 nm [36]. Moreover, zincblende to wurtzite phase transformation can be observed in other nanostructures with low energy wurtzite facets, when the surface energy gain outweighs the difference in bulk cohesive energies.

4 GaAs/AlGaAs/InGaAs Nanoneedles

Integration of III-V optoelectronic materials with silicon CMOS processing is an important area of research for realizing active optoelectronic devices integrated with silicon electronics, particularly devices that operate at silicon-transparent wavelengths. Devices such as lasers, LEDs and photodetectors require low defect densities and the ability to grow heterostructures. VLS-grown nanowires have proved promising for this application, but their size is limited to critical diameters by their lattice-mismatch with the substrate and crystal phase transitions [37,16]. The metal catalysts used in VLS growth may also be detrimental to silicon CMOS devices due to their formation of deep level defects, which is particularly an issue with Au.

In this chapter, we present the growth of catalyst-free ultra-sharp GaAs-based nanoneedle structures, with record narrow tip diameters, sharp 6-9° taper angles, lengths up to 10 µm and base diameters up to 1.3 µm [38]. A diagram of the typical structure of these nanoneedles is shown in Figure 4.1(a). Figure 4.1(b) shows an SEM image of a nanoneedle grown on GaAs. The nanoneedles have ultrasharp catalyst-free tips, as shown in the inset of Figure 4.1(b). The tips often have diameters less than a few nm, contrary to typical VLS growth [17] for one-dimensional nanostructures.

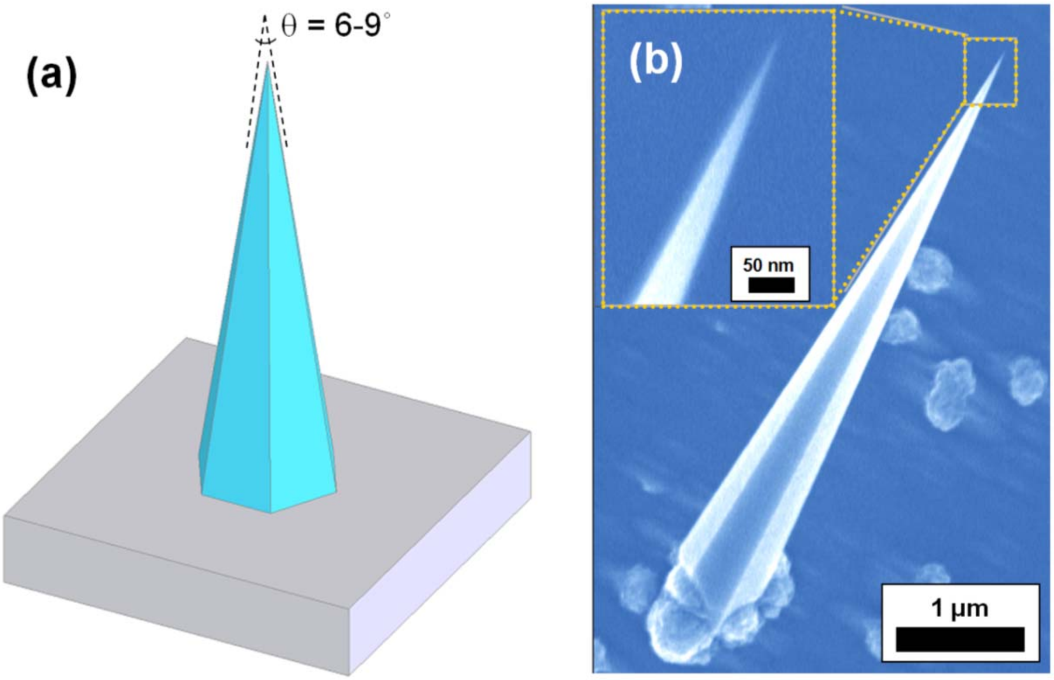

Figure 4.1 (a) schematic of a typical nanoneedle, with a 6-9° taper and hexagonal cross-section. (b) SEM image of a GaAs nanoneedle grown on (111)GaAs. The inset shows the sharp taper and extremely narrow tip, often less than a few nm in diameter.

The nanoneedles grow on GaAs, silicon and sapphire substrates under the same growth conditions, resulting in the same nanoneedle physical characteristics and bright room-temperature photoluminescence. For (111)Si and (111)GaAs substrates, the tips of the nanoneedles (c-axes) align to the substrate normal, as shown in Figure 4.1(a). The growths are conducted at 380 to 420 °C, temperatures even lower than that of typical VLS grown nanowires, making the process ideal for silicon-CMOS processes, which require low growth temperatures of < 450 °C [1]. The nanoneedles can also be large enough to facilitate device fabrication using top-down, standard processing techniques. The longest nanoneedle growths of 180 min yield ~10 μm long nanoneedles. The nanoneedle growth mode also allows for ternary compounds and heterostructures, as we demonstrate by growing pure InGaAs nanoneedles, as well as InGaAs and AlGaAs heterostructures and quantum wells in the nanoneedles [39].

The nanoneedles are also single-crystal wurtzite GaAs, free of the twinning defects and crystal phase switching typically seen in nanowires [40]. This was the first observation of such large samples of wurtzite GaAs outside of high-pressure experiments. The single needles exhibit bright room-temperature micro-photoluminescence.

Nanostructures with ultra-sharp tips and narrow tapers [41] are also of great interest due to the strong [42,43] electric field enhancement at the tips, which is inversely proportional to the tip diameter [44]. This effect is commonly used for nonlinear optics and applications such as tip-enhanced Raman spectroscopy [45], or for field emission devices. The enhancement is observed in metallic and semiconductor tips [42], and even single-wall carbon nanotubes [42,46,47]. These nanoneedles could prove useful for many other applications such as parallel scanning-probe microscopy devices, attoliter droplet delivery via etched core/shell nanoneedles for biological applications, or direct integration of III-V material on silicon for optoelectronic devices.

4.1 Nanoneedle Growth Mechanism

The nanoneedles are grown using an MOCVD reactor. The wafers are first cleaned and deoxidized before growth. For GaAs, silicon and sapphire substrates, the wafers are first cleaned of organic contaminates by degreasing the wafers for 3 minutes in acetone, methanol, and then deionized water. The GaAs wafers are then deoxidized using a 50% HCl solution for 3 min, or until the surface becomes hydrophobic. Silicon is deoxidized in a 5:1 H_20:HF solution for 3 min. The sapphire does not undergo any deoxidation processes, since sapphire itself is an oxide (Al_2O_3). For GaAs and silicon substrates, the wafers are then mechanically treated to initiate surface roughness to catalyze three-dimensional (3D) GaAs island growth, which may be similar to 3D growth of GaN enabled by surfactants [48]. The nanoneedle growth on sapphire substrates however is spontaneous across the entire surface of the wafer, and does not require the mechanical roughening process.

The wafers are loaded into the MOCVD system immediately after deoxidation. The wafers are annealed at 600 °C for 10 minutes, and then the growth is conducted at 380 – 420 °C. The hydrogen carrier gas and precursor species are passed over the hot wafer spinning at 1400 rpm, at a pressure of 76 torr. The hot wafer causes the precursor material to react on the wafer surface, resulting in controlled growth of the nanoneedles. The group III and V sources used for GaAs growth are triethylgallium and tertiarybutylarsine, which have relatively low decomposition temperatures (300 °C and 380 °C, respectively) [49,50]. These low decomposition temperatures allow for the low growth temperatures, which favor a 3D growth mode rather than typical MOCVD thin-film growths at much higher temperatures of ~600 °C. AlGaAs and InGaAs nanoneedle heterostructures, as well as bulk InGaAs nanoneedles, can be grown by adding trimethylaluminum and trimethylindium [38,39]. However, pure AlAs and InAs nanoneedles cannot be grown with these precursors as of yet. The nanoneedle growth proceeds via conformal deposition of the metal-organic precursor material, with a higher growth rate along the nanoneedle c-axis tip. The growth is linear, with the radius and c-axis growth rates being 5 nm/min and 67 nm/min, respectively.

The nanoneedles typically align to the $\langle 111 \rangle$ crystal directions on GaAs and silicon. Most growths were conducted on $(111)B$ GaAs and (111)Si substrates, and thus the nanoneedles end up growing perpendicular to the substrate surface. The needles have a constant taper angle of 6-9° throughout the growth.

Figure 4.2 shows the growth progression of a typical nanoneedle. The growth begins with precursor material aggregating in certain areas (the mechanically roughened areas for GaAs and silicon substrates) in a 3D growth mode, with needle shapes visible in SEM imaging within the first couple minutes of growth. As the growth continues, subsequent material deposition occurs on the sidewalls and tip coherently forming the single-crystal nanoneedles, with a much higher growth rate along the c-axis direction. The nanoneedle sidewalls do not correspond exactly to any particular low-index zone axis of the crystal. However, in the nanoneedle cross-section, the flat hexagonal sidewalls of the nanoneedle align to the hexagonal $\langle 1\bar{1}00 \rangle$ axes perpendicular to the c-axis, which are in turn aligned to the $\langle 11\bar{2} \rangle$ axes of the cubic substrate.

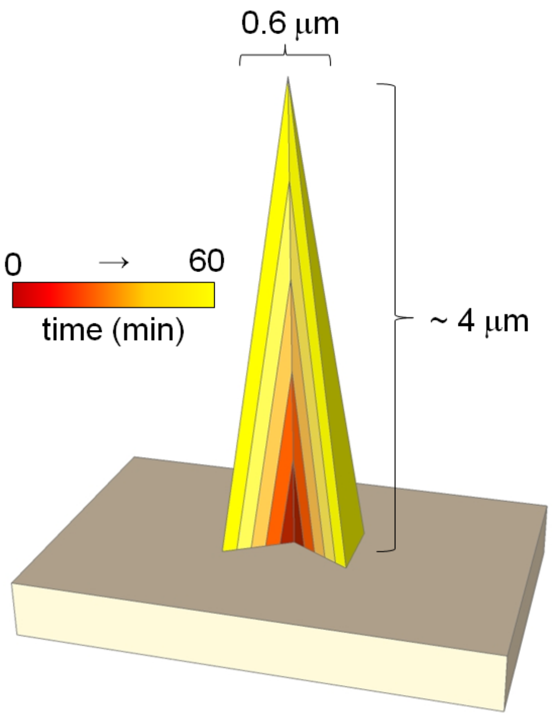

Figure 4.2 Nanoneedle growth progression. The nanoneedles start out at the first few minutes of growth as small needle structures (shown in dark red), and evolve via tip and sidewall deposition of further material, keeping a constant taper angle. 60 minute growths typically result in 4 µm long nanoneedles.

The nanoneedle growth rate of the length and radius dimensions remains roughly linear up to the longest growth times attempted at 180 min. Figure 4.3 shows SEM images of the progression of GaAs nanoneedle growth on sapphire substrate vs. time, scaled relative to each other. The smallest nanoneedle in Figure 4.3(a), grown for 1.5 min (zoomed in 10 x) is about 120 nm long and already shows the needle shape as being similar to the shape of the nanoneedles from 60 minute growths. Nanoneedles smaller than this are unable to be seen clearly in our SEM due to resolution limitations. The other SEM images in Figure 4.3(b)-(d) show that the needle shape and taper angle stay consistent for up to 80 minute growths, yielding anywhere from 120 nm to 5 µm long nanoneedles. At 180 minutes, the nanoneedle growth rate along the c-axis starts to reduce, with while the sidewall deposition stays relatively constant, resulting in a larger taper angle.

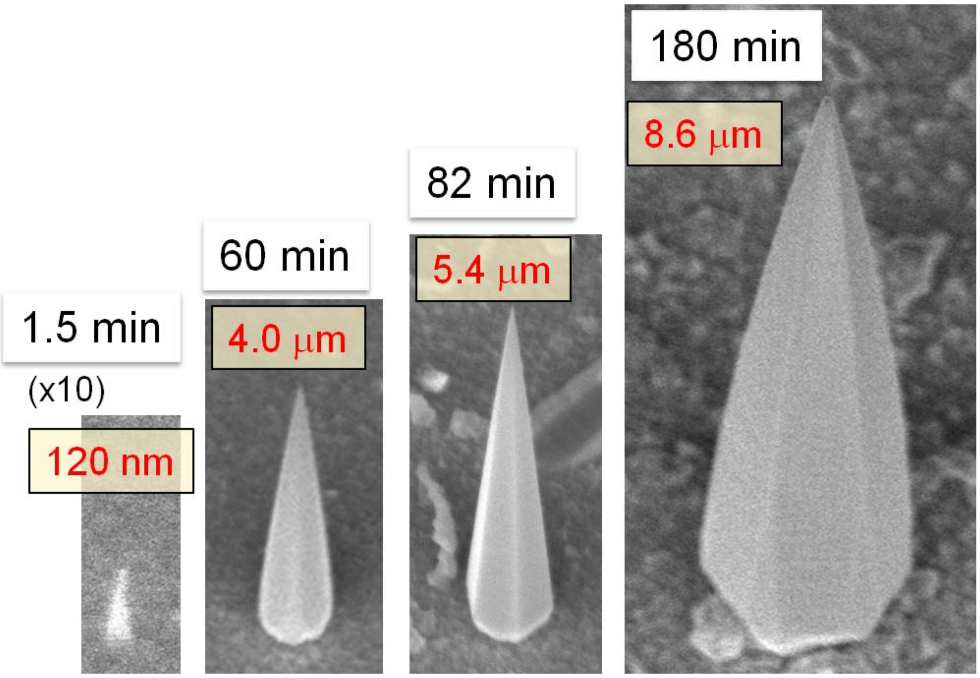

Figure 4.3 SEM images of GaAs nanoneedles grown on sapphire for various growth times, scaled relative to each other. Nanoneedle growth times and nanoneedle lengths are labeled. The smallest (1.5 min) growth is zoomed in 10x relative to the other images. The tapered nanoneedle shape is apparent even at 1.5 min, and the tip and sidewall deposition increases in a linear fashion up to at least 82 min. By 180 min, the growth slows down along the c-axis, resulting in a larger taper angle.

Figure 4.4 shows SEM images of two nanoneedles grown on a (001)GaAs substrate. The nanoneedles grow mainly along the two degenerate $\langle 111 \rangle$B orientations, so for the (001) substrate the nanoneedles can cross each other. In this image we observe that the nanoneedles have enveloped each other during growth. By increasing or decreasing the growth time, the nanoneedle lengths are correspondingly increased or decreased without changing the nanoneedle shape, taper angle or tip dimension. These observations elucidate that the growth of nanoneedles is via continuous deposition on their initial 3D surface, favored along the $[0001]$ wurtzite crystal orientation, as explained in the schematic in Figure 4.2.

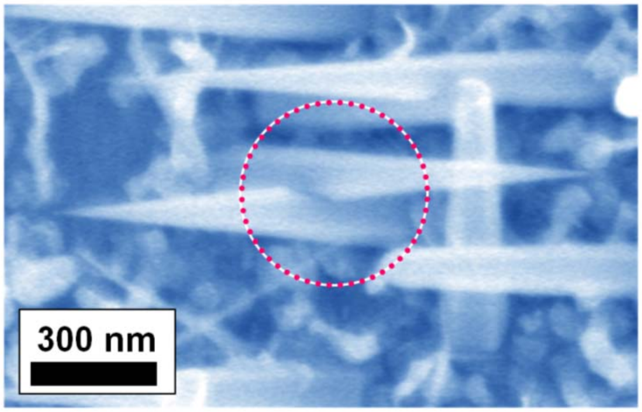

Figure 4.4 Two nanoneedles which have enveloped each other during growth. This shows that the growth mode is via conformal deposition on both the sidewalls and tips, unlike nanowire VLS growth.

Some nanoneedles wiped off of the substrates onto the carbon film grids show a small section of reverse tapering at their base, as shown in Figure 4.5(a). This is a result of competition of the 3D nanoneedle growth with a small amount of polycrystalline thin-film GaAs growth. The thin-film growth rate is very slow at this low temperature of ~400 °C, compared to the nanoneedle growth. Figure 4.5(b) shows an approximate diagram of the layer deposition vs. time. As the thin film deposits around the nanoneedle, it prevents the subsequent layers of nanoneedle growth from directly contacting the substrate, resulting in the reverse-tapering effect.

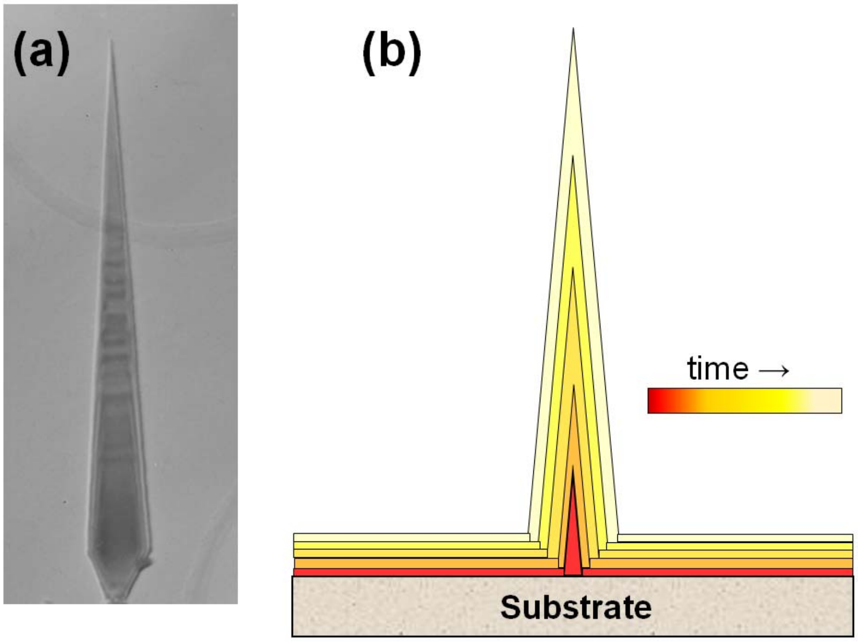

Figure 4.5 (a) TEM image of nanoneedle.

Tilted SEM images also show the presence of a small amount of thin-film growth. Figure 4.6 shows a cleaved edge of a sapphire wafer which had GaAs nanoneedles grown on it for 60 minutes. It can be seen here that the surface has a ~200 nm layer of thin film growth, in addition to the nanoneedles growth. The thin film growth rate is typically consistent at about 200 nm/hr.

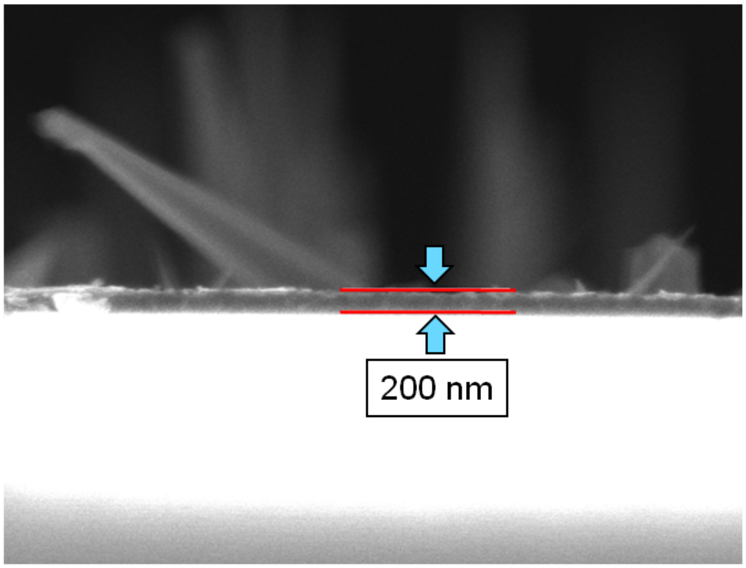

Figure 4.6 (a) SEM image of cleaved edge of a sapphire wafer with nanoneedles grown for 60 min. The thin-film growth is 200 nm thick.

Typical SEM images of nanoneedles grown on a (111)B GaAs substrate viewed both normal to the substrate and tilted 30° are shown in Figure 4.7. The white hexagonal shapes in the first image show the cross-section of the nanoneedles, which are aligned to each other. The tilted image shows that these nanoneedles are sharp, and have a length of 2 – 3 µm, which takes 38 min of growth time.

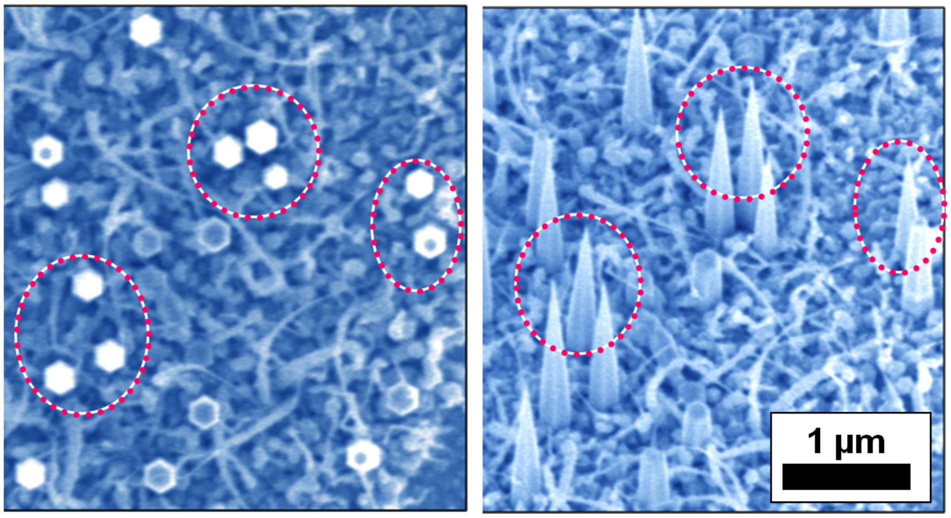

Figure 4.7 Nanoneedles grown on a GaAs (111)B substrate, viewed top-down (left) and tilted by 30° (right) indicating the uniformity and alignment of the $[0001]$ nanoneedle growth axis to the $\langle 111\rangle$B substrate directions.

4.2 Wurtzite Nanoneedle Alignment to Cubic Substrate

Figure 4.8 shows the relation between the wurtzite GaAs nanoneedle crystal orientation and the (111) cubic (zincblende) substrates (GaAs or silicon). The $\langle 1\bar{1}00\rangle$ family of zone axes on the nanoneedle, which lie perpendicular to the flat edges of the nanoneedle hexagonal cross-section, align to the $\langle 2\bar{1}\bar{1}\rangle$ family of cubic substrate zone axes. The $\langle 11\bar{2}0\rangle$ family of zone axes on the nanoneedle, which lie perpendicular to the corners of the nanoneedle cross-section, align to the $\langle 01\bar{1}\rangle$ family of zone axes on the cubic substrate.

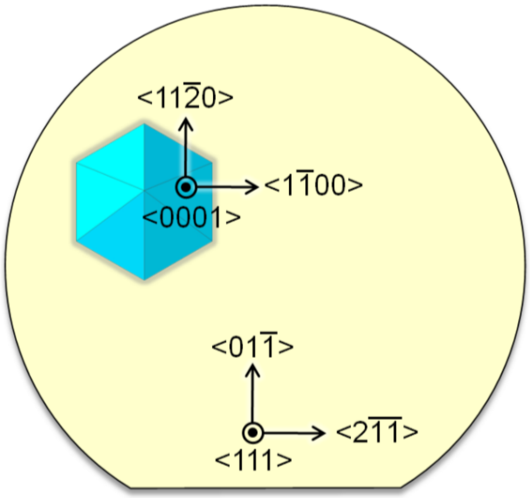

Figure 4.8 Relative orientations of the wurtzite nanoneedles and the cubic substrates.

The nanoneedle $\langle 1\bar{1}00 \rangle$ axes align to the cubic substrate $\langle 111 \rangle$ axes due to the similar surface and symmetry of the hexagonal and cubic crystal systems in those crystal directions. This six-fold symmetry is shown in Figure 4.9. The labeling of hexagonal indices is shown in Figure 4.9. This system has three vectors perpendicular to the c-axis, which are constrained by the relation $a_3 = -(a_1 + a_2)$. The result is that zone axes with same a_1, a_2 and a_3 index numbers simply transposed, are symmetric zone axes, making it more clear which zone axes are analogous to each other.

The cubic indices also have hexagonal symmetry in the plane perpendicular to the $\langle 111 \rangle$ axis as shown. In the diagram of the cube in Figure 4.9, there are six zone axes that line up with the corners of the cube, which are $\langle \bar{1}\bar{1}2 \rangle$ type, and six others which line up with the middle of the edges of the cube, which are $\langle 1\bar{1}0 \rangle$ type, as shown in the red circles. It is important to note that the zincblende (GaAs) and diamond cubic (silicon) structures only have three-fold symmetry in this plane technically, but the effects of this are not critical for the current discussion.

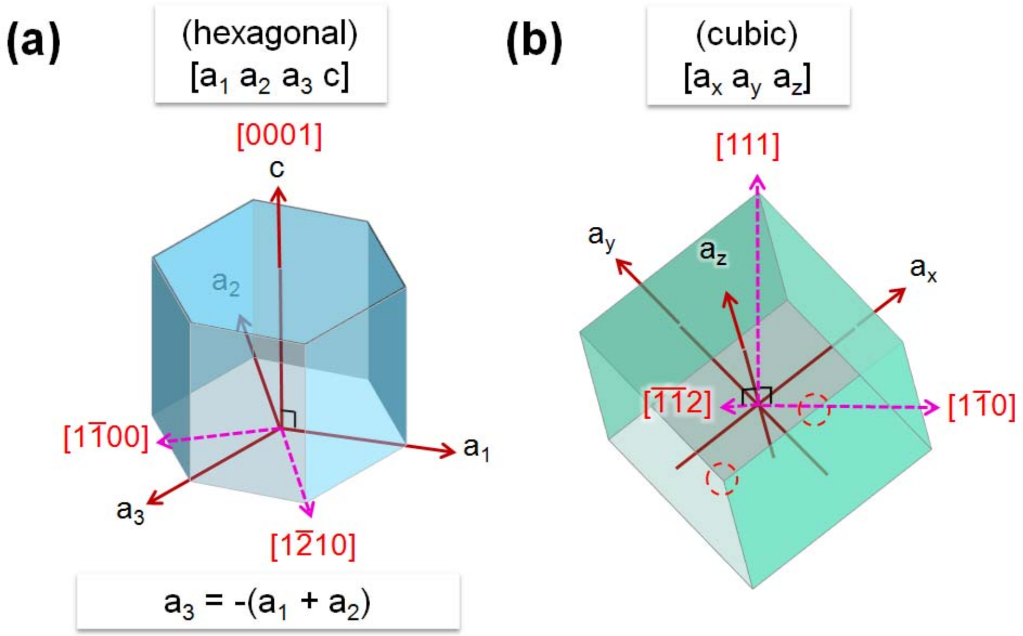

Figure 4.9 Comparison of hexagonal and cubic crystal indices. Each of the indices have a six-fold rotational symmetry about their axes shown oriented in the vertical direction.

4.3 GaAs Nanoneedle Growth on Silicon and Sapphire

The GaAs nanoneedles are grown on silicon substrates using the same growth conditions and exhibit the same characteristics, despite the 4% lattice mismatch between GaAs and silicon. Figure 4.10 shows 30° tilted and top-down views of a 4 µm long nanoneedle grown on an off-cut (111)Si substrate. The lattice-mismatched GaAs nanoneedles grown on silicon substrates do not appear to be limited by the critical diameter effect seen in VLS-grown nanowires [19,20,18]. This is probably because the nanoneedle growth proceeds by sidewall and tip deposition and thus is not critically dependent on coherency to the substrate as the nanoneedle grows larger, as long as the growth at the sidewall and tip remains coherent to the previous atomic layer. The typical nanoneedle density is ~10^7/cm^2 on GaAs substrates and ~5x10^5/cm^2 for silicon substrates in the roughened areas.

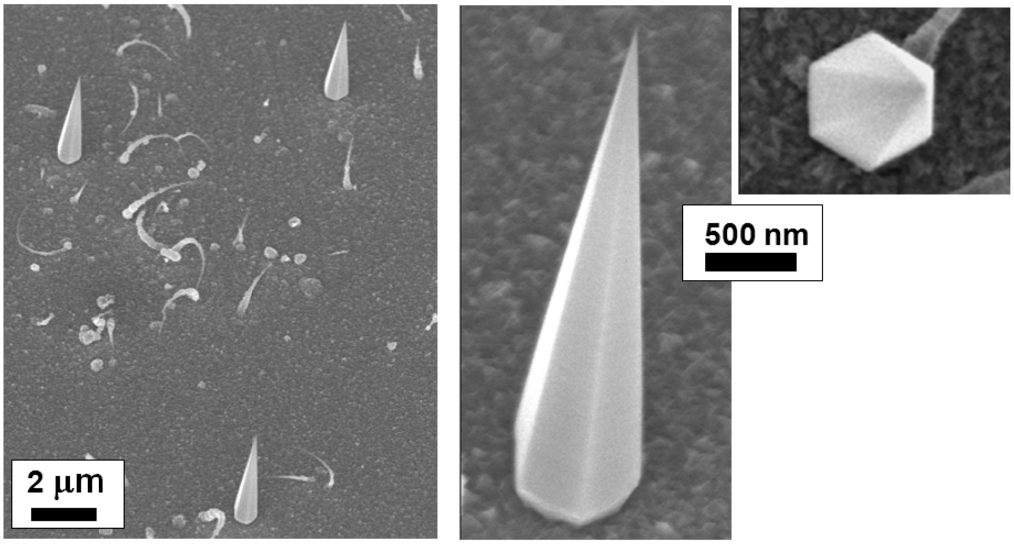

Figure 4.10 GaAs nanoneedle grown on off-cut (111)Si substrate, with views 30° tilted and top-down. The nanoneedle tilt indicates good epitaxial alignment to substrate despite the 4% lattice mismatch.

The nanoneedle shape and optical properties are identical when grown on c-axis sapphire substrates as well. The nanoneedle alignment to the substrate is not as consistent as it is for the (111)GaAs and silicon substrates. However, the nanoneedles grow spontaneously across the entire surface of the sapphire substrate, without the need for mechanical roughening of the surface. Figure 4.11 shows a side-view of a typical nanoneedle growth on c-axis polished sapphire substrate, with vertically-aligned nanoneedles.

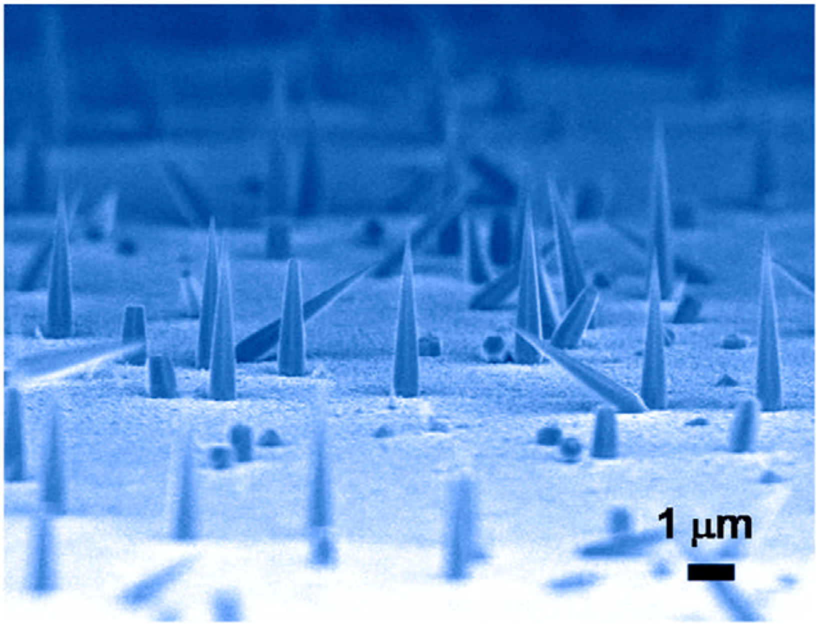

Figure 4.11 Side-view SEM of GaAs nanoneedles grown on c-axis sapphire substrate. The nanoneedles still show alignment to each other and perpendicular to the substrate.

Figure 4.12 shows GaAs nanoneedles grown on c-axis sapphire, viewed normal to the substrate. Unlike the GaAs and silicon substrates, the sapphire substrates show much more randomness in their substrate alignment. However, many of the nanoneedles align to either the substrate normal (c-axis), or in one of three directions 120° from each other and 32.4° tilted up from the plane of the substrate, like in Figure 4.11. These orientations correspond to the normal vectors of the $\{1\bar{1}02\}$ planes of the sapphire.

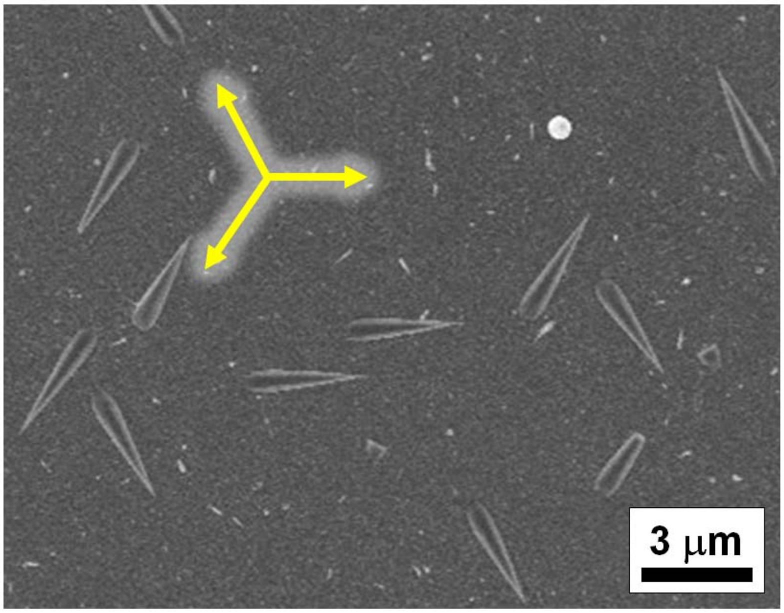

Figure 4.12 SEM of nanoneedles grown on c-axis sapphire, viewed normal to the substrate. Some of the nanoneedles align to three of the $\langle 1\bar{1}02 \rangle$ directions, 120° from each other and tilted 35° up from the substrate. The white spot is a vertically aligned nanoneedle.

The ability to grow the nanoneedles on sapphire substrates makes optical transmission experiments possible. It also highlights that the nanoneedle growth mode is versatile, and may be viable for other substrates beyond those attempted thus far in our work.

4.4 AlGaAs Heterostructure Nanoneedles

The conformal growth mode of the nanoneedles, unlike VLS growth, facilitates synthesis of core-shell heterostructures by simply adding additional precursors during the growth, such as nanoneedles with a GaAs core and an AlGaAs cladding layer [38]. We grew such structures by adding trimethylaluminum for the last 80 nm of growth but keeping all other conditions constant. The samples were then ultrasonicated in H_20 for several minutes. Sonication of these as-grown core-shell nanoneedles resulted in broken tips, exposing the (0001) GaAs surface, as shown in Figure 4.13. The sonicated sample was then selectively etched to remove the GaAs core while leaving the AlGaAs cladding intact, resulting in a hollow AlGaAs nanoneedle.

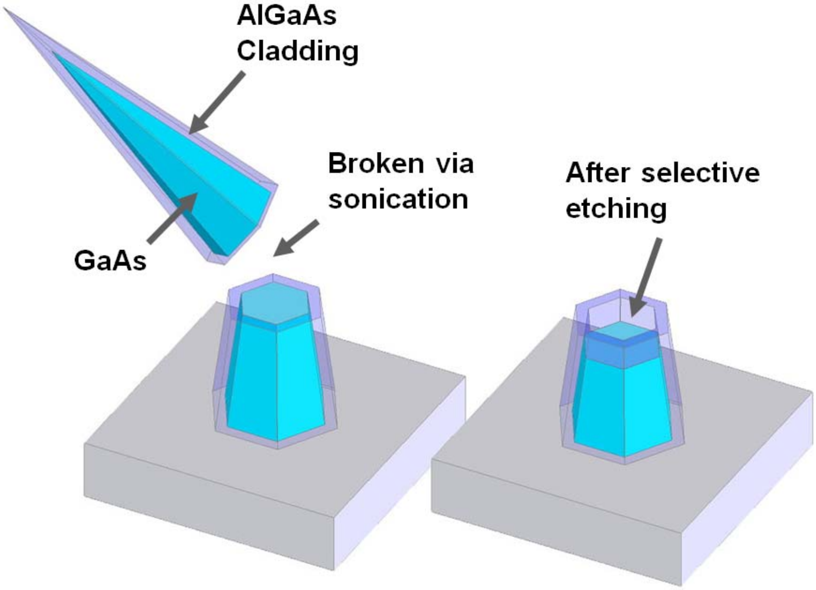

Figure 4.13 Sonication of the AlGaAs-shell, GaAs-core nanoneedles resulted in broken tips. A selective etch was then performed to remove part of the core GaAs material to form hollow nanoneedles, demonstrating the surface-deposition growth mode.

Figure 4.14(a) shows SEM images of some hollow structures fabricated by this method. The outer cladding (shown in purple) is ~80 nm of AlGaAs. The core at the broken tip is GaAs with a radius of ~300 nm. The etching was timed to remove ~150 nm of the GaAs core [51]. Another etched nanoneedle is shown in Figure 4.14(b), having the same AlGaAs wall thickness but with the sonication break closer to the tip. This confirms the surface deposition growth mechanism as well as the ability to grow smooth GaAs/AlGaAs interfaces.

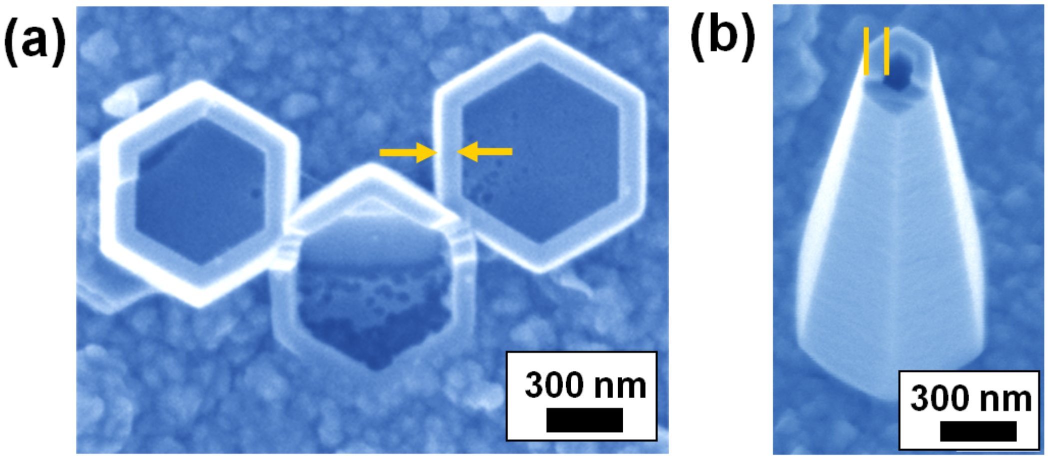

Figure 4.14 (a) A planar-view SEM picture of the fabricated hollow nanoneedles. The AlGaAs cladding with thickness ~80 nm is clearly seen after the removal of the GaAs core. (b) A 20°-tilt view SEM picture of another fabricated hollow nanoneedle with the sonication break closer to the tip, and the same thickness AlGaAs cladding.

4.5 GaAs Nanoneedle Photoluminescence with AlGaAs coating

Very little is known experimentally about the wurtzite GaAs band structure [52]. Hence further experiments on the large bulk-like base structures of the nanoneedles could provide important experimental band structure data and improve understanding of III-V nanowires with wurtzite phase sections. The optical properties of single, as-grown nanoneedles on silicon were characterized using micro-photoluminescence with a 2 µm focused laser spot and a wavelength of 532 nm. Figure 4.15(a) shows low-temperature (4 K) micro-photoluminescence spectra for a GaAs nanoneedle with a 300 nm base radius and a similarly sized GaAs nanoneedle with an additional outer 25 nm-AlGaAs cladding layer. The peak wavelength of the GaAs nanoneedle is at 1.510 eV, which is red-shifted by only 10 meV from the zincblende GaAs band gap at 1.520 eV [53]. No quantization effects are expected due to the large size of the nanoneedles. Hence, these results represent a reliable measurement of near-band-edge emission of wurtzite GaAs. The AlGaAs-coated nanoneedle emits at a similar wavelength and is brighter than the pure GaAs nanoneedle by approximately a factor of two at 4 K. This is not surprising since the AlGaAs layer can effectively passivate the GaAs surface.

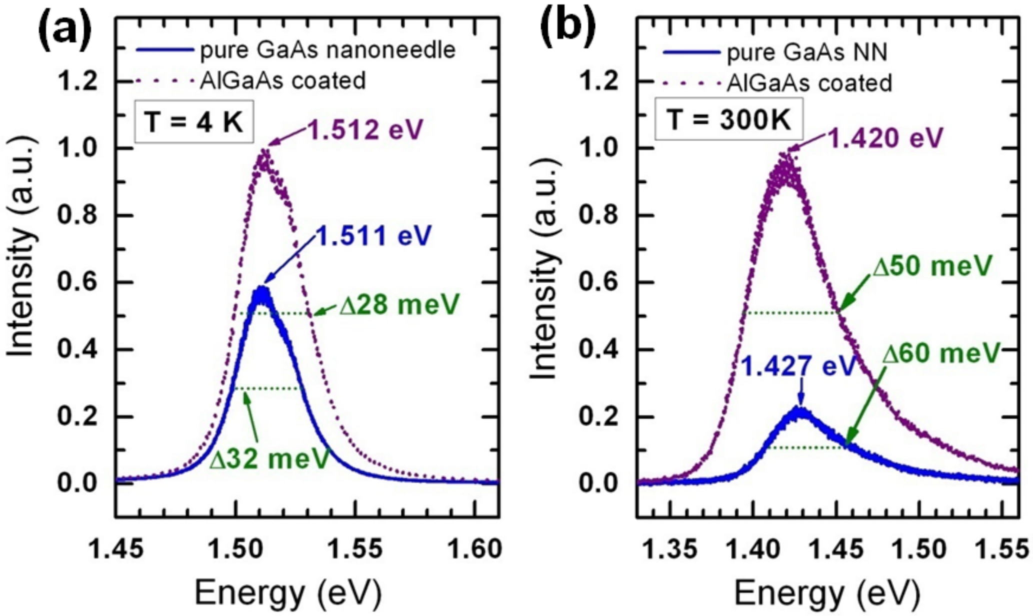

Figure 4.15 micro-photoluminescence spectra of the pure GaAs nanoneedle and AlGaAs-coated GaAs nanoneedle. (a) Low-temperature (4 K) micro-photoluminescence spectrum. Pumping power is 100 μW with a 2 μm focused laser spot and a wavelength of 532 nm. The peak wavelength of the GaAs nanoneedle is at 1.510 eV. The AlGaAs-coated nanoneedle emits at a similar wavelength and is brighter than the pure GaAs nanoneedle by approximately a factor of two. (b) Room temperature (300 K) micro-photoluminescence spectrum. Pumping power is 300 μW. The peak wavelength of the GaAs nanoneedle and AlGaAs-coated nanoneedle are approximately 1.425 eV. The AlGaAs-coated nanoneedle is brighter than the GaAs nanoneedle by a factor of four. The photoluminescence linewidths of the pure GaAs and AlGaAs coated nanoneedles are 50 and 60 meV, respectively.

The room-temperature (300 K) spectra of the same nanoneedles are shown in Figure 4.15. The peak wavelength of the GaAs nanoneedle and AlGaAs-coated nanoneedle are both approximately 1.425 eV, very close to the band edge of undoped, bulk zincblende GaAs at 1.430 eV [53]. The AlGaAs-coated nanoneedle is brighter than the GaAs nanoneedle by a factor of four at room temperature.

These photoluminescence results show that the GaAs nanoneedles have potential to be used for optoelectronic devices integrated with silicon-CMOS processes. The AlGaAs coating layer can also effectively passivate the GaAs surface, reducing the effects of the typical high surface recombination rate in GaAs.

5 InGaAs Quantum Well Nanoneedles

The ability to grow III-V heterostructures is extremely important for constructing efficient devices such as semiconductor lasers. Tuning the quantum well material composition and thickness can create efficient confinement of carriers in the gain region and a more ideal density of states and hence more efficient gain in quantum well lasers compared to that of bulk material. For nanostructure growth as well, the addition of heterostructures can be used in the same way to create more efficient structures for optoelectronic devices, with the potential for silicon integration.

Here, we report the growth of pure InGaAs nanoneedles with indium composition up to 15%, and InGaAs/GaAs quantum well heterostructures grown in GaAs nanoneedles, which are in turn grown on silicon substrates [39]. The nanoneedles retain their sharp tips, narrow tapers and are single-crystal wurtzite phase. These quantum well structures exhibit redshifted, 8x brighter photoluminescence than the typical GaAs nanoneedles, indicating confinement of carriers in the well region. The quantum well nanoneedles can be tuned for emission even below the silicon band edge by increasing the indium composition further. The ability to grow these III-V heterostructures on silicon with radiative emission below the silicon band edge paves the way for bandgap tunability of integrated optoelectronic devices for applications such as lasers, detectors, and other devices, which allow for use of silicon waveguides. The long wavelengths prevent the light from being absorbed in silicon devices.

The InGaAs nanoneedles were grown via MOCVD at 76 torr and 400 – 420 ˚C on silicon substrates for 60 min, resulting in ~4 µm long nanoneedles with ~600 nm wide bases. The metal-organic precursors were trimethylindium (TMIn), triethylgallium and tertiarybutylarsine. The growth conditions were the same as in our previous report of GaAs nanoneedle growths except for the addition of the TMIn flow. The growth is initiated via mechanical roughening of the substrate surface, without the need for metal catalyst particles, contrary to nanowire VLS growth.

5.1 InGaAs Nanoneedle Growth

Three different growths were conducted, with their SEM images shown in Figure 5.1. The first nanoneedle shown in Figure 5.1(a) had a TMIn flow rate of zero. The second growth, shown in Figure 5.1(b), had a TMIn flow rate which resulted in InGaAs material with a nominal 5% indium incorporation. The third growth in Figure 5.1(c) had further increased TMIn flow, resulting in a nominal 15% indium incorporation. The indium incorporation was estimated based on photoluminescence experiments via the following method. The wurtzite GaAs nanoneedles have photoluminescence peaks at 1.509 eV, which is lower than the zincblende band edge at 1.519 eV by 0.7%. In Eq. 5.1, we utilize the quadratic bandgap vs. indium composition equation from ref. [54], with the 0.7% reduction factor to determine the indium composition vs. bandgap for the nanoneedles based on the amount of redshift of the photoluminescence peaks observed.

$$0.993 \times [.419 + .7(1-x) + .4(1-x)^2]\ (\mathrm{eV}) = \mathrm{E_g}(\mathrm{In_xGa_{1\text{-}x}As}) \qquad 5.1$$

As the indium incorporation increases, the nanoneedles become shorter with a curved taper, and take on a more rounded cross-section rather than the hexagonal shape of the pure GaAs nanoneedle. Figure 5.1(d)-(f) shows the top-down views of the 0%, 5% and 15% indium nanoneedles, respectively.

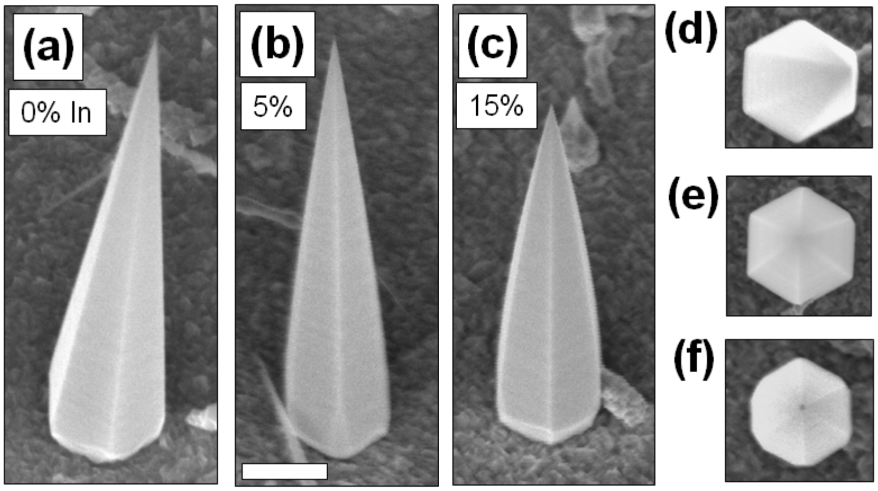

Figure 5.1 (a)-(c): SEM images of $\mathrm{In_xGa_{1\text{-}x}As}$ nanoneedles with indium concentrations of x = 0, 0.05 and 0.15. The images are tilted 30˚ from the normal view. The pure GaAs nanoneedle was grown on a 4˚ off-cut (111)Si wafer. The scale bar (middle) is 500 nm and applies to all the SEM images. (d)-(f): top-down views of the x = 0, 0.05 and 0.15 $\mathrm{In_xGa_{1\text{-}x}As}$ nanoneedles, respectively. The GaAs nanoneedle has a hexagonal cross section, which becomes more rounded for higher indium concentrations.

5.2 Micro-Photoluminescence of InGaAs Nanoneedles

The optical properties of single InGaAs nanoneedles from these growths were characterized using micro-photoluminescence with a 532 nm laser focused to a 2 µm diameter spot with the sample at a temperature of 4 K. The results are shown in Figure

5.2. Quantum confinement effects from the tip are not expected to contribute to the emission, since the quantum confined regions with radius < 10 nm makes up less than 1% of the nanoneedle, and are likely dominated by non-radiative surface recombination.

The peak wavelength of the typical GaAs nanoneedles is at 1.509 eV, redshifted only slightly from bulk zincblende GaAs band edge at 1.519 eV. For the lower TMIn flow sample, the micro-photoluminescence peak is at 1.430 eV due to the increased indium incorporation. This peak corresponds to approximately 5% indium composition based on Eq. 5.1. The higher flow rate nanoneedle has a micro-photoluminescence peak at 1.294 eV, corresponding to approximately 15% indium incorporation. The micro-photoluminescence peak full-width at half-max (FWHM) for the $In_{0.15}Ga_{0.85}As$ (61 meV) is approximately twice that of the pure GaAs (35 meV), and the intensity is reduced by 50%. The micro-photoluminescence peak position does not vary when the excitation laser spot is moved from the base to near the tip of a nanoneedle, which shows the indium distribution is fairly uniform.

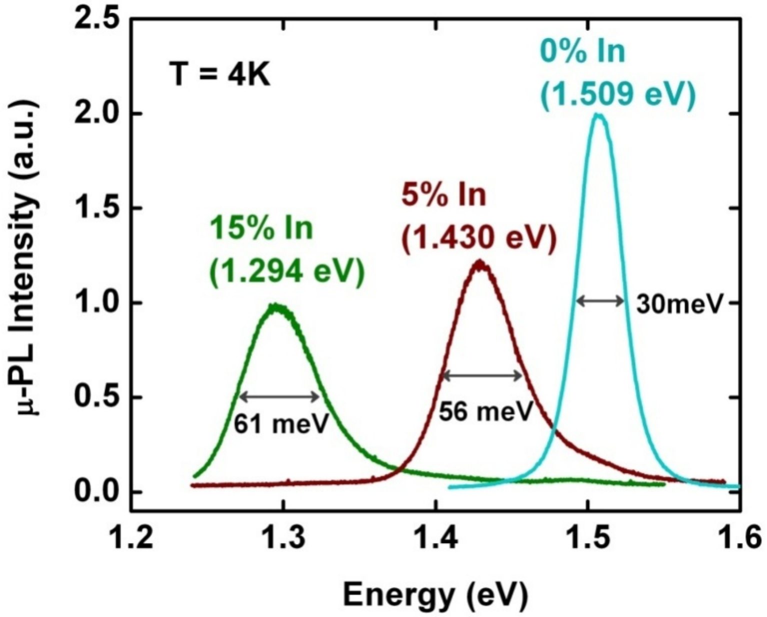

Figure 5.2 Micro-photoluminescence spectra of $In_xGa_{1-x}As$ nanoneedles with x = 0, 0.05 and 0.15. The photoluminescence peak energy redshifts with increasing indium incorporation.

Previously, growth of the nanoneedle structure was shown to be via preferential deposition along the c-axis [38]. We also reported a core-shell nanoneedle structure with sharp AlGaAs/GaAs heterojunction interfaces. Here, we first determined the growth rate of InGaAs and GaAs nanoneedles with several runs having different growth times. The nanoneedle radii and lengths have a linear dependence on growth time, and the growth rate on the nanoneedle sidewalls is 5 nm/min. We grew three quantum well core-shell layered structures with nominal well region thickness of 15, 10 and 5 nm using the 15% indium TMIn flow rate, as shown in Figure 5.3. In this InGaAs heterostructure case, the growth steps start with a 60-minute GaAs core, $In_{0.15}Ga_{0.85}As$ for one to three minutes, and 10 more minutes of GaAs to form an outer shell to confine carriers in the InGaAs region. All growth conditions were held constant, except for the flow of TMIn.

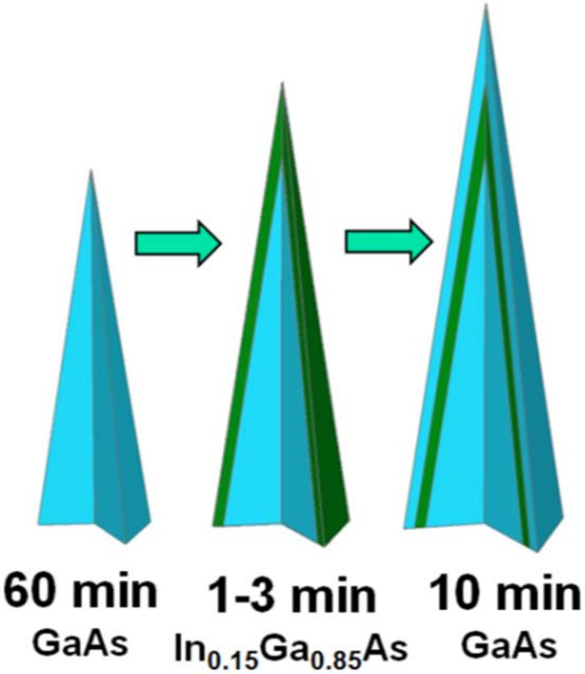

Figure 5.3 Three nanoneedle samples were grown, starting with a 4 µm long GaAs core for 60 min, then coating with $In_{0.15}Ga_{0.85}As$ for 1-3 min (~5 – 15 nm width), and capping with a GaAs barrier for 10 min. The schematic shows a three dimensional side-view of the nanoneedle growth steps with one third of the needle cut away to show the heterostructure layers.

5.3 Micro-photoluminescence of InGaAs Quantum Well Nanoneedles

Micro-photoluminescence measurements were performed on the single quantum well nanoneedles at temperatures of 4K. The results are shown in Figure 5.4(b), compared with a typical GaAs nanoneedle and the $In_{0.15}Ga_{0.85}As$ bulk nanoneedle. The 15 nm quantum well nanoneedle peak is at 1.339 eV, redshifted from the typical bulk wurtzite GaAs peak, due to carrier recombination in the lower-bandgap InGaAs region. The 15 nm well is blueshifted by 45 meV from the bulk $In_{0.15}Ga_{0.85}As$ nanoneedle emission, which may be due to strain resulting from lattice mismatch with the GaAs core. The exact contribution of strain is unknown though since the properties of bulk wurtzite InGaAs are yet to be determined, and the tapered nanoneedle sidewalls make it difficult to predict the strain relaxation in the heterostructure, and the strain contribution to bandgap shift. There is also a possibility that reduced indium incorporation in the well region compared to the InGaAs bulk nanoneedles contributes to this blueshift.

The 10 nm quantum well nanoneedle photoluminescence peak is at 1.351 eV, 12 meV higher. This quantum well nanoneedle emission is ~8x more intense than the typical GaAs nanoneedle, indicating that the carriers are confined to the well region, reducing the effects of non-radiative surface recombination. TEM images of these 10 nm $In_{0.15}Ga_{0.85}As$ layers grown on GaAs show that they are coherent to the GaAs core lattice.

The 5 nm quantum well nanoneedle has its peak at 1.458 eV, blueshifted further due to additional quantum confinement. In this case the carriers are less confined, and relatively more radiative recombination can be seen from the GaAs core at higher energy. The FWHM for the 5 nm quantum well is 34 meV.

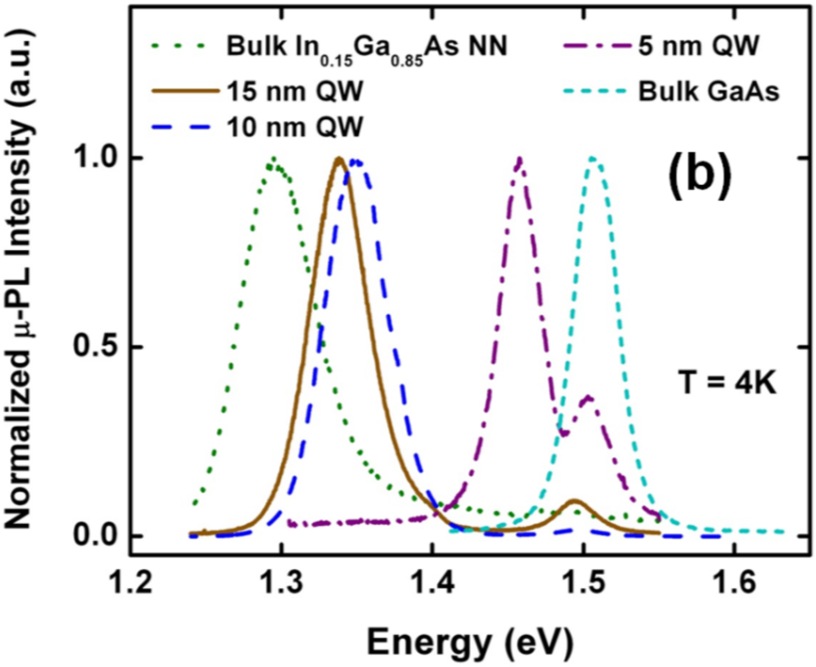

Figure 5.4 Micro-photoluminescence spectra of the 60-minute growth bulk GaAs nanoneedle, bulk $In_{0.15}Ga_{0.85}As$ nanoneedle and the three quantum well nanoneedles with thicknesses of 5, 10 and 15 nm.

The quantum well nanoneedles also exhibit photoluminescence at room temperature. Figure 5.5 shows the photoluminescence peak of the 10 nm quantum well from Figure 5.5 compared to a similar nanoneedle measured at room temperature. The emission is redshifted by 31 meV due to the temperature increase, and broadened due to the increased thermalization of carriers into the GaAs region.

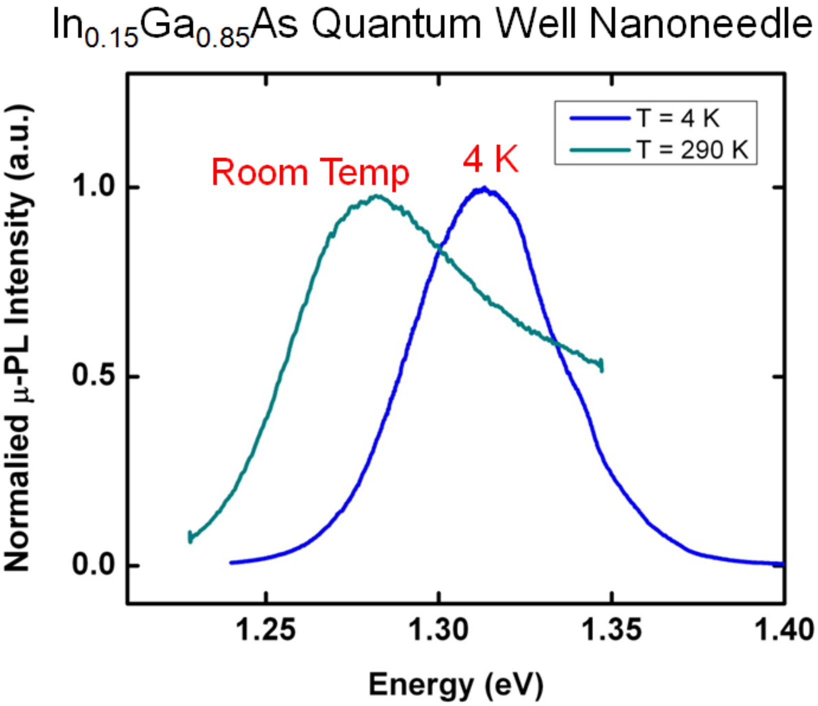

Figure 5.5 Micro-photoluminescence emission spectra of two different 15% indium nanoneedles, showing the difference between the 4 K and room temperature emission. The shift is 31 meV in this case.

5.4 Long-wavelength Quantum Well Nanoneedles

A third quantum well nanoneedle sample was grown with the same recipe as the 10 nm quantum well nanoneedle, except with the TMIn flow rate doubled. The resulting micro-photoluminescence spectrum is shown in Figure 5.6 along with the 15% indium quantum well nanoneedle and pure GaAs nanoneedle normalized spectra for comparison. The peak emission energy is at 1.119 eV, 390 meV below the GaAs peak. The indium composition is estimated to be 30% based on the photoluminescence emission. The emission peak energy shows the ability to tune the photoluminescence wavelength over a wide range, even below the absorption edge of silicon at 1.17 eV (at

T = 4 K). This is important for integrated optoelectronic devices on silicon which operate at wavelengths for which silicon waveguides are transparent.

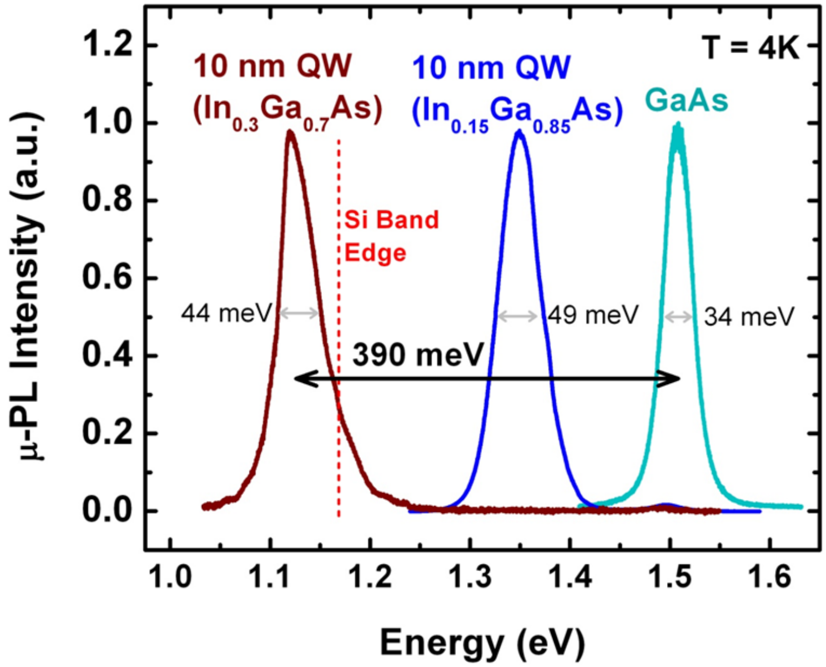

Figure 5.6 The micro-photoluminescence emission spectra of single nanoneedles comparing the 30% and 15% indium quantum well nanoneedles to the pure GaAs nanoneedle. All spectra are shown in normalized arbitrary units. The emission can be tuned from 1.509 eV to 1.119 eV, a range of 390 meV. The 30% indium quantum well nanoneedle emission is below the silicon band edge.

The 30% indium quantum well nanoneedle emission remains above the silicon band edge all the way up to room temperature. Figure 5.7 shows a plot of the photoluminescence from nanoneedles similar to those in Figure 5.6 plotted from 4 K to near room temperature.

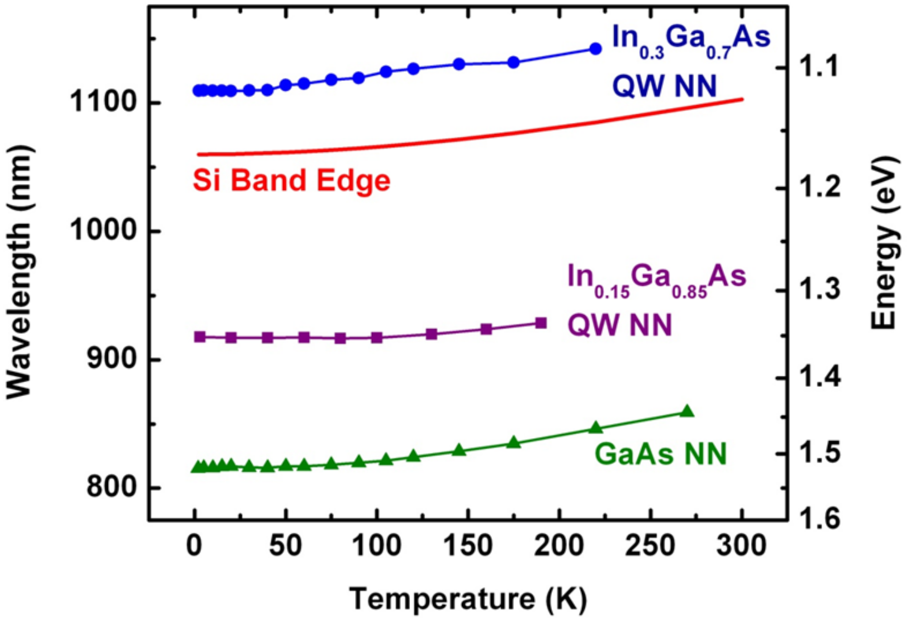

Figure 5.7 Micro-photoluminescence emission peak energies of single nanoneedles comparing the 30% and 15% indium quantum well nanoneedles to the pure GaAs nanoneedle plotted vs. temperature. The silicon band edge is shown for comparison. The nanoneedle with nominal 30% indium incorporation in the well shows emission at wavelengths longer than the silicon band edge throughout the temperature range.

6 Nanoneedle Transmission Electron Microscopy

6.1 Nanoneedle Selected Area Electron Diffraction

In order to determine the crystal phase of the nanoneedles, TEM was used in diffraction mode. Selected Area Electron Diffraction (SAED) can be used to determine the phase of the crystal, since the electrons diffract off of lattice planes in the crystal, much like in x-ray diffraction. Bragg's Law, shown in Eq. 3.6, relates the lattice plane spacing d to the diffraction angle θ based on the electron wavelength λ.

$$n\lambda = 2d \cdot \sin\theta \qquad 6.1$$

In TEM, the resulting SADP pattern contains electron diffraction peaks at distances r from the transmitted electron beam, which for a camera length L, relate to an interplanar spacing d according to Eq. 6.2.

$$rd = \lambda L \tag{6.2}$$

In this way, the SADPs can be used to determine the orientation and size of the crystal interplanar spacings, and thus the crystal structure. Figure 6.1 shows a diagram of this process. The blue line shows the incoming electron beam from the filament. When a crystal is oriented so a particular zone axis points along the optical axis of the TEM, then the resulting SADP will show peaks due to the zone axes which are close to perpendicular to the zone axis along the optical axis. Electrons will scatter at the different atom sites, and the diffraction conditions result in constructive interference at the points that satisfy Equation 6.2. For example in Figure 6.1, the diffracted peak at distance r from the transmtted beam satisfies the diffraction condition for the lattice planes marked by d. The distance r is equal to $\lambda L/d$. The direction the beam is diffracted away from the center transmitted beam corresponds to the normal vector of the lattice plane contributing to the diffraction peak.

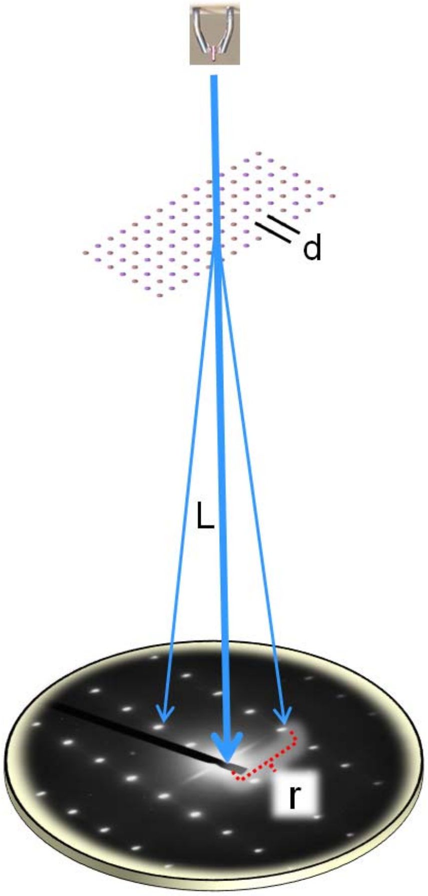

Figure 6.1 Diagram of electron diffraction.

Selected area electron diffraction patterns (SADPs) of nanoneedles were recorded in a TEM to determine the crystal structure and uniformity of the nanoneedles. The samples were prepared by wiping copper TEM grids with holey carbon films across the substrates of nanoneedles, breaking the nanoneedles off from the surface. The nanoneedles adhere to the thin electron-transparent carbon film, which supports the nanoneedles for imaging. The nanoneedles end up typically lying on one of their six flat sidewalls on the image plane of the TEM. Since the c-axis of the nanoneedles points towards the tip of the nanoneedles, this means tilting these nanoneedles up 3-4° will result in TEM imaging on the $\langle 1\bar{1}00\rangle$ family of zone axes, with the $\langle 0001\rangle$ c-axis lying horizontally in the image plane.

Figure 6.2 shows SADPs from a GaAs nanoneedle grown on sapphire grown for 60 min, which was rotated about its c-axis to three different zone axes. The patterns are all displayed at the same scale. The diagrams of the nanoneedles show the orientation of the lying-down nanoneedles in the image plane, with the c-axis pointing towards the top of the image plane.

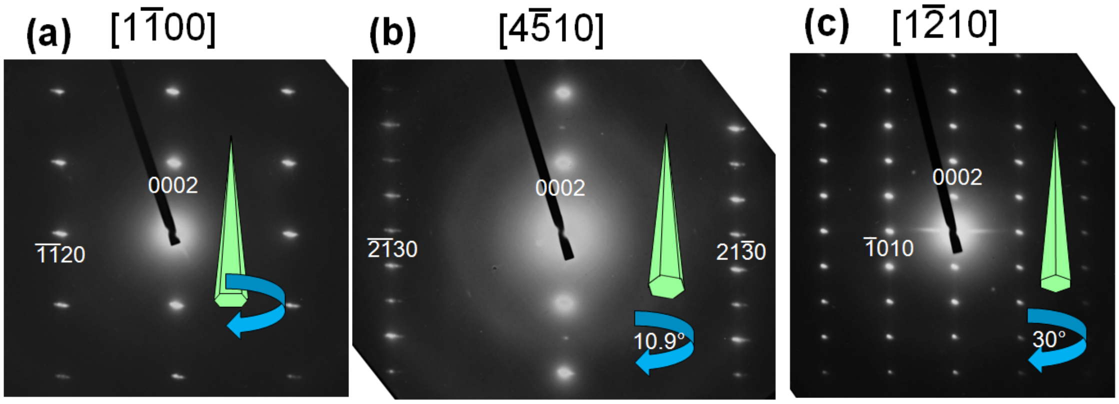

Figure 6.2 Selected area electron diffraction patterns from the same nanoneedle rotated to the $[\mathbf{1\bar{1}00}]$, $[\mathbf{4\bar{5}10}]$ and $[\mathbf{1\bar{2}10}]$ zone axes in (a), (b) and (c) respectively. The inset nanoneedle diagrams show a top-down view of the nanoneedle observed from the TEM optical axis. The blue arrow shows the direction of rotation of the nanoneedle about the c-axis. (c) The SADP shows unambiguously that the nanoneedle is wurtzite phase throughout the needle.

The SADP in Figure 6.2(a) is oriented on the $[1\bar{1}00]$ zone axis, close to the flat tapered sidewall of the nanoneedle. The $[0002]$ and $[\bar{1}\bar{1}20]$ peaks are labeled in this pattern. However, for wurtzite $\langle 1\bar{1}00\rangle$ and zincblende $\langle 2\bar{1}\bar{1}\rangle$, the resulting characteristic SADPs are identical to each other, given that in GaAs the $d_{0002}(\text{wurtzite})$ and $d_{111}(\text{zincblende})$ interplanar spacings are nearly equal to each other [38,55]. The nanoneedle must be rotated to other zone axes in order to observe SADPs that correspond unambiguously to wurtzite rather than zincblende and determine the full crystal structure.

Figure 6.2(b) shows the nanoneedle rotated to the $\left[4\bar{5}10\right]$ zone axis, 10.9° about the c-axis. In this zone axis, the SADP has a distinct orientation not observed in wurtzite.

Figure 6.2(c) shows the SADP of the nanoneedle rotated by 30° about the c-axis to the $[1\bar{2}10]$ zone axis on the corner of the nanoneedle sidewall. This SADP shows unambiguously that the crystal is pure hexagonal wurtzite phase throughout the needle. Moving the selected area aperture around the nanoneedle does not affect the SADP, showing that the nanoneedles are single-crystal. This diffraction pattern shows unique SADP peaks corresponding to wurtzite $[1\bar{1}00]$ interplanar spacings. This particular interplanar spacing does not appear for zincblende GaAs in any orientation. It is also clear that the material is not wurtzite, because rotation of zincblende at the $[2\overline{11}]$ zone axis by 30° about the $[111]$ axis (similar to the wurtzite c-axis) would be on the $[1\bar{1}0]$ zone axis, which has a very different SADP. The $[0001]$ peaks specific to the wurtzite phase also appear due to double-diffraction [56].

Figure 6.3 shows a comparison of kinematical simulations of SADPs from the wurtzite $\langle 1\bar{2}10\rangle$ and zincblende $\langle 1\bar{1}0\rangle$ families of zone axes at the same scale to highlight the differences in both the orientation of the diffraction peaks and their spacings. Figure 6.3(a) shows the diffraction peaks in blue (with the missing peaks seen via double-diffraction as open circles). The indices are labeled in the format h, k, l corresponding to $[h, k, -(h+k), l]$ wurtzite zone axes. The zincblende SADP in Figure 6.3(b) has a much different pattern, with a skewed hexagonal shape, and spacings much different than those seen in wurtzite.

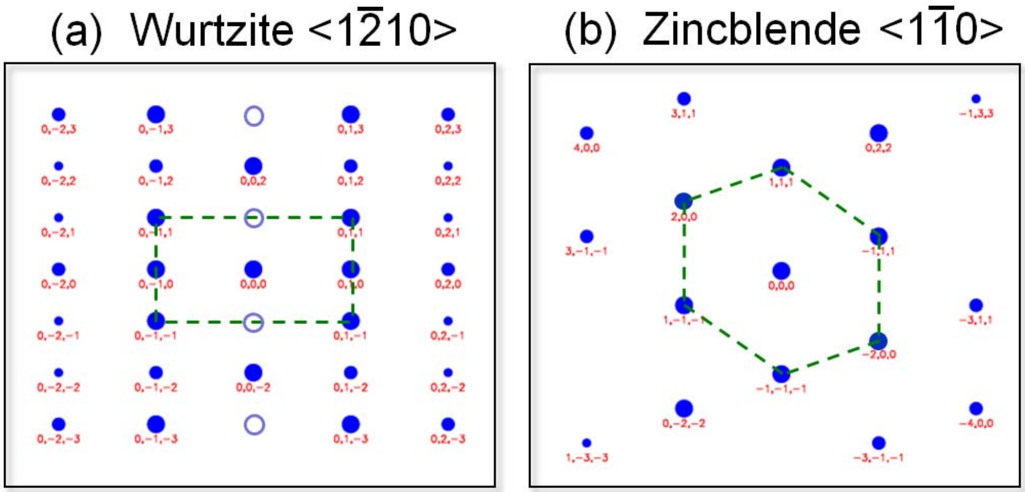

Figure 6.3 Comparison of kinematical simulations of SADPs from wurtzite and zincblende. ***Courtesy of J.M. Zuo and J.C. Mabon, Web-based Electron Microscopy Application Software: Web-EMAPS, Microsc Microanal 10(Suppl 2), 2004; URL: http://emaps.mrl.uiuc.edu/***

A second GaAs nanoneedle was imaged in TEM in Figure 6.4(a), which was broken off near the base where the nanoneedle was 450 nm wide, and ended up standing straight up on the carbon film along with its c-axis normal to the image plane. The arrows show the direction of the normal vectors for the $\{1\bar{1}00\}$ and $\{1\bar{2}10\}$ families of planes. A SADP was also recorded in the area denoted by the red circle, and is shown in Figure 6.4(b). Again, the SADP from this orientation shows that the structure is wurtzite, due to the presence of SADP peaks from the $\{1\bar{1}00\}$ planes, which are not seen in zincblende. The $\{1\bar{1}00\}$ and $\{1\bar{2}10\}$ plane peaks show up in the expected orientation relative to the hexagonal shape of the nanoneedle as well. The SADP chevron shape is due to scattering from the two nanoneedle side-facets included in the SADP area. The $\{1\bar{1}00\}$

interplanar spacings are the largest seen in this SADP pattern, and their corresponding 3.45 Å interplanar spacings uniquely match those of wurtzite GaAs, rather than the largest spacing of 2.00 Å expected from $\{2\bar{2}0\}$ planes in zincblende GaAs. Contrary to many reports on GaAs VLS nanowire growth [40,57,58] these nanoneedles have pure wurtzite phase material throughout the entire nanoneedle.

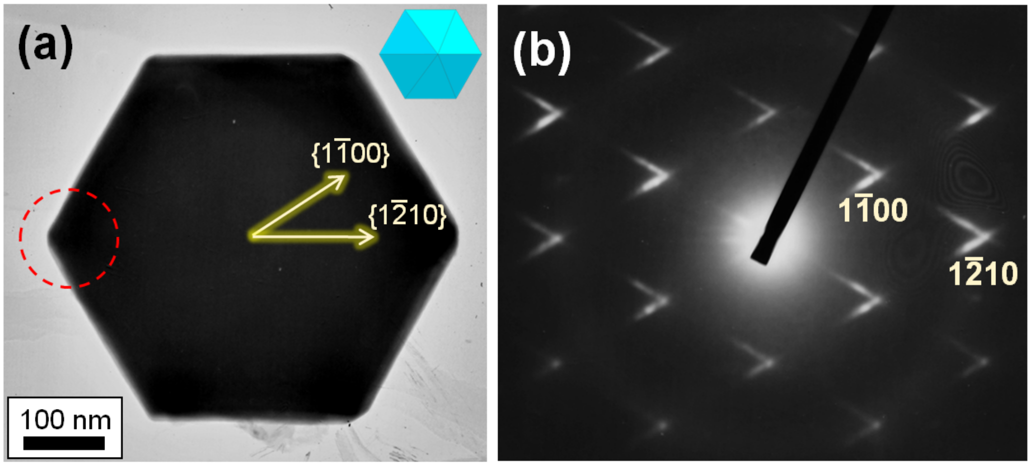

Figure 6.4 (a) TEM image of the top portion of a nanoneedle imaged on the c-axis. A 3D diagram of the nanoneedle orientation is shown on the upper right. The arrows indicate the normal vectors for the $\{1\bar{1}00\}$ and $\{1\bar{2}10\}$ families of planes. (b) The SADP from the area shown in the red circle. Peaks from both the $\{1\bar{1}00\}$ and $\{1\bar{2}10\}$ planes are seen, whereas in zincblende only peaks in the $\{1\bar{2}10\}$ positions would be visible.

6.2 High Resolution Nanoneedle TEM imaging

High-resolution TEM (HRTEM) is a TEM technique that utilizes phase contrast imaging of electron waves passing through a thin sample of crystal to achieve imaging resolutions as low as 1 Å. The electrons passing through a thin crystal undergo different phase shifts depending on the path they take through the periodic crystal structure, due to their charge interaction with the atomic potentials. These differences in phase, in combination with the other parameters of the microscope, sample thickness, and defocus, can result in amplitude contrast with high resolution. It is important to note that the location of light and dark portions of the image are dependent on many factors, such as defocus, sample thickness, and aberration of the microscope, and thus do not necessarily denote the exact position of particular atom columns. However, the contrast periodicity is usually a direct result of the crystal structure periodicity. Figure 6.5 shows a 4x4 grid of simulated TEM images, to serve as an example of how the appearance of the phase contrast image can change based on the thickness of the sample region or defocus. The actual positions of the atom columns generating the phase contrast images are shown on the upper-right at the same scale.

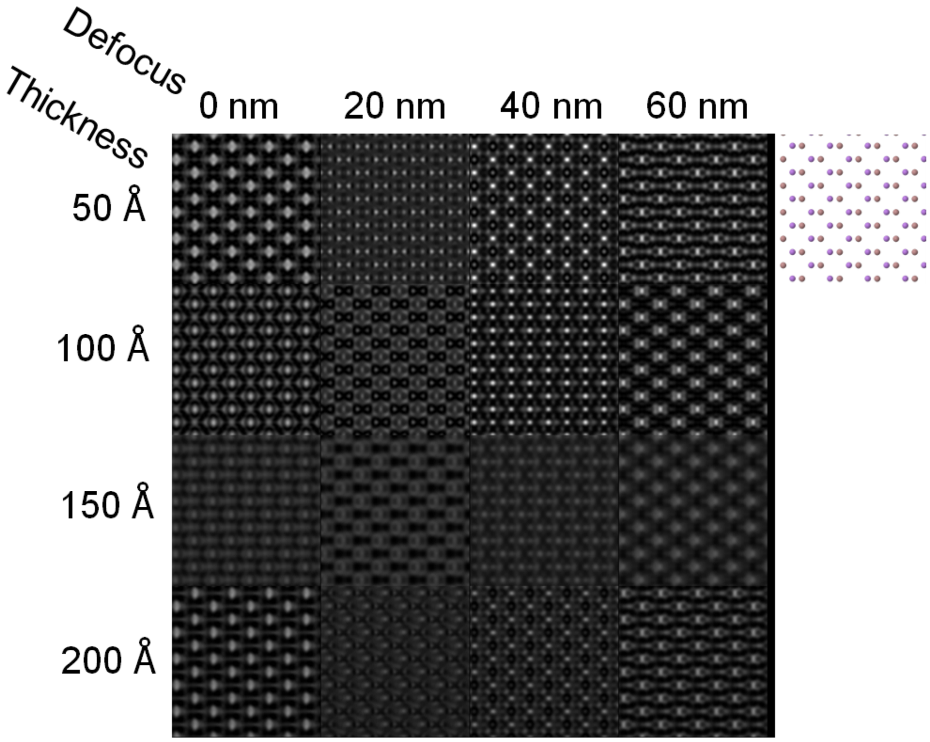

Figure 6.5 4x4 array of TEM image simulations of $[110]$GaAs with thickness varied in the vertical direction and defocus of the sample varied in the horizontal. The actual atom column arrangement is shown on the right. This demonstrates that the phase contrast pattern can appear different depending on the parameters used for the sample and imaging. ***Courtesy of J.M. Zuo and J.C. Mabon, Web-based Electron Microscopy Application Software: Web-EMAPS, Microsc Microanal 10(Suppl 2), 2004; URL: http://emaps.mrl.uiuc.edu/***

Figure 6.6(a) shows an HRTEM image on the $[1\bar{1}00]$ zone axis of a GaAs nanoneedle grown on GaAs, with a zoomed-out view in Figure 6.6(b). The tip in the image comes to an atomically sharp point just 2 – 4 nm wide. The material remains single-crystal wurtzite all the way up until the tip, with no catalyst material observed. There is a surrounding 2 nm oxide layer which forms due to exposure to air. The fast Fourier transform (FFT) in Figure 6.6(c) shows spatial frequency peaks which are similar to those seen in SADPs, and depend on the crystal lattice periodicity in much the same way. The position and orientation of the peaks can be used to determine the lattice constants of the material after calibration to known samples, in this case it was a silicon sample. The c and a-axes for this nanoneedle were determined to be 6.52 Å and 3.98 Å respectively, within ± 0.5%. HRTEM measurements from other nanoneedles are consistent with these values. This c/a ratio is 1.638, close to the ideal hexagonal ratio of 1.633, and in close agreement with recent x-ray diffraction of wurtzite GaAs in powder form created through high-pressure treatments [55].

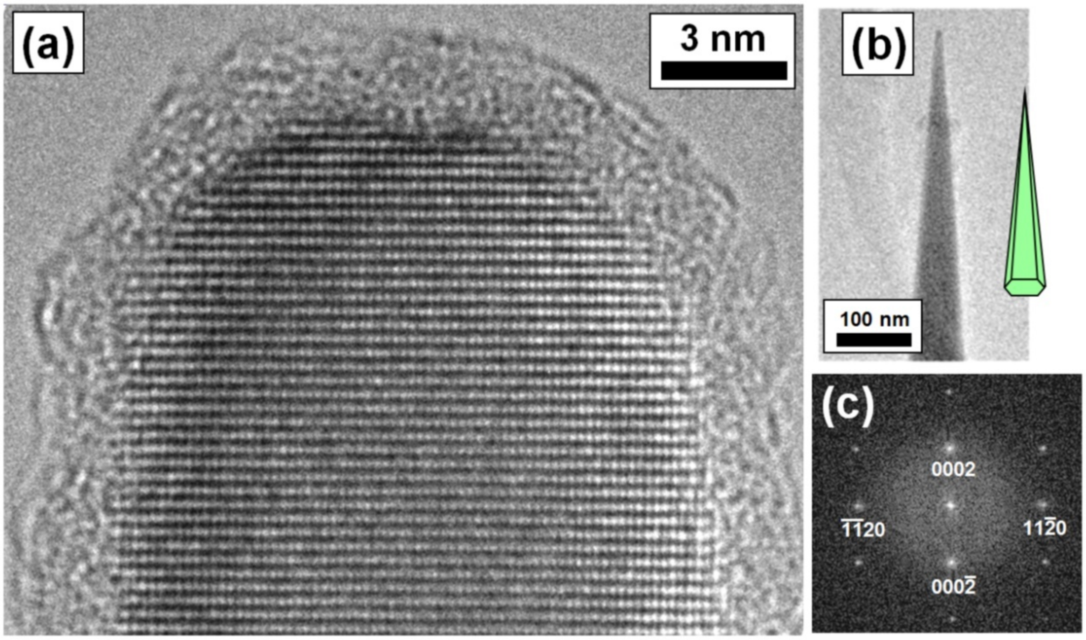

Figure 6.6 (a) HRTEM image of an ultra-sharp GaAs nanoneedle grown on GaAs substrate, viewed on the $[1\bar{1}00]$ zone axis. (b) Zoomed-out view of the nanoneedle tip, with a diagram showing the orientation of the nanoneedle in the image plane. (c) FFT of the HRTEM image.

Imaging along the sides of the nanoneedles away from the tip similarly shows a very uniform crystal structure. Figure 6.7 shows an HRTEM image looking at the edge of the nanoneedle at the 120° corner of the hexagonal cross section. Imaging at this corner means the sample gets much thicker to the right of the image, with the thickness t relating to distance d from the corner along the red arrow as $t = d\sqrt{3}/2$. This results in the banding effect seen. The phase contrast appears different based on the varying thickness, just as in Figure 6.5, so each band represents regions of similar thickness.

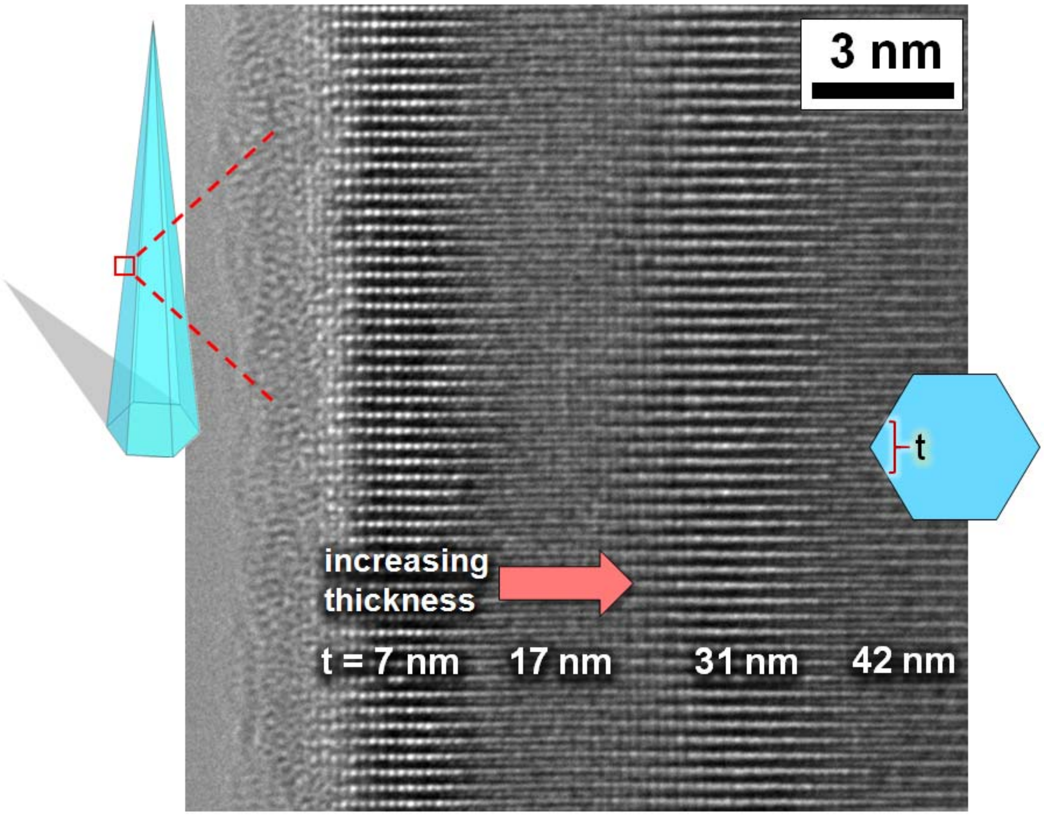

Figure 6.7 HRTEM image of a GaAs nanoneedle grown on GaAs substrate, viewed on the $[1\bar{1}00]$ zone axis at the side of a nanoneedle near the corner, as shown on the diagram on the left. The thickness of the sample increases towards the right of the image, due to the 120° corner of the nanoneedle. The phase contrast varies due to its thickness dependence, creating the appearance of bands.

6.3 Comparisons of Wurtzite and Zincblende Crystal Zone Axes

It is important to note that for HRTEM images at the $\langle 1\bar{1}00\rangle$ family of zone axes, the phase contrast lattice image for wurtzite GaAs is indistinguishable from the zincblende $\langle 2\overline{11}\rangle$ family of axes, just like in the case of SADP patterns. Figure 6.8 shows a comparison of the actual lattices of the wurtzite and zincblende phases of GaAs on the $\langle 1\bar{1}00\rangle$ and $\langle 2\overline{11}\rangle$ zone axes, respectively. These lattice images and subsequent images in this work were generated using *"Jmol: an open-source Java viewer for chemical structures in 3D. http://www.jmol.org/"* in combination with crystal files generated from

WebEMAPS (*Courtesy of J.M. Zuo and J.C. Mabon, Web-based Electron Microscopy Application Software: Web-EMAPS, Microsc Microanal 10(Suppl 2), 2004; URL: http://emaps.mrl.uiuc.edu/*).

The corresponding nanoneedle orientation for this zone axis is shown on the left. The differences between the two materials stack within each atom column are obscured at this orientation behind each column, so the lattice must be tilted to another zone axis to determine the crystal structure and get a complete picture of the arrangement of the atoms.

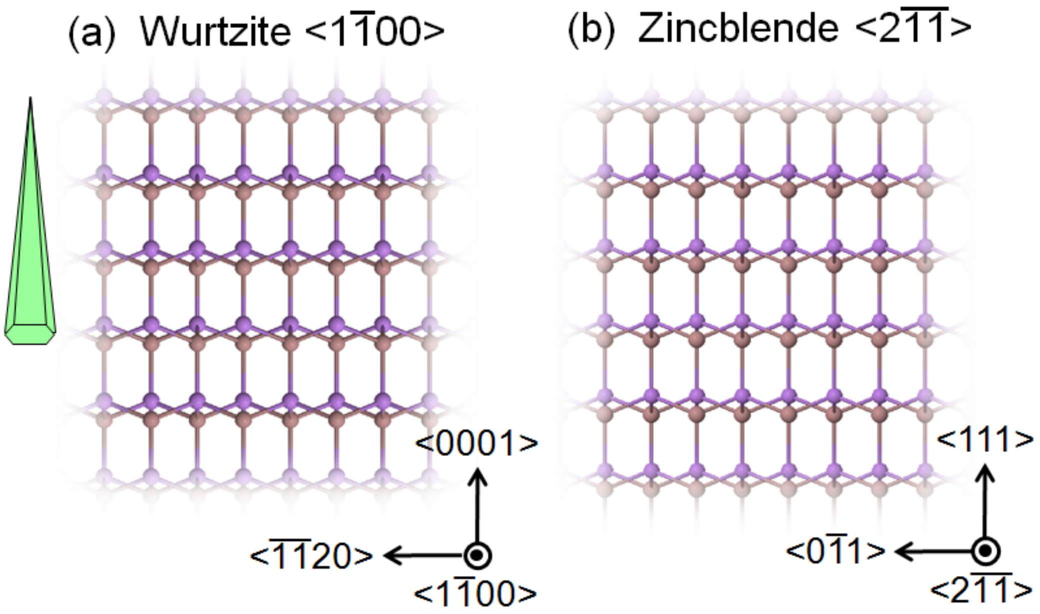

Figure 6.8 Crystal lattice of $\langle 1\bar{1}00\rangle$ wurtzite GaAs compared with that of $\langle 2\bar{1}\bar{1}\rangle$ zincblende GaAs. The atomic column arrangements appear identical for these zone axes.

Rotating from the $\langle 1\bar{1}00\rangle$ by 10.9° about the c-axis to the $\langle 4\bar{5}10\rangle$ zone axes results in the pattern seen in Figure 6.9. The characteristic difference of wurtzite and zincblende material becomes apparent. The wurtzite has a pattern which repeats itself every two layers in an ABAB pattern, with the atom pairs flipping direction every layer. The zincblende repeats itself every three layers.

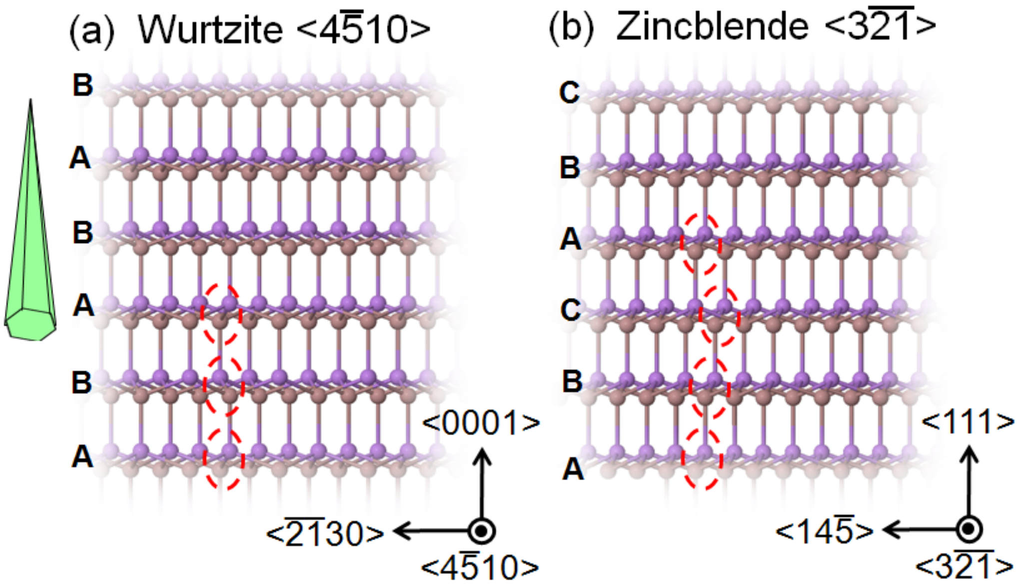

Figure 6.9 Crystal lattice of $\langle 4\bar{5}10\rangle$ wurtzite GaAs compared with that of $\langle 3\overline{21}\rangle$ zincblende GaAs. The atomic column arrangements start to show the difference in the wurtzite ABAB stacking compared with the zincblende ABCABC stacking.

Upon further rotation from the $\langle 1\bar{1}00\rangle$ zone axis by 30°, the difference between the wurtzite and zincblende phases become more apparent. This zone axis is shown in Figure 6.10. Again, the wurtzite phase repeats itself every two layers, whereas the zincblende phase repeats every three layers. This significantly alters both the HRTEM images and diffraction patterns seen at this zone axis, just like in Figure 6.2.

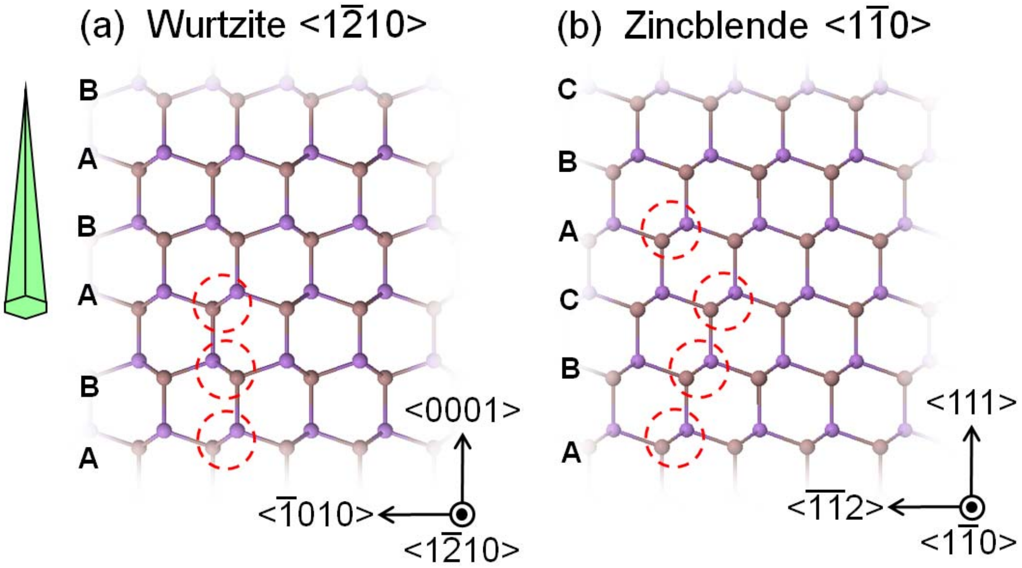

Figure 6.10 Crystal lattice of $\langle 1\bar{2}10\rangle$ wurtzite GaAs compared with that of $\langle 1\bar{1}0\rangle$ zincblende GaAs. This orientation clearly shows the differences in the wurtzite ABAB stacking compared with the zincblende ABCABC stacking.

The following HRTEM images show nanoneedles at the other zone axes described, so that the wurtzite structure can be observed directly. Figure 6.11(a) shows an HRTEM image of another GaAs nanoneedle grown on GaAs, on the $[1\bar{2}10]$ zone axis, with a zoomed-out view in Figure 6.11(b). Here, the oxide layer is obscured because the nanoneedle tip was lying on carbon film. The tip of this nanoneedle comes to an extremely sharp point of only a few lattice spacings wide, < 1 nm. The fast Fourier transform (FFT) in Figure 6.11(c) shows the unique wurtzite pattern with peaks from $\{1\bar{1}00\}$ family planes. For this orientation, the differences between wurtzite and zincblende structure can be directly observed in the image rather than inferred from SADPs.

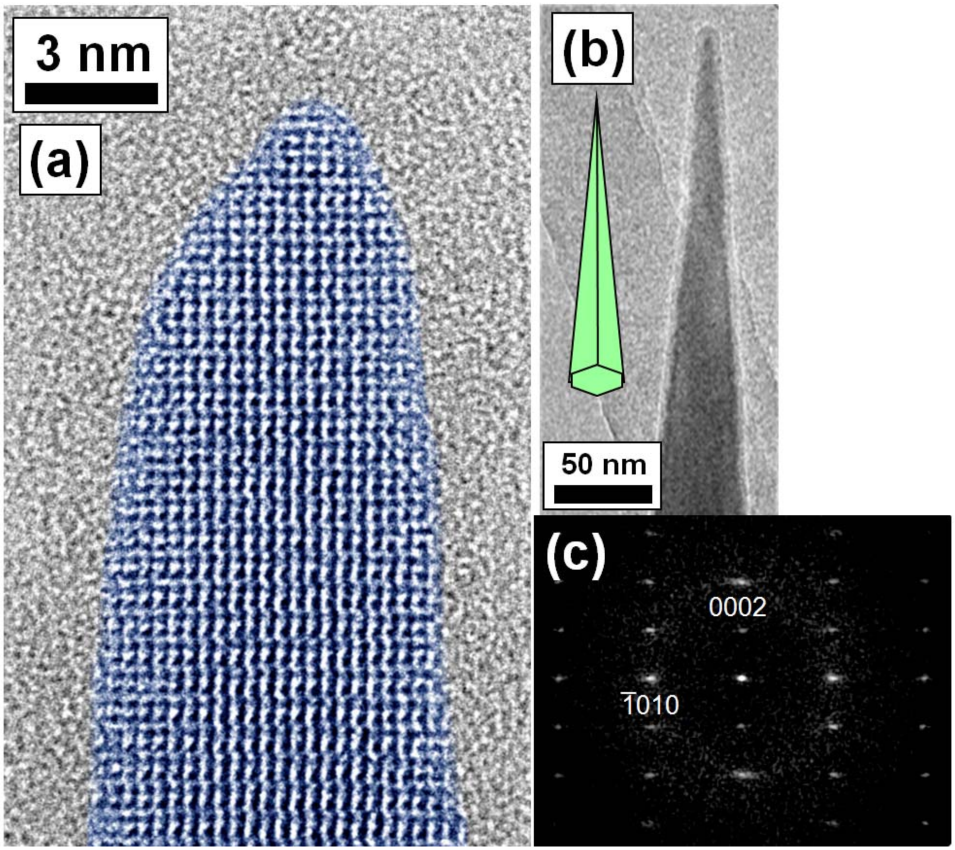

Figure 6.11 (a) HRTEM image of an ultra-sharp nanoneedle viewed on the $[1\bar{2}10]$ zone axis. (b) Zoomed-out view of the nanoneedle tip, with a diagram showing the orientation of the nanoneedle in the image plane. (c) FFT of the HRTEM image, showing periodicity unique to wurtzite.

Figure 6.12 shows the wurtzite atomic column pattern superimposed over the nanoneedle image from Figure 6.11, to make the ABAB periodicity of the image more clear. It can be seen that as well as being stacking-defect-free material, the tip comes to a very sharp point.

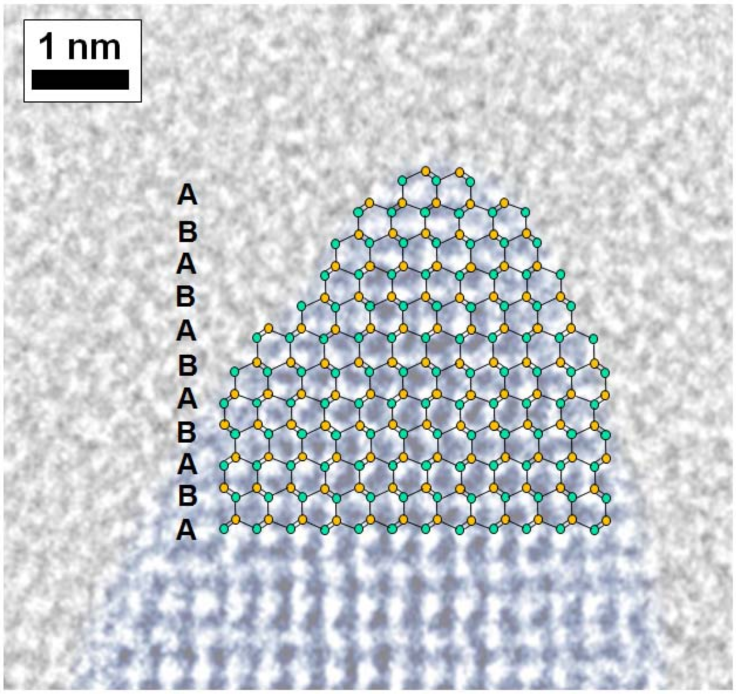

Figure 6.12 (a) HRTEM image of the tip of the same nanoneedle in Figure 6.11. The atomic lattice for wurtzite $[1\bar{2}10]$ is overlaid to highlight the periodicity of the structure, as well as the extremely small size of the tip.

Figure 6.13(a) shows the edge of a nanoneedle broken off of the substrate, viewed top-down along the c-axis. The diagram at the upper right shows the orientation of the nanoneedle in the image. A diagram of the actual positions of the atomic columns is shown superimposed on the right. Figure 6.13(b) shows the FFT of the image. Similar to Figure 6.4, the peaks have a large spatial period of around 3.45 Å perpendicular to the c-axis, rather than the 2.00 Å period in zincblende.

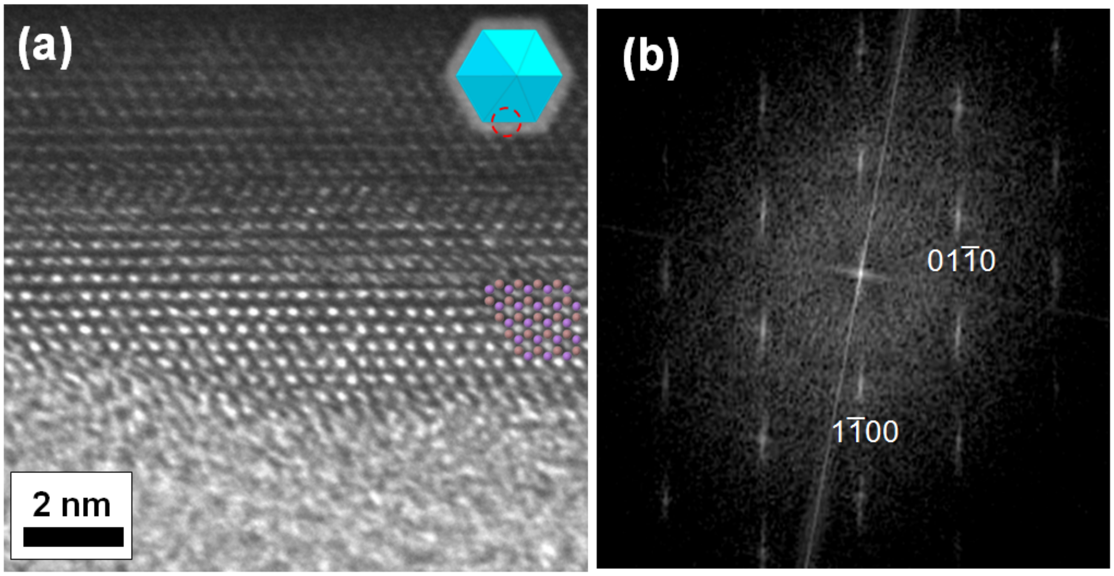

Figure 6.13 TEM image at the edge of a nanoneedle viewed on the $[0001]$ zone axis. The actual positions of the atom columns are overlaid on the right. The FFT is shown which indicates the pure wurtzite phase.

Figure 6.14 shows the lattice of wurtzite GaAs on the $\langle 0001\rangle$ zone axis, just like in Figure 6.13, compared with zincblende on the $\langle 111\rangle$ zone axis. The zincblende pattern has a similar hexagonal shape, but with additional atom columns in the center of the open hexagonal areas seen in the wurtzite pattern. This means that the larger spatial period peaks seen in the FFT for Figure 6.13 would not occur for zincblende material. In the case of Figure 6.13, the white spots represent the areas in the center of the open hexagons, and the darker areas in between are where the atom columns actually lie, similar to the effect shown in Figure 6.5.

It is important to note that the actual density of the atoms on the surface layer for the two materials is the same for both the crystal phases. The zincblende appears denser because there are three different monolayers which interleave, repeating in the ABCABC… pattern, whereas the wurtzite alternates only twice (ABAB…). This similarity of the growth surfaces is part of the reason why twinning is prone to occur in nanowires grown in the $\{111\}$ zincblende or $\{0001\}$ wurtzite planes, as the surface of each monolayer of growth is roughly the same for both materials from an epitaxial perspective.

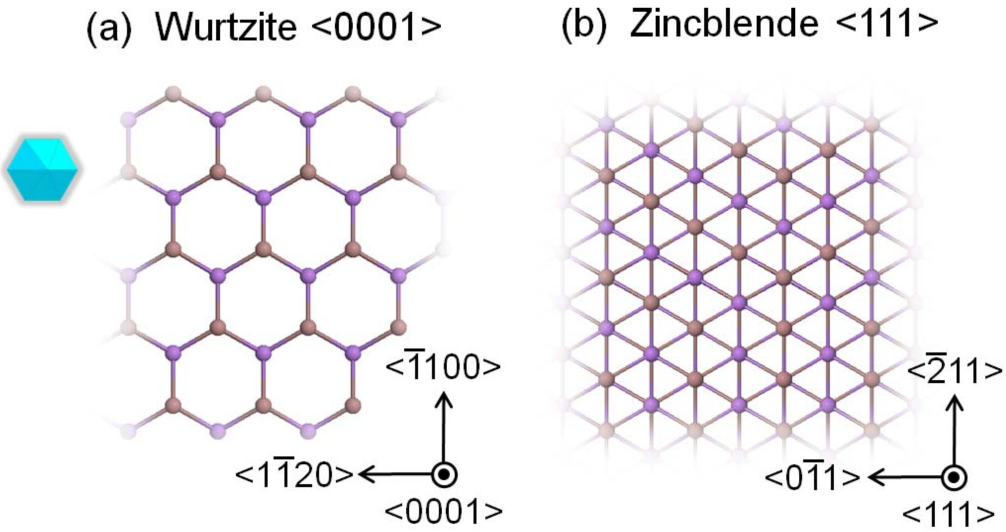

Figure 6.14 GaAs on the wurtzite $\langle 0001 \rangle$ family zone axis compared with zincblende $\langle 111 \rangle$.

6.4 GaAs Nanoneedles on Silicon TEM imaging

GaAs nanoneedles grown on silicon also show the same properties. Figure 6.15(a) shows a TEM image on the $[1\bar{2}10]$ axis of a GaAs nanoneedle which was grown on a (111)Si substrate. The FFT is shown in Figure 6.15(b), which shows the wurtzite pattern clearly, free of any zincblende phases. Figure 6.15(c) shows a zoomed-in view of the lattice image, with the atomic columns overlaid. The periodicity of the phase-contrast image matches with the periodicity of the atom columns expected for the $[1\bar{2}10]$ wurtzite zone axis generated from WebEMAPS.

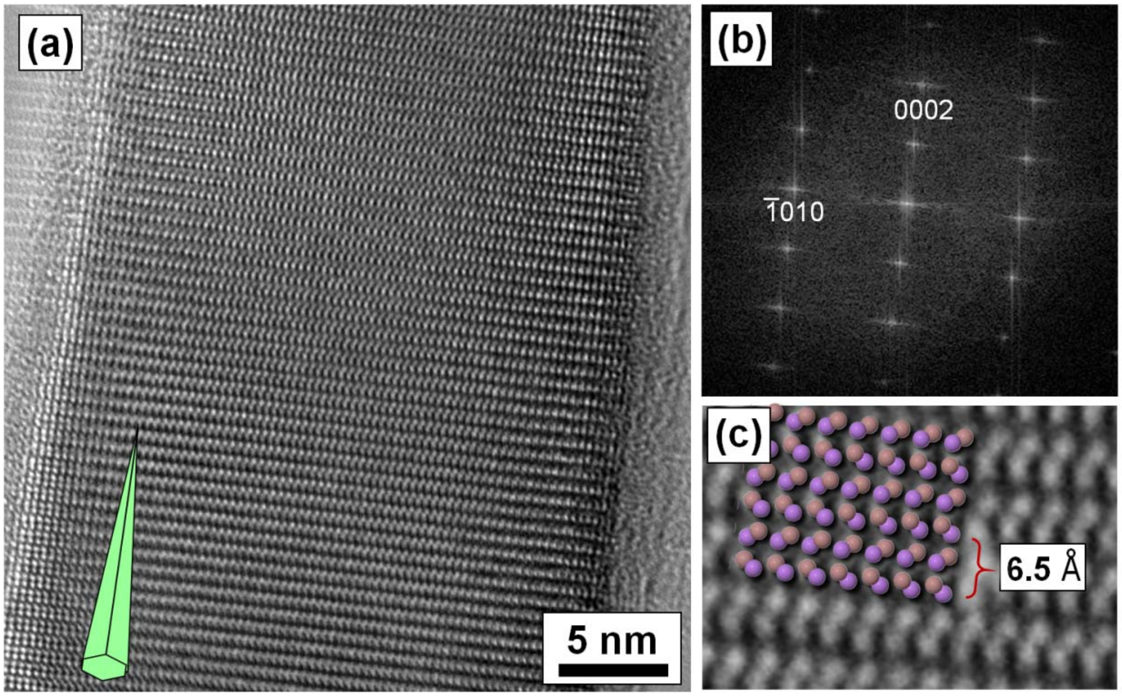

Figure 6.15 GaAs nanoneedle grown on silicon substrate on the $[1\bar{2}10]$ zone axis. (a) TEM image. (b) FFT showing the distinct wurtzite pattern. (c) Atomic column diagram overlaid on the TEM image, similar to Figure 6.10.

The GaAs nanoneedles grown on silicon also exhibit the same extremely sharp tips as on GaAs. The nanoneedle tip in Figure 6.16 shows the tip of a GaAs nanoneedle grown on a silicon substrate. The tip tapers down to a region less than a few nm wide. The nanoneedle imaged here is slightly blurry because of vibration perpendicular to the c-axis, due to the nanoneedle extending far off the edge of the carbon film in the TEM grid. The actual SADP from this nanoneedle tip however showed a clear diffraction pattern.

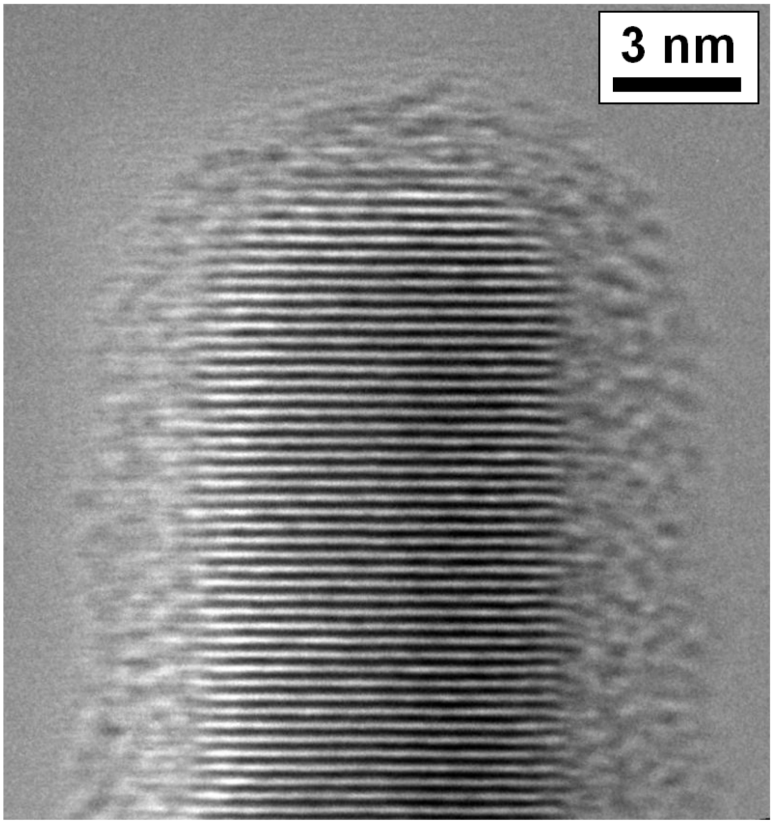

Figure 6.16 Tip of GaAs nanoneedle grown on silicon substrate imaged on the $[1\bar{1}00]$ zone axis. Similar to the nanoneedles grown on GaAs substrate, this tip comes to a point less than 1 nm wide.

GaAs nanoneedles grown on sapphire similarly result in the same sharp needle tips. Figure 6.17 shows a GaAs nanoneedle grown on sapphire, again with the lattice tapering down to about 1 nm. The cases for nanoneedle growth on silicon and sapphire substrate show that the physical properties of the nanoneedles are very similar, regardless of which substrate is used for the growth.

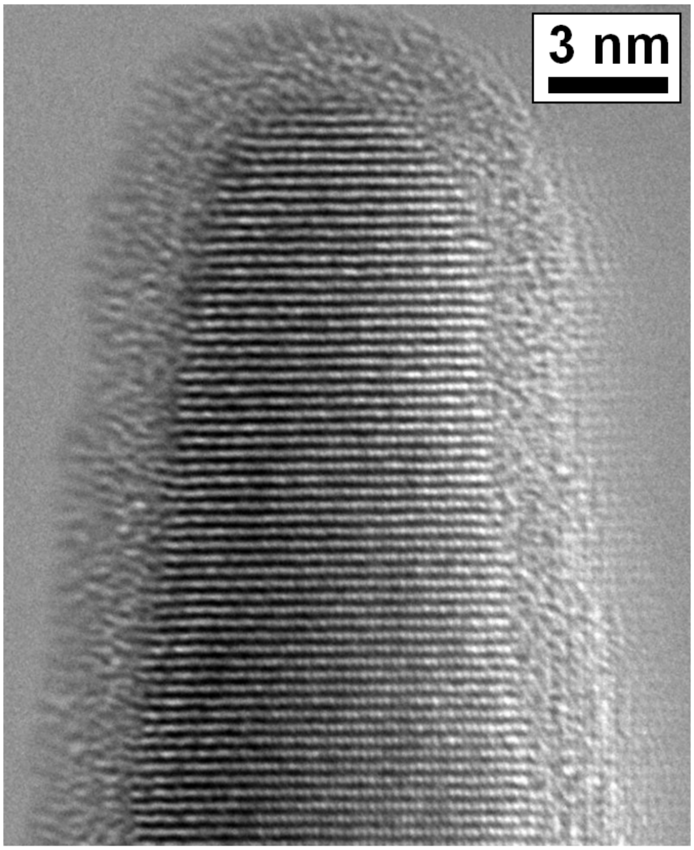

Figure 6.17 Tip of GaAs nanoneedle grown on sapphire substrate, imaged on the $[1\bar{1}00]$ zone axis.

6.5 InGaAs Nanoneedle TEM imaging

In addition to the pure GaAs nanoneedles, HRTEM was performed on the InGaAs nanoneedles. Figure 6.18 shows the tip of one of the nominal $In_{0.15}Ga_{0.85}As$ nanoneedles from Figure 5.1(c) imaged on the $[1\bar{1}00]$ zone axis. This image shows that the InGaAs nanoneedles also have extremely sharp tips similar to the pure GaAs nanoneedles, which taper down to less than a few nm. The nanoneedles also show the same twin-defect-free wurtzite pattern when rotated about the c-axis. The lattice constants for the c-axes and a-axes of the $In_{0.15}Ga_{0.85}As$ nanoneedles measured at the tips and sidewalls are larger than the GaAs nanoneedles by 0.9 ± 0.1%. The c-axis is measured as 6.58 Å.

For the GaAs nanoneedle TEM measurements, the wurtzite and zincblende d_{0002} and d_{111} interplanar spacings, respectively, are equal [38]. If one assumes this relation is similar for InAs, which in the zincblende phase has 7.16% larger lattice spacings than GaAs, then the 0.9% lattice mismatch of the wurtzite GaAs and InGaAs corresponds to 13% indium incorporation, close to the estimate of 15% based on photoluminescence experiments on the nanoneedles.

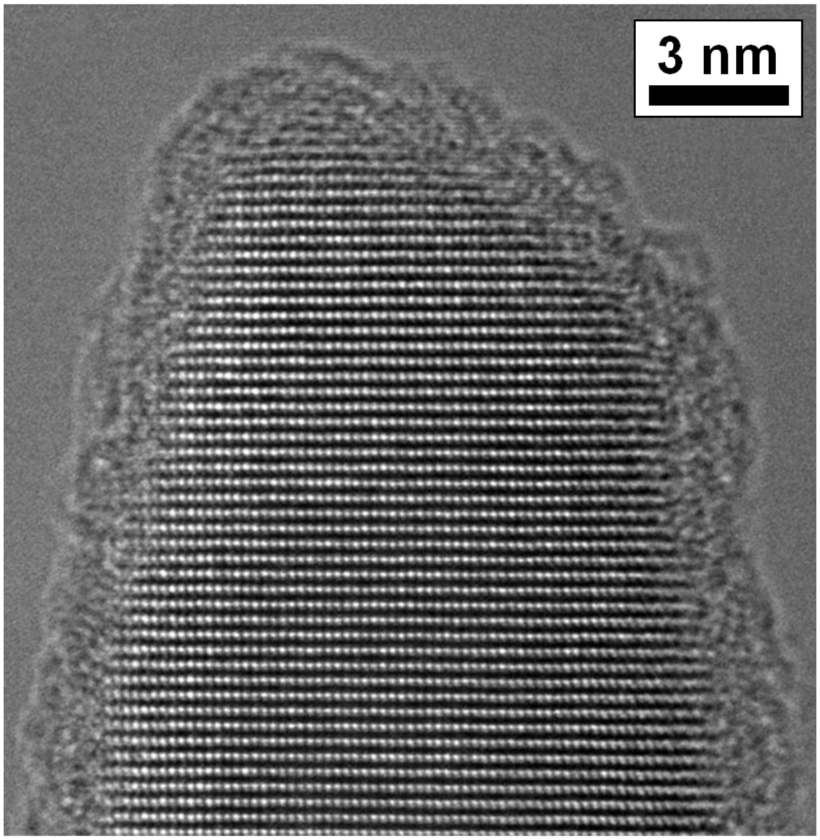

Figure 6.18 HRTEM image at the tip of the $In_{0.15}Ga_{0.85}As$ nanoneedle imaged on the $[1\bar{1}00]$ zone axis. Comparisons with the GaAs nanoneedles show that the lattice constant is 0.9 ± 0.1% larger.

This InGaAs nanoneedle was grown on sapphire, which shows that the nanoneedles grown on sapphire also exhibit the same sharp tips as those on GaAs and silicon. In this case, the taper angle is slightly larger at the tip due to the overall slightly larger taper angle caused by higher indium incorporation, which can be seen in the SEM images in previous sections.

6.6 InGaAs Nanoneedle Heterostructure TEM imaging

The quality of the interface between semiconductor heterostructures is important for quantum wells, because defect sites in the crystal can act as nonradiative recombination centers which are detrimental for devices which rely on radiative recombination [59].

To image the heterostructure interface quality in the InGaAs/GaAs heterostructure nanoneedles, a nanoneedle sample was grown with a GaAs core for 60 min, resulting in a ~4 µm long nanoneedle with a 300 nm diameter base. Then an $In_{0.15}Ga_{0.85}As$ layer was grown for 2 min, resulting in an approximately 10 nm InGaAs outer layer. This structure is similar to the previously discussed 10 nm InGaAs core-shell quantum well nanoneedles, but with the outer GaAs cap omitted to facilitate HRTEM imaging. Figure 6.19(a) shows the HRTEM image of this nanoneedle. Figure 6.19(b) shows the FFT of the HRTEM image. Figure 6.19(c) is a diagram showing a schematic of the nanoneedle core-shell structure, and the location and orientation of the TEM imaging axis. The nanoneedle was imaged on its side at the $[1\bar{2}10]$ zone axis so that the outer 10 nm region would contain only the InGaAs region and the rest of the image would be mostly pure GaAs as in Figure 6.19(c). The outer InGaAs section is coherent single-crystal material everywhere on the edge of the nanoneedle. The outer 2 – 3 nm native oxide is formed due to exposure to air, which is typical in the GaAs and InGaAs nanoneedles. The

FFT of the lattice region in Figure 6.19(b) shows a pure wurtzite phase pattern with no zincblende twinning, which is similar everywhere along the edge of the nanoneedle.

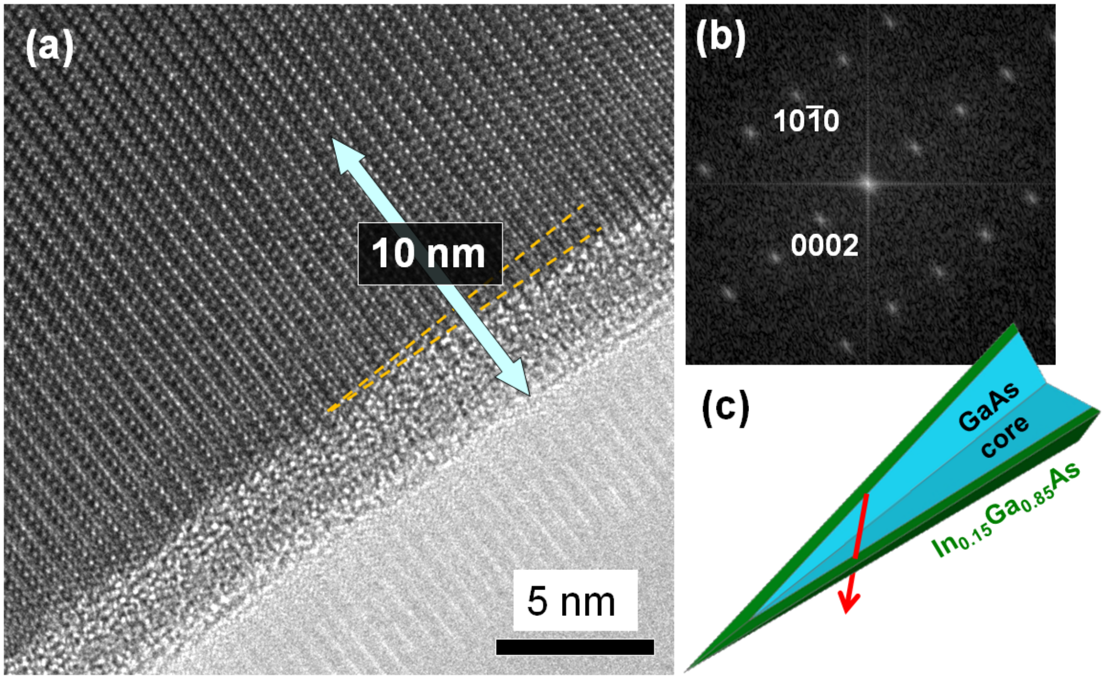

Figure 6.19 (a) HRTEM image of the outer edge of an InGaAs shell on GaAs core nanoneedle, imaged on the $[1\bar{2}10]$ plane. The light blue arrow shows the region of the image which consists of only $In_{0.15}Ga_{0.85}As$ due to the zone axes orientation. The InGaAs layer is coherent to the GaAs core. The yellow dotted lines also highlight the 3-4° taper of the nanoneedle sidewall. (b) shows the fast Fourier transform of the lattice area in (a) showing the unique wurtzite pattern. The TEM imaging axis and location is shown by the red arrow in (c). The nanoneedle is shown with 1/3rd cut away to show the heterostructure core.

No misfit dislocations are seen anywhere on the edge of the nanoneedle. The critical thickness for dislocations for $In_{0.15}Ga_{0.85}As$ grown on (100)GaAs substrates is typically over 20 nm for zincblende structures [14,60]. However the strain and mechanisms of strain relaxation for the 3D nanoneedle structures are more complicated than that of 2D thin films and are on a different crystal plane, so it is not certain how much strain these quantum well nanoneedle regions would be expected to accommodate. But at least for the 10 nm region, the growth appears to be coherent, which allows for the bright photoluminescence reported from these quantum well nanoneedles.

It is interesting to note that the nanoneedle sidewalls do not lie exactly on a low-index plane, in contrast with other hexagonal pyramidal growth such as in GaN [61]. Instead, due to the sharp 3-4° half-angle of the nanoneedle sidewalls, the TEM image reveals a terraced structure, as highlighted by the yellow dotted lines in Figure 6.19(a).

The TEM results discussed in this section show that the nanoneedle growth mode in MOCVD results in high uniformity crystals, which are single-crystal wurtzite phase, regardless of whether the growth is on GaAs, silicon or sapphire substrates, or whether the material has indium incorporation (up to 15% indium characterized in TEM). Heterostructure growth for the quantum wells appears coherent to the GaAs core in all the images recorded. The nanoneedles have extremely sharp tips as well in all the cases.

7 Conclusion

Understanding the growth properties of nanostructures is the first step in achieving the control of growth parameters necessary for uniform, repeatable devices. Also, exploring new growth modes for III-V nanostructures can open the path for other potential devices.

In this work we have demonstrated the prediction of III-V nanowire growth rate and crystal phase based on the theoretical modeling of the nanowires and identification of certain critical diameters which govern the nanowire growth. In particular, controlling the crystal phase of nanowires is important for achieving devices with predictable optical and electronic properties.

We have also demonstrated that nanoneedles can open the path to many devices due to their unique growth properties. Particularly, their very low growth temperature, and catalyst-free properties make them ideal for silicon CMOS processes, which are sensitive to damage from temperatures above 450 °C and also to Au contamination.

The nanoneedle structures are also of interest due to their ultra-sharp tips, which could open a path for nonlinear optical devices, or other applications dependent on electric field enhancement at sharp tips, such as tip-enhanced Raman spectroscopy, or even self-assembled growth of parallel atomic force microscope tips. The AlGaAs heterostructures could potentially be used for attoliter droplet delivery devices integrated with microfluidic structures.

Overall, this work has shown the potential for new methods of integrating lattice-mismatched semiconductors, particularly III-V materials with silicon, which overcome the previous limitations of typical thin-film growth on silicon.

8 Bibliography

[1] H. Takeuchi, A. Wung, Xin Sun, R. Howe, and Tsu-Jae King, “Thermal budget limits of quarter-micrometer foundry CMOS for post-processing MEMS devices,” *Electron Devices, IEEE Transactions on*, vol. 52, 2005, pp. 2081-2086.

[2] Y. Ohno, R. Terauchi, T. Adachi, F. Matsukura, and H. Ohno, “Spin Relaxation in GaAs(110) Quantum Wells,” *Physical Review Letters*, vol. 83, Nov. 1999, p. 4196.

[3] A.A. Kiselev and K.W. Kim, “Progressive suppression of spin relaxation in 2D channels of finite width,” *cond-mat/9910482*, Oct. 1999.

[4] J.A. Gupta, D.D. Awschalom, X. Peng, and A.P. Alivisatos, “Spin coherence in semiconductor quantum dots,” *Physical Review B*, vol. 59, Apr. 1999, p. R10421.

[5] M. Yoshita, H. Akiyama, L.N. Pfeiffer, and K.W. West, “Quantum wells with atomically smooth interfaces,” *Applied Physics Letters*, vol. 81, Jul. 2002, pp. 49-51.

[6] Y. Kajikawa, “Level anticrossing and related giant optical anisotropy caused by the Stark effect in a strained (110) quantum well,” *Physical Review B*, vol. 49, Mar. 1994, p. 8136.

[7] C. Chang-Hasnain, Pei-cheng Ku, Jungho Kim, and Shun-lien Chuang, “Variable optical buffer using slow light in semiconductor nanostructures,” *Proceedings of the IEEE*, vol. 91, 2003, pp. 1884-1897.

[8] P. Ku, F. Sedgwick, C.J. Chang-Hasnain, P. Palinginis, T. Li, H. Wang, S. Chang, and S. Chuang, “Slow light in semiconductor quantum wells,” *Optics Letters*, vol. 29, Oct. 2004, pp. 2291-2293.

[9] P. Palinginis, S. Crankshaw, F. Sedgwick, E. Kim, M. Moewe, C.J. Chang-Hasnain, H. Wang, and S. Chuang, “Ultraslow light (< 200 m/s) propagation in a semiconductor nanostructure,” *Applied Physics Letters*, vol. 87, Oct. 2005, pp. 171102-3.

[10] P. Palinginis, F. Sedgwick, S. Crankshaw, M. Moewe, and C. Chang-Hasnain, “Room temperature slow light in a quantum-well waveguide via coherent population oscillation,” *Optics Express*, vol. 13, Nov. 2005, pp. 9909-9915.

[11] M. Sargent, “Spectroscopic techniques based on Lamb's laser theory,” *Physics Reports*, vol. 43, Jul. 1978, pp. 223-265.

[12] M.S. Bigelow, N.N. Lepeshkin, and R.W. Boyd, “Ultra-slow and superluminal light propagation in solids at room temperature,” *Journal of Physics: Condensed Matter*, vol. 16, Nov. 2004, p. R1321.

[13] H. Wang, J. Remillard, M. Webb, D. Steel, J. Pamulapati, J. Oh, and P. Bhattacharya, “High resolution laser spectroscopy of relaxation and the excitation lineshape of excitons in GaAs quantum well structures,” *Surface Science*, vol. 228, Apr. 1990, pp. 69-73.

[14] P.L. Gourley, I.J. Fritz, and L.R. Dawson, “Controversy of critical layer thickness for InGaAs/GaAs strained-layer epitaxy,” *Applied Physics Letters*, vol. 52, Feb. 1988, pp. 377-379.

[15] J. Zou, D.J.H. Cockayne, and B.F. Usher, “Misfit dislocations and critical thickness in InGaAs/GaAs heterostructure systems,” *Journal of Applied Physics*, vol. 73, Jan. 1993, pp. 619-626.

[16] L.C. Chuang, M. Moewe, C. Chase, N.P. Kobayashi, C. Chang-Hasnain, and S. Crankshaw, “Critical diameter for III-V nanowires grown on lattice-mismatched substrates,” *Applied Physics Letters*, vol. 90, Jan. 2007, pp. 043115-3.

[17] R.S. Wagner and W.C. Ellis, “VAPOR-LIQUID-SOLID MECHANISM OF SINGLE CRYSTAL GROWTH,” *Applied Physics Letters*, vol. 4, Mar. 1964, pp. 89-90.

[18] F. Glas, “Critical dimensions for the plastic relaxation of strained axial heterostructures in free-standing nanowires,” *Physical Review B (Condensed Matter and Materials Physics)*, vol. 74, 2006, pp. 121302-4.

[19] L.C. Chuang, M. Moewe, S. Crankshaw, and C. Chang-Hasnain, “Optical properties of InP nanowires on Si substrates with varied synthesis parameters,” *Applied Physics Letters*, vol. 92, Jan. 2008, pp. 013121-3.

[20] E. Ertekin, P.A. Greaney, D.C. Chrzan, and T.D. Sands, “Equilibrium limits of coherency in strained nanowire heterostructures,” *Journal of Applied Physics*, vol. 97, Jun. 2005, pp. 114325-10.

[21] J.C. Harmand, G. Patriarche, N. Pere-Laperne, M. Merat-Combes, L. Travers, and F. Glas, “Analysis of vapor-liquid-solid mechanism in Au-assisted GaAs nanowire growth,” *Applied Physics Letters*, vol. 87, Nov. 2005, pp. 203101-3.

[22] A.I. Persson, M.W. Larsson, S. Stenstrom, B.J. Ohlsson, L. Samuelson, and L.R. Wallenberg, “Solid-phase diffusion mechanism for GaAs nanowire growth,” *Nat Mater*, vol. 3, Oct. 2004, pp. 677-681.

[23] B. Pal, K. Goto, M. Ikezawa, Y. Masumoto, P. Mohan, J. Motohisa, and T. Fukui, “Type-II behavior in wurtzite InP/InAs/InP core-multishell nanowires,” *Applied Physics Letters*, vol. 93, 2008, pp. 073105-3.

[24] P. Mohan, J. Motohisa, and T. Fukui, “Controlled growth of highly uniform, axial/radial direction-defined, individually addressable InP nanowire arrays,” *Nanotechnology*, vol. 16, 2005, pp. 2903-2907.

[25] V.G. Dubrovskii and N.V. Sibirev, “Growth rate of a crystal facet of arbitrary size and growth kinetics of vertical nanowires,” *Physical Review E*, vol. 70, 2004, p. 031604.

[26] W. Seifert, M. Borgström, K. Deppert, K.A. Dick, J. Johansson, M.W. Larsson, T. Mårtensson, N. Sköld, C. Patrik T. Svensson, B.A. Wacaser, L. Reine Wallenberg, and L. Samuelson, “Growth of one-dimensional nanostructures in MOVPE,” *Journal of Crystal Growth*, vol. 272, Dec. 2004, pp. 211-220.

[27] V.G. Dubrovskii, G.E. Cirlin, I.P. Soshnikov, A.A. Tonkikh, N.V. Sibirev, Y.B. Samsonenko, and V.M. Ustinov, “Diffusion-induced growth of GaAs nanowhiskers during molecular beam epitaxy: Theory and experiment,” *Physical Review B*, vol. 71, May. 2005, p. 205325.

[28] E.I. Givargizov, *Highly Anisotropic Crystals*, Berlin: Springer, 1987.

[29] J. Cahn and R. Hanneman, “(111) Surface tensions of III-V compounds and their relationship to spontaneous bending of thin crystals,” *Surface Science*, vol. 1, Oct. 1964, pp. 387-398.

[30] Landolt-Bornstein, *Group IV Elements, IV-IV and III-V Compounds*, Berlin: Springer, 2006.

[31] T. Akiyama, K. Sano, K. Nakamura, and T. Ito, “An Empirical Potential Approach to Wurtzite-Zinc-Blende Polytypism in Group III-V Semiconductor Nanowires,” *JAPANESE JOURNAL OF APPLIED PHYSICS PART 2 LETTERS*, vol. 45, 2006, p. 275.

[32] T. Akiyama, K. Nakamura, and T. Ito, “Structural stability and electronic structures of InP nanowires: Role of surface dangling bonds on nanowire facets,” *Physical Review B (Condensed Matter and Materials Physics)*, vol. 73, Jun. 2006, pp. 235308-6.

[33] V.G. Dubrovskii and N.V. Sibirev, “Growth thermodynamics of nanowires and its application to polytypism of zinc blende III-V nanowires,” *Physical Review B (Condensed Matter and Materials Physics)*, vol. 77, Jan. 2008, pp. 035414-8.

[34] F. Glas, J. Harmand, and G. Patriarche, “Why Does Wurtzite Form in Nanowires of III-V Zinc Blende Semiconductors?,” *Physical Review Letters*, vol. 99, Oct. 2007, pp. 146101-4.

[35] J.M. Besson, E.H. Mokhtari, J. Gonzalez, and G. Weill, “Electrical properties of semimetallic silicon III and semiconductive silicon IV at ambient pressure,” *Physical Review Letters*, vol. 59, Jul. 1987, p. 473.

[36] A. Fontcuberta i Morral, J. Arbiol, J.D. Prades, A. Cirera, and J.R. Morante, “Synthesis of Silicon Nanowires with Wurtzite Crystalline Structure by Using Standard Chemical Vapor Deposition,” *Advanced Materials*, vol. 19, 2007, pp. 1347-1351.

[37] M. Moewe, L.C. Chuang, V.G. Dubrovskii, and C. Chang-Hasnain, “Growth mechanisms and crystallographic structure of InP nanowires on lattice-mismatched substrates,” *Journal of Applied Physics*, vol. 104, 2008, pp. 044313-4.

[38] M. Moewe, L.C. Chuang, S. Crankshaw, C. Chase, and C. Chang-Hasnain, “Atomically sharp catalyst-free wurtzite GaAs/AlGaAs nanoneedles grown on silicon,” *Applied Physics Letters*, vol. 93, Jul. 2008, pp. 023116-3.

[39] M. Moewe, L.C. Chuang, S. Crankshaw, K.W. Ng, and C. Chang-Hasnain, “Core-shell InGaAs/GaAs quantum well nanoneedles grown on silicon with silicon-transparent emission,” *Optics Express*, vol. 17, May. 2009, pp. 7831-7836.

[40] R.[. Banerjee, A.[. Bhattacharya, A.[. Genc, and B.M.[. Arora, “Structure of twins in GaAs nanowires grown by the vapouraliquidasolid process,” *Philosophical Magazine Letters*, vol. 86, Dec. 2006, pp. 807-816.

[41] R.C. Smith, J.D. Carey, R.D. Forrest, and S.R.P. Silva, “Effect of aspect ratio and anode location on the field emission properties of a single tip based emitter,” *Journal of Vacuum Science & Technology B: Microelectronics and Nanometer Structures*, vol. 23, 2005, p. 632.

[42] J.Y. Huang, S. Chen, S.H. Jo, K. Kempa, and Z.F. Ren, “Giant Field Enhancement at Carbon Nanotube Tips Induced by Multi-Stage Effect,” *Microscopy and Microanalysis*, vol. 11, 2005, pp. 1926-1927.

[43] Y.B. Tang, H.T. Cong, Z.M. Wang, and H. Cheng, “Catalyst-seeded synthesis and field emission properties of flowerlike Si-doped AlN nanoneedle array,” *Applied Physics Letters*, vol. 89, Dec. 2006, pp. 253112-3.

[44] G.T. Boyd, T. Rasing, J.R.R. Leite, and Y.R. Shen, “Local-field enhancement on rough surfaces of metals, semimetals, and semiconductors with the use of optical second-harmonic generation,” *Physical Review B*, vol. 30, Jul. 1984, p. 519.

[45] R.M. Stöckle, Y.D. Suh, V. Deckert, and R. Zenobi, “Nanoscale chemical analysis by tip-enhanced Raman spectroscopy,” *Chemical Physics Letters*, vol. 318, Feb. 2000, pp. 131-136.

[46] Y. Saito, Y. Tsujimoto, A. Koshio, and F. Kokai, “Field emission patterns from multiwall carbon nanotubes with a cone-shaped tip,” *Applied Physics Letters*, vol. 90, May. 2007, pp. 213108-3.

[47] K.A. Dean and B.R. Chalamala, “Field emission microscopy of carbon nanotube caps,” *Journal of Applied Physics*, vol. 85, Apr. 1999, pp. 3832-3836.

[48] S. Tanaka, S. Iwai, and Y. Aoyagi, “Self-assembling GaN quantum dots on Al[sub x]Ga[sub 1 - x]N surfaces using a surfactant,” *Applied Physics Letters*, vol. 69, Dec. 1996, pp. 4096-4098.

[49] P.W. Lee, T.R. Omstead, D.R. McKenna, and K.F. Jensen, “In situ mass spectroscopy and thermogravimetric studies of GaAs MOCVD gas phase and surface reactions,” *Journal of Crystal Growth*, vol. 85, Nov. 1987, pp. 165-174.

[50] C.A. Larsen, N.I. Buchan, S.H. Li, and G.B. Stringfellow, “Decomposition mechanisms of tertiarybutylarsine,” *Journal of Crystal Growth*, vol. 94, Mar. 1989, pp. 663-672.

[51] M. Huang, Kan Bun Cheng, Ye Zhou, B. Pesala, C. Chang-Hasnain, and A. Pisano, “Demonstration of piezoelectric actuated GaAs-based MEMS tunable VCSEL,” *Photonics Technology Letters, IEEE*, vol. 18, 2006, pp. 1197-1199.

[52] Z. Zanolli, F. Fuchs, J. Furthmuller, U. von Barth, and F. Bechstedt, “Model GW band structure of InAs and GaAs in the wurtzite phase,” *Physical Review B (Condensed Matter and Materials Physics)*, vol. 75, Jun. 2007, pp. 245121-8.

[53] I. Vurgaftman, J.R. Meyer, and L.R. Ram-Mohan, “Band parameters for III--V compound semiconductors and their alloys,” *Journal of Applied Physics*, vol. 89, Jun. 2001, pp. 5815-5875.

[54] S.L. Chuang, *Physics of Optoelectronic Devices*, New York, NY: John Wiley & Sons, Inc., 1995.

[55] M.I. McMahon and R.J. Nelmes, “Observation of a Wurtzite Form of Gallium Arsenide,” *Physical Review Letters*, vol. 95, Nov. 2005, p. 215505.

[56] P. Specht, J. Ho, X. Xu, R. Armitage, E. Weber, E. Erni, and C. Kisielowski, “Zincblende and wurtzite phases in InN epilayers and their respective band transitions,” *Journal of Crystal Growth*, vol. 288, Mar. 2006, pp. 225-229.

[57] K. Hiruma, M. Yazawa, T. Katsuyama, K. Ogawa, K. Haraguchi, M. Koguchi, and H. Kakibayashi, “Growth and optical properties of nanometer-scale GaAs and InAs whiskers,” *Journal of Applied Physics*, vol. 77, Jan. 1995, pp. 447-462.

[58] J. Johansson, L.S. Karlsson, C. Patrik T. Svensson, T. Martensson, B.A. Wacaser, K. Deppert, L. Samuelson, and W. Seifert, “Structural properties of <111>B -oriented III-V nanowires,” *Nature Materials*, vol. 5, Jul. 2006, pp. 574-580.

[59] G. Brammertz, M. Heyns, M. Meuris, M. Caymax, D. Jiang, Y. Mols, S. Degroote, M. Leys, and G. Borghs, “Surface recombination velocity in GaAs and In[sub 0.15]Ga[sub 0.85]As thin films,” *Applied Physics Letters*, vol. 90, Mar. 2007, pp. 134102-3.

[60] B. Elman, E.S. Koteles, P. Melman, C. Jagannath, J. Lee, and D. Dugger, “In situ measurements of critical layer thickness and optical studies of InGaAs quantum wells grown on GaAs substrates,” *Applied Physics Letters*, vol. 55, 1989, p. 1659.

[61] H.X. Jiang, J.Y. Lin, K.C. Zeng, and W. Yang, “Optical resonance modes in GaN pyramid microcavities,” *Applied Physics Letters*, vol. 75, 1999, pp. 763-765.